

Aus dem Bereich Theoretische Medizin und Biowissenschaften
der Medizinischen Fakultät
der Universität des Saarlandes, Homburg/Saar

**Biophysical characterization of lipid bilayer stress sensing
by the unfolded protein response transducer PERK**

**Dissertation zur Erlangung des Grades eines Doktors der Medizin
der Medizinischen Fakultät
der UNIVERSITÄT DES SAARLANDES**

2024

vorgelegt von: Philipp Florian Preukschas
geb. am: 04.10.1997 in Augsburg

Aus dem Präklinischen Zentrum für Molekulare Signalverarbeitung
Universitätsklinikum des Saarlandes, Homburg/Saar
(Arbeitsgruppe Prof. Dr. Robert Ernst)

Tag der Promotion: 26.03.2025

Dekan: Univ.-Prof. Dr. med. dent. M. Hannig

Berichterstatter: Prof. Dr. Robert Ernst

Prof. Dr. Barbara Niemeyer-Hoth

Prof. Dr. Lutz Schmitt

Contents

1 Zusammenfassung	4
2 Summary	6
3 Introduction	8
3.1 Biological membranes	8
3.2 The endoplasmatic reticulum	9
3.3 Proteinbiosynthesis and protein modification	9
3.4 Unfolded protein response	10
3.5 Lipid bilayer stress	13
3.6 Membrane compressibility: a key activating factor for IRE1 and PERK	13
3.7 Electron paramagnetic resonance spectroscopy	15
4 Aim	18
5 Materials and equipment	20
5.1 List of equipment	20
5.2 List of chemicals and reagents	21
5.3 List of lipids	21
5.4 List of commercial kits	22
5.5 List of consumables	22
5.6 List of enzymes	23
5.7 List of probes and dyes	23
5.8 List of antibodies	23
5.9 List of primers	24
5.10 List of plasmids	25
5.11 List of <i>E. coli</i> strains	26
5.12 List of media for <i>E. coli</i> cultivation	27
5.13 List of buffers	28
6 Methods	30
6.1 Cultivation and storage of <i>E. coli</i>	30
6.2 Preparation of chemically competent <i>E. coli</i>	30
6.3 Site-directed mutagenesis	30
6.3.1 QuikChange™ site-directed mutagenesis	30
6.3.2 In-Fusion™ site-directed mutagenesis	31
6.3.3 Q5™-Phusion site-directed mutagenesis	32
6.4 Agarose gel electrophoresis	33
6.5 Transformation of <i>E. coli</i>	33
6.6 Plasmid isolation	33
6.7 DNA sequencing	33
6.8 Heterologous production of PERK-transmembrane region (TMR) proteins in <i>E. coli</i>	33
6.9 Preparation of amylose resin	34

6.10 Purification and labeling of MBP-transmembrane helix (TMH) constructs by affinity chromatography	34
6.11 Size-exclusion chromatography	35
6.12 Preparation of liposomes	35
6.13 Testing lipid density by C-Laurdan fluorescence spectroscopy	36
6.14 Preparation of SM-2 Biobeads™	36
6.15 Reconstitution of PERK-TMR proteins in liposomes	37
6.16 Electron paramagnetic resonance (EPR) spectroscopy	37
6.17 SDS-polyacrylamide gel electrophoresis	38
6.18 InstantBlue™ staining	38
6.19 Immunoblotting	39
6.20 Tobacco Etch virus protease cleavage	39
6.21 Sucrose density gradient centrifugation of proteoliposomes	39
6.22 Estimating lipid content using Hoechst 33342 fluorescence	39
6.23 Sodium carbonate extraction from proteoliposomes	40
7 Results	42
7.1 Bioinformatic analysis of the predicted PERK-TMR	42
7.1.1 Evolutionary conservation of the predicted PERK-TMR	43
7.2 Preparation of PERK-TMR protein	44
7.2.1 Heterologous production, purification and labeling of the PERK-TMR in <i>E. coli</i>	44
7.2.2 Determining the spin labeling efficiency of PERK-TMR variants	48
7.3 Optimization of the reconstitution of PERK-TMR protein in liposomes	50
7.3.1 Comparing the reconstitution of the cysteine-less PERK-TMR to the native cysteine-containing PERK-TMR	51
7.3.2 The effect of different lipid environments on the reconstitution of PERK-TMR	53
7.3.3 The effect of different protein to lipid ratios on the reconstitution of PERK-TMR	55
7.4 Quality control of the reconstitution of PERK-TMR in liposomes	56
7.4.1 Loss of protein during the reconstitution of cysteineless PERK-TMR	56
7.4.2 Stability of insertion of reconstituted cysteine-less PERK-TMR in a POPC environment	57
7.5 Processing and interpretation of EPR-spectra	58
7.6 EPR spectra of the PERK-TMR	62
7.6.1 EPR-Spectra of spin-labeled PERK-TMR at room temperature	62
7.6.2 EPR-Spectra of spin-labeled PERK-TMR at low temperature (-196 °C)	64
7.7 The effect of different lipid environments on the PERK-TMR	66
7.7.1 Characterization of the used lipid environments	66
7.7.2 Lipids lead to a pronounced change in the cwEPR spectra of PERK-TMR	69
7.7.3 POPE has no effect on the dimerization of PERK-TMR	72
7.7.4 Cholesterol at high concentrations make an reconstitution of PERK impossible	76
7.7.5 Soy PI shows no effect on the cwEPR spectra of PERK-TMR	79

8 Discussion	82
8.1 Establishment of a robust system for examining PERK-TMR through cwEPR	82
8.2 Experimental insights into PERK-TMR: The transition zone between amphipathic and transmembrane helix	82
8.3 Mechanical activation of the PERK-TMR	83
9 Appendix	86
9.1 Python code for semi-automatic EPR spectra analysis	86
10 List of Figures	92
11 List of Tables	94
12 List of Acronyms	96
13 References	98
14 Danksagung	104
15 Lebenslauf	106

1 Zusammenfassung

Das endoplasmatische Retikulum (ER) ist ein Schlüsselorganell der Membranbiogenese. Die Homöostase des ER wird unter anderem durch die sogenannte Unfolded Protein Response (UPR) reguliert, die bei Säugetieren durch drei single-pass Membranproteine in der ER-Membran vermittelt wird. Da die UPR nicht nur durch ungefaltene Proteine, sondern auch durch Veränderungen der Lipidumgebung der ER-Membran selbst ausgelöst werden kann, untersucht die vorliegende Arbeit die Struktur-Funktions-Beziehungen des transmembranen Bereichs des UPR-Transducers protein kinase R like endoplasmic reticulum kinase (PERK). Dazu wurde ein minimales Membransensor-Konstrukt, basierend auf der Transmembranhelix von PERK, in verschiedenen Lipidumgebungen rekonstituiert. Das Konstrukt wurde mit jeweils einer einzelnen MTSL-Sonde markiert, welche an das jeweils einzige Cystein in der PERK-Transmembranhelix gebunden wurde. Anzumerken ist, dass das native PERK ein einzelnes Cystein in der nativen Transmembranhelix enthält, welches vorher entfernt wurde, bevor andere Einzel-Cystein-Varianten erzeugt wurden. Elektronenspinresonanzspektroskopie wurde verwendet, um Einblicke in die Struktur, Dynamik und Oligomerisierung von PERK in den verschiedenen Lipidumgebungen zu gewinnen.

Durch experimentelle Methoden wurden zusätzliche Einblicke in den amphipathischen-transmembranen Übergang gewonnen. Funktionell interessante Reste wurden entdeckt, wie beispielsweise ein polarer Rest, welcher in den Acylketten-Bereich der Membran hineinragt und dadurch die effiziente Inserierung der Transmembranhelix in die Lipid-Doppelschicht erschwert. Bemerkenswert ist, dass in dieser Studie eine außergewöhnliche Empfindlichkeit von PERK gegenüber der Lipidumgebungen nachgewiesen werden konnte: Das Ausmaß der Oligomerisierung, gemessen an den Spin-Spin-Interaktionen, nimmt mit spezifischen Änderungen der Lipidzusammensetzung erheblich zu. Unsere Daten deuten darauf hin, dass sich PERK ähnlich wie der am stärksten konservierte UPR-Transducer Inositol-requiring Enzyme 1 (IRE1) (wie in *S. cerevisiae* untersucht) verhält. Systematische EPR-Daten deuten darauf hin, dass PERK Protomere miteinander assoziieren, wobei die N-terminalen Bereiche der Transmembrandomäne der Membranoberfläche "aufliegen" und von der Kontaktfläche der Proteine wegzeigen. Diese Daten liefern wichtige Eck- und Validierungspunkte für umfangreiche Molecular-Dynamic Simulationen (MD), die von den Forschungsgruppen Hummer und Covino aus Frankfurt durchgeführt werden.

Basierend auf der Lipidabhängigkeit der Oligomerisierung wurde die Rolle von Lipiden auf PERK mittels spezieller Rekonstitutionsexperimente weiter untersucht. Es wurde bereits in der Literatur vorgestellt, dass PERK in stark gesättigten Membranen dimerisieren kann (Volmer, Ploeg, Ron 2013). Es blieb jedoch zu untersuchen, ob diese Lipidsensitivität auf bloße Lipidphasen-Trennung basiert oder ob sie die Fähigkeit von PERK zeigt, physiologisch vorkommende Lipidveränderungen zu erkennen und als Regler der Homöostase zu fungierend. Tatsächlich sind die speziellen Parameter, auf die die PERK-Transmembranregion reagiert – ob nur auf Lipidpackungsdichte, Protein/Lipid-Verhältnis oder spezifische Lipidkopfgruppen – derzeit unbekannt. Um zu untersuchen, wie die Transmembranregion von PERK spezifisch auf bestimmte Lipidzusammensetzungen reagiert, wurde das minimale Konstrukt der PERK-Transmembranregion, markiert an seinem nativen Cystein mit einer MTSL-Sonde, in verschiedenen Lipidumgebungen rekonstituiert. Einzelne Komponenten der Lipidumgebung wurden auftitriert, um den Einfluss einzelner Lipide auf die Oligomerisierung zu untersuchen. Anschließend wurde die Elektronenspinresonanzspektroskopie durchgeführt, um Veränderungen in der PERK-Homodimerisierung zu

identifizieren.

Die komplexe Lipidumgebung CHO2 wurde ausgewählt, um eine Kombination mehrerer Merkmale zu reflektieren, die bekanntermaßen die UPR in Zellen auslösen (z.B. erhöhte Lipidsättigung, erhöhter Sterolspiegel, erhöhtes PE-zu-PC-Verhältnis). Sie löst ebenfalls eine erhöhte Oligomerisierung von PERK aus, was aus einer signifikanten spektralen Verbreiterung der EPR-Spektren abgeleitet wurde. Einzelne Komponenten der CHO2-Umgebung (POPE, Cholesterin, PI) wurden auftitriert, und ein Screening wurde durchgeführt. Die Ergebnisse zeigten, dass die Transmembranregion von PERK möglicherweise durch einen auf hydrophoben Mismatch basierenden Mechanismus reguliert wird, ähnlich wie Ire1 aus *S. cerevisiae*. Die Erhöhung des hydrophoben Mismatch durch die Titration von Cholesterin behinderte auch die erfolgreiche Rekonstitution von PERK, was darauf hindeutet, dass die Membraninsertion hier tatsächlich energetisch ungünstig ist.

2 Summary

The endoplasmic reticulum (ER) is a key organelle of membrane biogenesis. ER homeostasis is regulated by the so-called unfolded protein response (UPR), which is mediated in mammals by three single-pass membrane proteins in the ER membrane. Because the UPR can also be triggered by aberrancies in the ER membrane, this thesis investigates the structure-function relationships in the transmembrane domain of the UPR transducer PERK. A minimal membrane sensor construct based on the transmembrane helix of PERK was generated and then reconstituted in various lipid environments. The construct is labeled with spin probes, installed at the position of unique cysteines installed in the construct. Notably, PERK contains a single cysteine in its native transmembrane helix region, which was removed prior to generating other single-cysteine variants. Electron spin resonance spectroscopy was employed to gain insight into the structure, dynamics, and oligomerization of PERK in the lipid bilayer.

Through experimental means, additional insights into the amphipathic-transmembrane transition were obtained. Functionally interesting residues were discovered, such as a polar residue protruding into the acyl chain region of the membrane, thereby interfering with efficient insertion of the transmembrane helix in the lipid bilayer. Remarkably, this study demonstrates an extraordinary sensitivity of PERK to its lipid environments: The degree of oligomerization, as judged from spin-spin interactions, increases substantially with specific changes of the lipid composition. Our data suggests that PERK oligomerizes similarly to the most conserved UPR transducer inositol-requiring enzyme type 1 (IRE1) (as studied in *S. cerevisiae*). Systematic EPR data suggests that PERK protomers associated with each other, having the N-terminal regions of the TMD "lying" in the membrane surface and pointing away from the dimer interface. This data provides important constraints and validation for extensive molecular dynamics (MD) simulations performed by the research groups Hummer and Covino from Frankfurt.

Based on the lipid-dependency of oligomerization, the role of lipids on PERK was explored more widely using dedicated reconstitution experiments. It was previously proposed that PERK can dimerize in highly saturated membranes (Volmer, Ploeg, Ron 2013). However, whether this lipid sensitivity is based on lipid phase separation and whether it also reflects an ability of PERK to sense under more physiological conditions remained to be investigated. In fact, the parameters to which the PERK transmembrane region responds—whether only to lipid packing density, protein/lipid ratio, or specific lipid headgroups—are currently unknown. To investigate how the transmembrane region of PERK specifically reacts to certain lipid composition, the minimal construct of the PERK transmembrane region labeled at its native cysteine with a spin probe was reconstituted in various lipid environments. Individual components of the lipid mixture were titrated to study the impact of specific lipids on the oligomerization. Subsequently, electron spin resonance spectroscopy was conducted to identify changes in PERK homodimerization.

The complex lipid environment CHO2, which was chosen to reflect a combination of several features which are known to trigger the UPR in cells (e.g. increased lipid saturation, increased sterol level, increased PE-to-PC ratio), also triggered an increased oligomerization of PERK, which was deduced from significant spectral broadening of the EPR spectra. Individual components of the CHO2 environment (POPE, Cholesterol, PI) were titrated, and a screening was conducted. The results indicated that the PERK transmembrane region may be regulated by a hydrophobic mismatch-based mechanism, similarly to Ire1 from *S. cerevisiae*. Increasing the hydrophobic mis-

match through the titration of cholesterol hindered the successful reconstitution of PERK, thereby suggesting that membrane insertion indeed is energetically unfavorable.

3 Introduction

3.1 Biological membranes

Biological membranes separate cells from their environment. In eukaryotes, they also compartmentalize the intra-cellular space into different organelles. As membranes do not allow for a free flux of sizeable, polar or charged molecules across membranes they are equipped with many functionalities for nutrient transport, drug extrusion, and signal transduction. The plasma membrane serves as a protective layer between the homeostatic, intra-membrane milieu and the ever-changing environment. Each organelle features characteristic lipidomes and proteomes that jointly define their identity. The stability and flexibility of biomembranes facilitate even extreme topological transitions, which are crucial –on the microscopic level- for example during endocytosis and membrane fusion events and -macroscopically- for architectural features enabling functions of special cell species (e.g. surface-enlarging microvilli in the gastrointestinal tract or neuron cells spanning several meters) (Robertson 2018).

The vast majority of biological membranes form lipid bilayers. Two layers of lipids (mainly glycerophospholipids, sphingolipids and cholesterol in mammalian cells) arrange themselves in a sandwich-conformation of polar headgroup-hydrophobic core-polar headgroup (van Meer, Voelker, Feigenson 2008). The characteristic lipid compositions are crucially contributing the bulk biophysical membrane properties such as viscosity/fluidity, thickness and melting temperature. To these basic membrane components, various membrane proteins are added, giving the particular membrane a unique set of properties and functions.

Various models try to explain how proteins and lipids interact in biological membranes, but the fluid mosaic model, introduced by Singer and Nicolson in 1972, is most widely known (Singer, Nicolson 1972). This model portrays the cell membrane as a dynamic, liquid-like 2-dimensional structure, enabling essential molecular movements along the bilayer plane. The fluidity of the lipid bilayer allows individual lipid molecules to move laterally, providing flexibility, crucial for membrane function: from selective molecule transport to cellular signaling as well as the formation and dissolution of macromolecular transmembrane complexes.

In response to temperature fluctuations, cell membranes exhibit a remarkable ability to adapt their composition to maintain membrane fluidity – a process referred to as homeoviscous adaptation. This adaptive mechanism ensures stability through lipid condensation at lower temperatures and enhanced fluidity at higher temperatures. This is exemplified in arctic fish (Malekar et al. 2018) or buckwheat (Taira, Akimoto, Miyahara 1986), where cell membranes incorporate unsaturated fatty acids to maintain fluidity and prevent solidification in cold environments. During elevated temperatures, (tomato) plants strategically modify the lipid composition of their thylakoid membranes of their chloroplasts. This includes an increase in saturation of galactolipids, ensuring optimal membrane fluidity and facilitating efficient photosynthetic processes under heat stress conditions (Spicher, Glauser, Kessler 2016).

Yeast cells, when exposed to osmotic stress or dehydration, undergo changes in the lipid composition of their plasma membranes. Adjustments in sphingolipids (Zhu et al. 2020) and ergosterol levels (Dupont et al. 2011) contribute to membrane fortification, preventing water loss and sustaining cellular viability in environments with altered osmotic pressures.

Under chronic oxidative stress, neural cells adjust both cholesterol and sphingomyelin lev-

els in their membranes, defending against destabilization caused by oxidized lipids, particularly the oxidation-prone omega-3 fatty acid docosahexaenoic acid— a crucial component of neuronal cell membranes. Cholesterol's antioxidant properties play a vital role in counteracting free radicals, contributing to the overall protection of the cell membrane under oxidative stress conditions (Clement et al. 2009).

3.2 The endoplasmatic reticulum

The endoplasmatic reticulum (ER) spans the entire cell with a dynamic system of fine, interconnected tubular and sheet-like membrane-structures (peripheral ER). It is continuous with the nuclear envelope, as it forms the outer nuclear membrane (nuclear ER). A significant portion of the ER forms intimate contacts with the plasma membrane (cortical ER) as hotspots for inter-organelle lipid transfer (Voeltz, Rolls, Rapoport 2002).

The functions of the ER are manifold: The vast majority of secretory proteins are synthesized by ER-associated ribosomes and either co- or posttranslationally translocated into the ER lumen, where they undergo folding. Likewise, most membrane proteins are inserted into the membrane at the level of the ER. It thus takes a crucial role in the maintenance of lipid and protein homeostasis (Sun, Brodsky 2019; Ellgaard, Helenius 2003). It also maintains contact sites with the various other organelles and the plasma membrane, which act as a means of non-vesicular transport and exchange of lipids as well as stored Ca^{2+} (Koch 1990; H. Wu, Carvalho, Voeltz 2018).

The ER can be electron-microscopically differentiated in a rough endoplasmatic reticulum (rER) and a smooth endoplasmatic reticulum (sER). The rER is studded with ribosomes involved in synthesizing secretory and transmembrane proteins. The sER is generally believed to have function in lipid biosynthesis and p450-dependent detoxification. The rER is highly abundant in professional secretory cells such as the insulin-producing β -cells of the pancreas or antibody-producing plasma cells. The tubular shaped sER is more pronounced in cells specialized in metabolizing lipids and xenobiotics. The sER is most abundant in hepatocytes, the steroid-hormone producing cells of the kidney and muscle cells (as so called sarcoplasmatic reticulum) (Westrate et al. 2015; Voeltz, Rolls, Rapoport 2002).

3.3 Proteinbiosynthesis and protein modification

A future secretory or membrane-bound protein in eukaryotic cells must undergo different steps until it is functional. The genetic information is stored inside the nucleus in form of a deoxyribonucleic acid (DNA), which has to be unzipped and transcribed into a messenger ribonucleic acid (mRNA). Ribosomes translate the genetic code of the mRNA into a polypeptide chain until a cytosolic signal recognition particle (SRP) recognizes an N-terminal signal peptide. A complex of ribosome, mRNA, SRP and nascent polypeptide chain forms and pauses translation momentarily until the complex is transferred to a SRP-receptor on the ER membrane. From here the nascent polypeptide chain is co-translationally translocated into the ER lumen through the translocation channel composed of a SEC61 translocation complex (Pool 2022; Merrick 1992). Newly synthesized proteins are folded in the lumen of the ER and undergo post-translational modifications including N-linked glycosylations and disulfide formation (Braakman, Hebert 2013).

ER-luminal chaperones shield the nascent polypeptide chain from interactions with the high

concentration of other proteins in the ER lumen and assist in folding the polypeptide chain during and after translation. Chaperones directly interfere with the polypeptide chain coming through the translocation channel. The binding immunoglobulin protein (BiP) is an important ER-luminal chaperone, whose function goes beyond its mere role as a folding assistant.

BiP also recognizes unfolded proteins by sensing hydrophobic regions on the outside of unfolded proteins which would normally evade the polar environment by turning to the inside of the 3D protein structure during proper folding. Further, BiP plays an integral part in the unfolded protein response discussed below, as the aggregation of unfolded proteins in the ER lumen can have harmful consequences for the cell by e.g. potentially interacting and aggregating with otherwise functional proteins (Ellgaard, Helenius 2003; Hebert, Molinari 2007). BiP also acts as an independent activation factor for the Unfolded Protein Response (UPR) transducers IRE1 α and PERK (Kopp et al. 2019) discussed below, whereby the specific mechanism is still a matter of debate. Three models have been proposed of how BiP interacts with the UPR transducer IRE1 α (see 1 (A-C)):

According to the chaperone inhibition mechanism, BiP binds to IRE1 α to keep it from dimerizing. This keeps IRE1 α in its monomeric, inactive state in the absence of proteotoxic stress. However, if unfolded proteins accumulate in the ER lumen, BiP is sequestered away from IRE1 α due to its binding preference for unfolded proteins. Consequently, IRE1 α dimerizes, initiating the UPR signaling cascade.

According to the allosteric mechanism, BiP's nucleotide binding domain (NBD) interacts with IRE1 α , blocking its oligomerization. Unfolded proteins in the ER lumen are sensed by BiP's substrate binding domain (SBD). When an unfolded protein binds to BiP, it induces a conformational change in BiP, releasing BiP's association with IRE1 α , thus enabling the dimerization of IRE1 α . In both the chaperone inhibition model, as well as the allosteric model, IRE1 α is a passive element and the protein sensing capabilities are part of BiP.

In the direct mechanism, unfolded proteins directly interact with the ER-luminal domain of IRE1 α . This direct binding stabilizes dimerization and oligomerization of IRE1 α . The direct interaction of unfolded proteins with IRE1 α bypasses the need for BiP dissociation to initiate UPR signaling. It is possible that the three models of IRE1 α activation are cooperative rather than mutually exclusive.

3.4 Unfolded protein response

The UPR was first documented as the up-regulation of chaperones during the increased accumulation of unfolded proteins in the ER (ER stress) (Kozutsumi et al. 1988). UPR is a highly conserved mechanism in eucaryotic cells from yeast to mammals and an integral part of maintaining protein homeostasis.

The UPR in mammalian cells relies on three UPR transducing proteins: the highly conserved inositol-requiring enzyme type 1 (IRE1 α), the activating transcription factor 6 (ATF6) and the protein kinase R like endoplasmic reticulum kinase (PERK). They all are single-pass trans-membrane proteins, residing mostly in the ER (Radanović, Reinhard, et al. 2018; Radanović, Ernst 2021).

IRE1 α is an ER transmembrane protein that possesses both kinase and endoribonuclease domains. When activated, IRE1 α undergoes autophosphorylation and activates its endoribonuclease activity. This activity splices the XBP1 (X-box binding protein 1) mRNA, producing an active

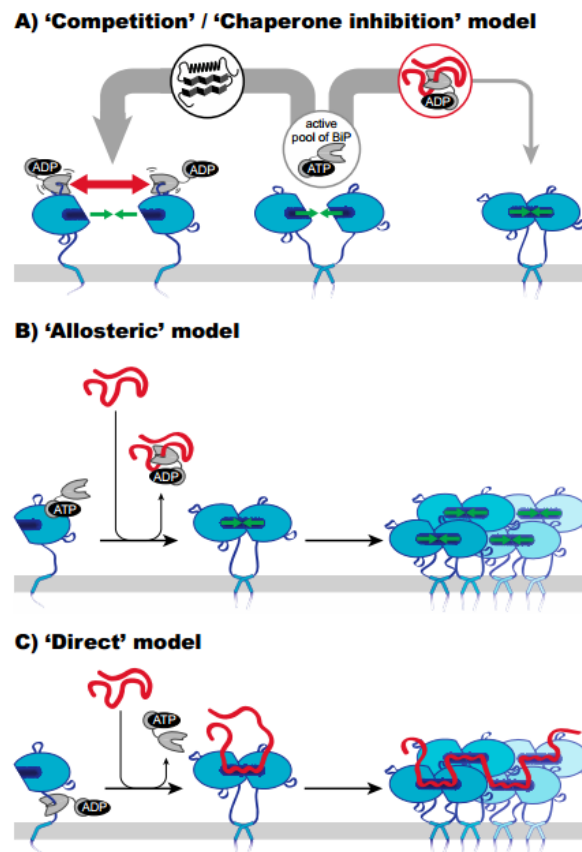


Figure 1: 3 models of the interaction between the UPR transducer $IRE1\alpha$, BiP and unfolded proteins. (A) **Competition Model:** BiP dynamically associates with $IRE1\alpha$, preventing its spontaneous dimerization. Under ER stress, BiP shifts its association to unfolded proteins, allowing $IRE1\alpha$ to dimerize and activate the Unfolded Protein Response (UPR). (B) **Allosteric Model:** BiP's nucleotide binding domain (NBD) physically blocks $IRE1\alpha$'s dimerization. Unfolded proteins in the ER induce a conformational change in BiP, releasing its association with $IRE1\alpha$ and enabling UPR activation. (C) **Direct Model:** Unfolded proteins directly bind to $IRE1\alpha$'s ER-luminal domain, stabilizing the dimerization/oligomerization of $IRE1\alpha$. This direct interaction serves as an activating ligand, triggering the UPR in response to ER stress. Here $IRE1\alpha$ shows direct sensing capabilities instead of being merely dependent on BiP. Illustration adapted from (Radanović, Ernst 2021).

form of XBP1s. XBP1s translocates to the nucleus and induces the expression of genes involved in ER-associated degradation (ERAD) and protein folding.

ATF6 is another ER transmembrane protein, acting as a transcription factor. Under ER stress, ATF6 is transported to the Golgi apparatus and cleaved by different proteases. The cleaved ATF6 fragment (ATF6c) then moves to the nucleus, activating the expression of UPR target genes responsible for protein folding and ERAD as well as expanding the ER membrane (Maiuolo et al. 2011).

PERK, an ER transmembrane kinase, becomes activated upon ER stress through autophosphorylation. Activated PERK phosphorylates the α subunit of eukaryotic initiation factor 2 (eIF2 α), leading to global translational attenuation. This reduction in protein synthesis alleviates ER workload by limiting the influx of newly synthesized proteins into the ER. The translation of specific mRNAs, such as the Activating Transcription Factor 4 (ATF4), is selectively upregulated. ATF4 translocates to the nucleus, inducing the expression of genes involved in amino acid metabolism,

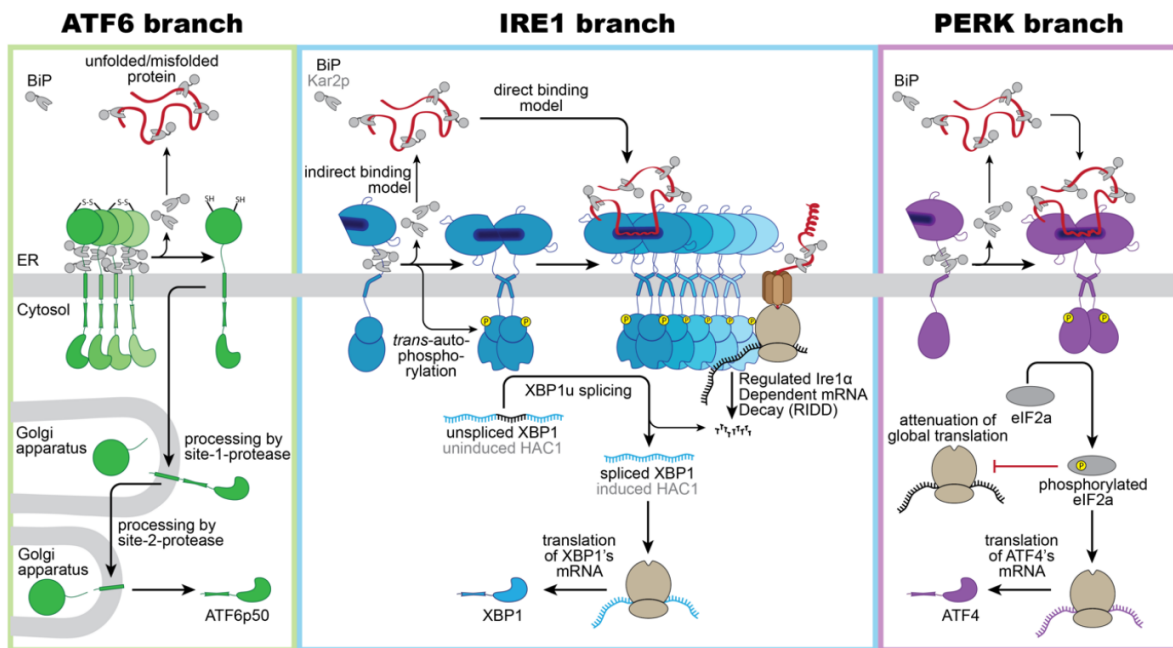


Figure 2: Schematic overview of the UPR signaling during proteotoxic ER stress, involving the three primary branches: ATF6, IRE1 α and PERK.

Left Panel (ATF6): Inactive ATF6 forms stabilized homo-oligomers with intermolecular disulfide bonds. BiP interacts with ATF6 under normal conditions. Upon ER stress, BiP dissociates, allowing ATF6 to be transported to the Golgi apparatus. Processing by different proteases releases a transcriptionally active fragment (ATF6p50) that regulates UPR target genes in the nucleus.

Middle Panel (IRE1 α): Inactive IRE1 α monomers associate with BiP. Proteotoxic ER stress induces dimerization, releasing BiP and forming higher homo-oligomers. Activated IRE1 α cleaves unspliced XBP1/HAC1 mRNA, initiating unconventional splicing and activating XBP1/HAC1. IRE1 α oligomers can also reduce the further increase of unfolded proteins through regulated IRE1 α dependent mRNA decay (RIDD).

Right Panel (PERK): Proteotoxic ER stress causes BiP dissociation from PERK, promoting the formation of PERK dimers and oligomers. Trans-autophosphorylation activates PERK's cytosolic kinase domain, leading to eIF2 α phosphorylation. eIF2 α leads to global translation attenuation. Further ATF4 production is selectively increased. ATF4 regulates both pro-survival and pro-apoptotic signals, contributing to the cellular response to ER stress. Illustration adapted from (Radanović, Ernst 2021).

redox regulation, and apoptosis. The PERK pathway is distinctive for its role in balancing protein synthesis and maintaining cellular homeostasis during ER stress, emphasizing global translational control.

To counteract the further increase of unfolded proteins in the ER lumen, UPR activation triggers a variety of adaptive responses in the ER: The folding capacity of the ER as well as the ER volume is increased. The folding workload is also decreased by lowering the initiation of translation via the so-called integrated stress response. Furthermore, to remove terminally misfolded proteins from the ER, components of the ERAD pathway are upregulated. If the ER stress can not be resolved and the proteotoxic stress prevails, the UPR can trigger cell apoptosis (Walter, Ron 2011; Korennykh, Walter 2012).

Lipid imbalances in biological membranes are equally potent, activating signal for the UPR (Wang et al. 2018; Volmer, Ploeg, Ron 2013; Pineau et al. 2009). The adaptation of UPR transduc-

ers to respond not only to proteotoxic stress but also to lipid bilayer stress offers several benefits and carries significant implications.

3.5 Lipid bilayer stress

Lipid Bilayer Stress (LBS) refers to an abnormal lipid composition in the ER membrane, which triggers a response similar to the UPR. It is typically initiated by the UPR transducer IRE1 in yeast and mammals, and possibly the UPR transducer PERK, even in the absence of their luminal sensing domain, which is critical for detecting misfolded proteins, indicating that these proteins also have sensing capabilities in their respective transmembrane region (TMR) (Volmer, Ploeg, Ron 2013; Ho et al. 2020).

Lipid bilayer stress is an umbrella term for all compositional changes of the ER membrane, which lead to UPR activation. A large variety of lipid metabolic changes all lead to lipid bilayer stress (Perturbance of the phosphatidylcholine (PC) and phosphatidylethanolamine (PE)-ratio, perturbation of the protein to lipid packaging ratio, the ratio of saturated and unsaturated lipids, inositol depletion). Chronification of metabolic aberrancies can cause chronic UPR activation, which can cause cell damage and decay associated with complex metabolic disorders. Lipid bilayer stress is emerging as a significant contributor to various pathological conditions, particularly in diseases related to excessive lifestyle, such as Type II diabetes, fatty liver disease, and arteriosclerosis (Mandl et al. 2013; Han, Kaufman 2016; Zámbo et al. 2013; Hotamisligil 2010).

Different models have been put forward how lipid bilayer stress may trigger the UPR. This activation can be direct, as seen in the interaction of dihydrosphingosine and dihydroceramide with the transmembrane region of ATF6 (Tam et al. 2018). Or more intricately and indirectly: Saturated lipids, sterols trigger the oligomerization UPR transducers by affecting the physicochemical properties of the ER membrane. Increased lipid packing lowers the membrane compressibility, thereby increasing the energetic penalty of IRE1 α and PERK for membrane distortion. This provides a hydrophobic mismatch-based driving force for dimerization, when distorted membrane areas around the transducer can coalesce (Kaiser, Orłowski, et al. 2011; Halbleib et al. 2017). The most indirect activation mechanism is proposed for highly increased PC-to-PE ratios in mammals. The increased PC-to-PE ratio reduces the activity of the ER-localized Ca²⁺ pump SERCA, thereby lowering the Ca²⁺ levels in the ER lumen. This decrease leads to an impairment of Ca²⁺-dependent chaperones (e.g. BiP) and hereby to the activation of the UPR (Preissler et al. 2020; Fu et al. 2011). Presumably due to the fact that SERCA is missing in yeast, and because the ER in yeast does not serve as the primary Ca²⁺ reservoir in cells, an increased PC-to-PE ratio does not trigger the UPR (Reinhard et al. 2024). Studying the mechanism of UPR by LBS is challenging, in particular in mammals, because any interference with the cellular protein folding machinery or lipid metabolism has numerous ripple effects throughout the lipid metabolic network, which are impossible to predict. Not every metabolic perturbation leads to UPR activation.

3.6 Membrane compressibility: a key activating factor for IRE1 and PERK

Even though PERK is known to be activated under conditions of lipotoxicity when saturated lipids accumulate, it remains largely unexplored how PERK senses ER membrane properties. Based on sequence analyses and bioinformatic predictions, it seems possible that PERK uses a similar

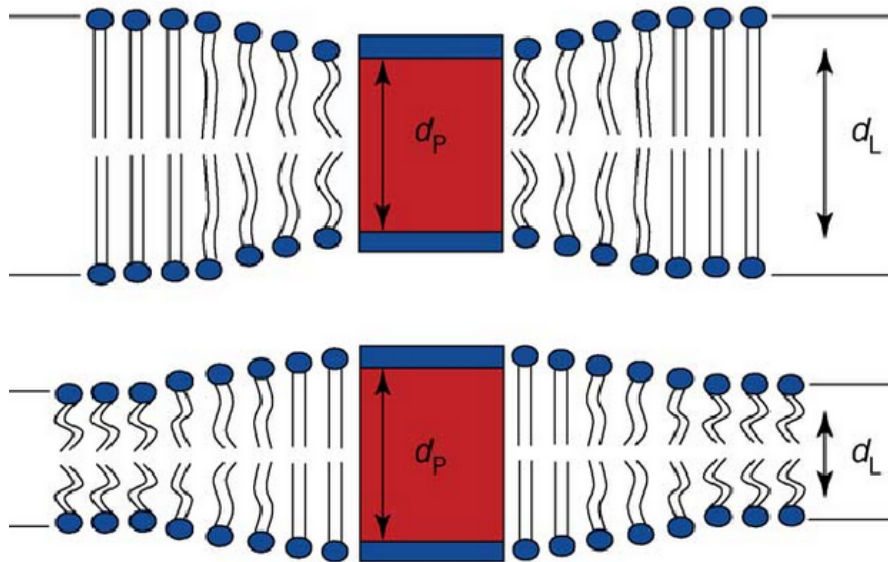


Figure 3: A schematic illustration of hydrophobic mismatch.

Depending on the mismatch of the length of the hydrophobic part of a transmembrane helix (d_P) and the thickness of the lipid bilayer (d_L), membrane and protein interact with each other. If the hydrophobic mismatch is negative (Length of hydrophobic transmembrane helix smaller than the thickness of the lipid bilayer) the membrane gets squeezed near the protein helix (see top illustration) and vice versa. Illustration adapted from (Janmey, Kinnunen 2006).

mechanism as the UPR transducer IRE1 from yeast: a short transmembrane helix and an adjacent amphipathic helix that cause a local membrane distortion by thinning the lipid bilayer. Each transmembrane protein uses a hydrophobic interface exposed to the hydrophobic acyl chains in the lipid bilayer (Mouritsen, Bloom 1984). If a transmembrane helix features a hydrophobic thickness that matches perfectly the hydrophobic thickness of the surrounding lipid bilayer, there is a minimal energetic penalty. If, however, the transmembrane domain is shorter or much longer than the surrounding bilayer, the lipids would have to locally deform to accommodate the membrane protein. This causes energetic costs, which can again be minimized by oligomerizing the protein by their hydrophobic segment that does not match the surrounding bilayer (Fattal, Ben-Shaul 1993).

This free energy of membrane protein insertion is not only dependent on the hydrophobic mismatch, even though this is an important contributor. It also is dependent on the lipid composition of the membrane, which affects the compressibility of the membrane (Renne, Ernst 2023). A deformable and compressible membrane, rich in poorly packed lipids, can accommodate an unfavorable transmembrane domain better than a tightly packed and more rigid membrane. In fact, this mechanism contributes to the sorting of transmembrane proteins along the secretory pathway, as the organelles along the secretory pathway feature increasingly higher sterol levels, which lower membrane compressibility. Thus, hydrophobic mismatching acts as a sorting mechanism of transmembrane proteins in the cell. The median length of the (hydrophobic) transmembrane domain in proteins increases along the secretory pathway (Sharpe, Stevens, Munro 2010). The ER, on the other hand, has a rather deformable membrane due to its low sterol content and can accommodate a wide range of transmembrane domains.

Every transmembrane domain of a protein spanning through a biological membrane leaves an imprint on the lipid bilayer, especially if a high hydrophobic mismatch is present. The compara-

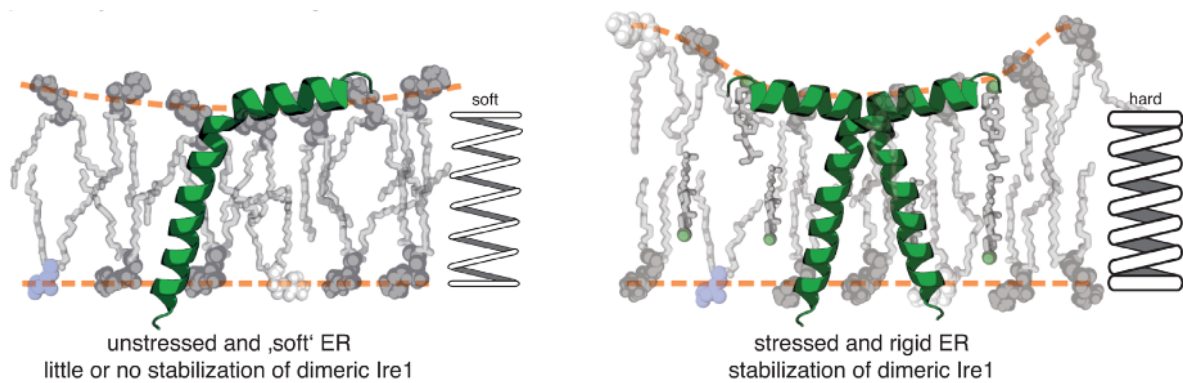


Figure 4: IRE1 dimerizes to spread the energetic cost of membrane compression.

The amphipathic helix of IRE1 enlarges the protein/lipid interface causing also a larger imprint in the membrane. IRE1 dimerization minimizes the free energy, by the regions of membrane distorting around each protomer coalesce. Stabilizing this conformation and splitting the energetic cost of compressing the membrane between multiple proteins. Illustration adapted from (Radanović, Reinhard, et al. 2018).

bly short transmembrane helix of both IRE1 and PERK should leave a pronounced imprint in the lipid bilayer of the ER. This imprint is further enlarged by the adjacent amphipathic helix, which increases the lipid bilayer-protein contact surface.

Lipid metabolic changes that increase the rigidity of the ER membrane affect the oligomerization of every protein with a hydrophobic mismatch. However, Ire1 is particularly sensitive due to its juxtamembrane amphipathic helix that increases the membrane imprint. If a similar mechanism of sensing is at work in PERK remained to be tested.

Many studies have been conducted primarily on the yeast Ire1 to differentiate between the role of unfolded protein and of lipid bilayer stress. IRE1 of yeast and mammals is activated even in the absence of unfolded proteins in the ER lumen (Kitai et al. 2013; Ariyama et al. 2010), or when the ER-luminal domain of Ire1 (yeast) is either entirely removed (Ho et al. 2020) or impaired (yeast) by mutation in its ability to bind unfolded proteins (Halbleib et al. 2017) or to dimerize (yeast) (Väth et al. 2021). Furthermore, the protein-independent activation of IRE1 is hindered by changes in the TMH-adjacent amphipathic helix, either in the function to sense special lipid headgroups like inositol (yeast) (Tran, Takagi, Kimata 2019), or in a general inability to sense membrane-associated stress (yeast) (Halbleib et al. 2017). Intriguingly, systematic mutations along the TMH do not lead to an impairment of mammalian IRE1 (or PERK) function (Väth et al. 2021; Volmer, Ploeg, Ron 2013). This led to the hypothesis that rather than sequence identity, the overall properties of the transmembrane domain may be the basis of lipid bilayer stress sensing. So far, the most mechanistic work along these lines have been performed with Ire1 from yeast. A similarly extensive study has not been performed for the mammalian PERK.

3.7 Electron paramagnetic resonance spectroscopy

The electron paramagnetic resonance spectroscopy (EPR) is the main method of this thesis. EPR was first used in 1944 by Yevgeny Zavoisky as a method used to study the atomic structure of metal complexes. The following paragraphs shall only introduce a basic understanding of the physics behind EPR (Schosseler 1998).

There are two prominent usage modes of EPR spectroscopy in life sciences: continuous wave Electron Paramagnetic Resonance (cwEPR) and pulsed Electron Paramagnetic Resonance (pulsed EPR), each offering distinct advantages and applications.

cwEPR involves continuously irradiating the sample with microwave radiation while monitoring the absorption or emission of energy. It allows for the determination of key parameters such as g-factor, linewidth and spin concentration. From the first two parameters, conclusions about the environmental variables can be derived (such as the polarity of the surroundings, proximity to other spin probes or atoms, aggregation states of spin-labeled proteins). Through cwEPR data, interspin distances between 0.8 nm and 2.0 nm can be recorded (Edwards et al. 2013). However, cwEPR typically lacks temporal resolution, making it less suitable for studying dynamic processes such as enzyme-substrate interactions or receptor binding kinetics. In cwEPR, temperature plays a crucial role. Measurements at room temperature allow for a more precise estimation of atomic movement. Conversely, conducting measurements at cryogenic temperatures enhances resolution and reduces interactions due to molecular dynamics. This is particularly beneficial for distance measurements.

Pulsed EPR utilizes short bursts of microwave radiation to manipulate the spin system and observe the resulting signal. By varying the duration and timing of these pulses, researchers can probe different time scales and dynamics within the sample. Pulsed EPR offers high time resolution, making it particularly useful for studying rapid processes such as receptor kinetics, enzyme-substrate interactions, and electron transfer reactions in reactive oxygen species. Given that in this thesis we aim at studying the conformation and lipid dependency of a single-pass membrane protein, distance measurements via cwEPR are ideal. EPR relies on three physical given factors: an unpaired electron (with its intrinsic magnetic spin) as a probe, a uniform external magnetic field around the sample, and microwaves as perturbation of and response from the spin probe. The paramagnetic spin of an electron(-probe) is aligned to external magnetic fields. The paramagnetic field of the electron can be aligned in the same - or the opposite - vector of the external magnetic field and has thus two different energy levels. This split in energy levels is called Zeeman effect. If the split occurs through the interaction of electronic spin with the external magnetic field it is sometimes called the Electron Zeeman effect. A further additive splitting of energy levels can occur if the electron is not only interacting with the uniform outer magnetic field but also with the magnetic field of an nearby nucleus; this is sometimes called Nuclear Zeeman effect.

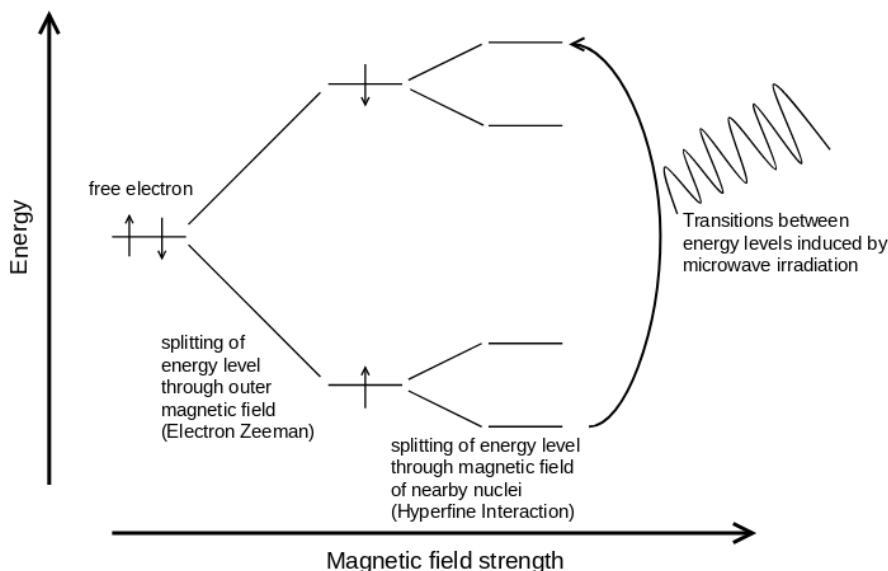


Figure 5: Schematic illustration of the Zeeman effect.

A free electron is aligned to an outer magnetic field, thus resulting in a high and a low energy state. The energy state is further dependent on the magnetic fields of nearby nuclei. If certain criteria are met and an electron is able to "couple", microwave irradiation is able to induce a transition between energy levels. When the criteria for coupling are not met any further, this energy is transmitted in the form of microwaves. Illustration based on (Schosseler 1998).

The difference in energy state of the electron occurring through the Zeeman effect is dependent on the intensity of the applied magnetic field. While increasing the intensity of the magnetic field, the difference between the energy levels widens until it matches the energy of the applied microwave frequency and energy absorption occurs.

If the microwave frequency resonates with an electron, the electron is excited to a higher energy state. As the system relaxes from the perturbation, the absorbed energy from the microwaves is emitted as microwaves and recorded.

The unique EPR spectrum is formed because the ability of an electron to resonate depends on nucleus-electron interactions as well as different molecular conformations and resulting molecular-electron and electron-electron interactions.

An electron only resonates to the microwave perturbation at a certain microwave frequency and matching magnetic field. An EPR sample is fastened in a resonator cavity. As this cavity is attuned to a certain frequency to create a standing microwave, it is practical to use a sweep of magnetic field and not a sweep in frequency to measure EPR spectra.

4 Aim

Maintaining the intricate composition of biological membranes and adapting it to withstand stress and metabolic challenges is a critical function for all cells. Disruptions in lipid homeostasis can result in undesirable levels of lipid saturation, significantly impacting bending rigidity, permeability, and membrane fluidity. Prolonged deviations from lipid homeostasis are linked to chronic endoplasmic reticulum stress, culminating in cell dysfunction and death. Despite its significance, it remains largely unexplored how the UPR transducer PERK senses membrane aberrancies. Understanding the intricate interplay between protein folding and lipid metabolism is crucial, particularly in the context of the UPR. The UPR is pivotal for cellular survival during ER stress and plays a key role in maintaining cellular homeostasis. Investigating the interaction of PERK's transmembrane region with the lipid environment may provide new insights into how cells sense and respond to disturbances in lipid homeostasis. This knowledge is essential for developing strategies to alleviate the impact of UPR-related disorders and underscores the significance of the research on PERK's membrane sensing capabilities.

The goal of this thesis is to characterize the protein-membrane interface and explore the potential membrane sensing capabilities of the human PERK protein. The primary focus is on the transmembrane region of PERK, which consists of a short transmembrane helix adjacent to an amphipathic helix, and its interaction with the surrounding lipid bilayer.

To achieve this goal, several procedures were performed. Site-directed mutagenesis was employed to introduce a cysteine at different positions within the otherwise cysteine-free PERK transmembrane helix. After quality control, *E. coli* strains were transformed with the respective plasmids for protein production. Following *E. coli* cultivation and induction of heterologous overexpression, cells were lysed, the protein of interest was labeled with MTSL and purified through affinity chromatography and later size exclusion chromatography. A key focus of the work was to establish a protocol for reconstituting the specific PERK transmembrane region into previously prepared liposomes to enable *in vitro* studies. A robust and efficient reconstitution protocol was required to facilitate EPR spectroscopy that requires substantial amounts of spin-labeled protein. Through screening multiple protein mutants in various liposome compositions and protein concentrations, a large number of reliable and reproducible EPR data was collected. To automate and standardize EPR data analysis, a Python script should be developed that avoids investigator bias and streamlines EPR data analysis. The goal was to generate a structural model for the juxtamembrane amphipathic helix of PERK and to undertake first steps towards investigating the impact of different lipid environments on the UPR transducer PERK.

5 Materials and equipment

5.1 List of equipment

Table 1: Equipment used in this study.

Name	Source
3D gyratory rocker SSL3	Stuart equipment
4102ST9010 cavity (resonator) (EPR)	Bruker
ÄKTA™ Pure	GE Healthcare
Automatic suction system AA04	Hettich
Avanti JXN-26	Beckman Coulter
Balance	Satorius
Chemical balance	KERN & SOHN GmbH
Deep-freeze Bluperformance	LIEBHERR
Desiccator DN150 Duran	DURAN Group GmbH
Electrophoresis chamber	BioRad
ER042XK microwave bridge (EPR)	Bruker
ESP300e CW-EPR spectrometer at X-band (9.8 GHz) (EPR)	Bruker
FluoroMax™ 4 spectrometer	Horiba Scientific
Fluostar Galaxy™	BMG labtech
Fridge gastro line	LIEBHERR
Gel Doc Imager	BIO-RAD
Heating Block with dual control	Stuart
Heating plate with magnetic stirrer	Heidolph
Hellma™ fluorescence cuvette, Suprasil™ quarts, 100 µl	Sigma-Aldrich
High Efficiency Freezer Ultra-low temperature (-80er)	New Brunswick
Incubator Innova 42	Eppendorf
Labor-Vakuum-System LVS 201 T	WELCH
Microcentrifuge (5415R, 5804R and 5415D)	Eppendorf
Mini-PROTEAN™ Tetra Cell	BioRad
motorized multichannel pipette; 100 µl, 300 µl	Eppendorf
NanoDrop™ ND-1000	PeqLab
Odyssey Imaging System	LI-COR™
PCR thermal cycler	Analytik Jena AG
Pipetboy 2	INTEGRA Biosciences
Pipettes; 10 µl, 50 µl, 200 µl, 1000 µl	Gilson
Roller mixer SRT6	Stuart
Rotator SB2	Stuart
Sonifier for cell disruption	Branson Ultrasonics
Tabletop Ultracentrifuge (Optima™ MAX, TL-100, Optima™ XPN)	Beckman Coulter
TECAN Spark™ multimode microplate reader	TECAN
Thermal shaker	Eppendorf
TransBlot™ Turbo™ transfer system	BioRad
Ultrasonic bath USC900D	VWR
Vortex Genie 2	USA Scientific
Zetasizer Nano-S	Malvern Panalytical

5.2 List of chemicals and reagents

Table 2: List of chemicals and their sources used in this study

Chemical	Source
Bromophenole blue	Carl Roth
DL-Dithiothreitol (DTT)	Sigma-Aldrich
Ethyldiaminetetraacetic acid (EDTA)	Grüssing Analytica
Glycerol 99%	Grüssing Analytica
Glycine 99%	Th.Geyer
HEPES (4-(2-hydroxyethyl)-1-piperazineethanesulfonic acid)	Carl Roth
Hydrochloric acid 37% (HCl)	VWR Chemicals
Magnesium chloride Hexahydrate (MgCl ₂ *6H ₂ O)	Grüssing Analytica
n-Octyl-beta-D-glycopyranoside (β -OG)	EMD Millipore
Piperazine-N,N'-bis(2-ethanesulfonic acid) (PIPES)	Carl Roth
Potassium chloride (KCl)	Grüssing Analytica
Saccharose D (Sucrose)	Carl Roth
Skim milk powder	SUCOFIN
Sodium carbonate (Na ₂ CO ₃)	Grüssing Analytica
Sodium chloride (NaCl)	Fisher scientific
Tris(hydroxymethyl)-aminomethan (Tris)	Sigma-Aldrich
Triton X-100 (TX-100)	Carl Roth
Tween-20	Sigma-Aldrich
Urea	Carl Roth
β -Mercaptoethanol	Sigma-Aldrich

5.3 List of lipids

Table 3: Lipids used in this study. Stocks are stored in chloroform overlaid with nitrogen at -80 °C.

Lipid	Source
1,2-Dioleoyl-sn-glycero-3-phosphocholine (DOPC)	Avanti Polar Lipids
1,2-Dipalmitoyl-sn-glycero-3-phosphocholine (DPPC)	Avanti Polar Lipids
1-Palmitoyl-2-oleoyl-sn-glycero-3-phosphocholine (POPC)	Avanti Polar Lipids
1-Palmitoyl-2-oleoyl-sn-glycero-3-phosphoethanolamine (POPE)	Avanti Polar Lipids
Cholesterol (CHOL)	Avanti Polar Lipids
L- α -phosphatidylinositol (SoyPI)	Avanti Polar Lipids

5.4 List of commercial kits

Table 4: Commercial kits/premade mixtures used in this study.

Name	Source
Bio-Beads™ SM-2 Adsorbent Media	BioRad
CloneAmp™ HiFi PCR Premix	Takara
Deoxynucleotide (dNTP) mix	NEB
DNA loading dye	NEB
GeneRuler™ 1kb DNA Ladder	NEB
In-Fusion™ HD Cloning Kit	Clonetech® Laboratories
InstantBlue™ Protein Stain	Expedeon
Q5™ Site-directed Mutagenesis Kit	NEB
QIAprep Spin Miniprep Kit	Qiagen
QIAquick PCR Purification Kit	Qiagen

5.5 List of consumables

Table 5: List of consumables and their sources used in this study

Name	Source
4-15% Mini PROTEAN™-TGX gels	BioRad
96-well plates; unsterile, black	Brand
Amicon Ultra, Ultracel 30 K, 50 K	Millipore
Amylose resin	NEB
AT 3000 special gas	CFH
Bottletop filter; 0.22 µm, 0.45 µm	BD
Disposable cuvette, semi-micro, 1.5 ml	VWR
Falcon tubes; 15 ml, 50 ml	Greiner
Inoculation loops	VWR
Microcentrifuge tubes (0.2 ml, 1.5 ml, 2 ml)	Roth, Eppendorf, Greiner, Starlab
Nitrocellulose membrane 0.45 µm	Fisher Scientific
Nunc™ cryogenic tubes; 1.8 ml	VWR
PD-10 column	GE Healthcare
Pipette tips, refill (10 µl, 200 µl, 1000 µl)	VWR, Roth, Starlab
Ringcaps 50 µl	Hirschmann
Serological pipettes (2 ml, 5 ml, 10 ml, 25 ml, 50 ml)	VWR
Sterican™ disposable needle (0.80 x 40 mm; 0.60 x 30 mm; 0.45 x 20 mm)	Braun
Sterile culture tubes with cap; 14 ml	VWR
Sterile Petri dishes (ø 90 mm)	VWR
Superdex 200 10/300 increase column	GE Healthcare
Vacuum filtration system (150 ml, 0.2 µm)	VWR
Vivaspin 2, (MWCO 30,000 kDa, 50,000 kDa)	Satorius, GE Healthcare

5.6 List of enzymes

Table 6: Enzymes used in this study, stored at -20 °C.

Name	Source
Benzonase	Sigma-Aldrich
<i>DpnI</i>	NEB
TEV	Toni Radanovic

5.7 List of probes and dyes

Table 7: Probes and fluorescent dyes used in this study.

Name	Source
C-laurdan (CL)	2p probes
Hoechst 33342	Sigma-Aldrich
MTS ((1-Oxyl-2,2,5,5-tetramethylpyrroline-3-methyl) methanethiosulfonate)	Enzo Life Sciences

5.8 List of antibodies

All antibodies used for detection by immunoblotting are listed in Table 8. Antibodies were prepared in a solution of 4% skimmed milk powder dissolved in TBS-T. Primary antibody solutions were reused and stored for up to 1-2 weeks at 4 °C. Secondary antibody solutions were discarded after one time use.

Table 8: Antibodies used in this study.

Primary Antibody	Dilution	Source
Anti-MBP monoclonal (mouse)	1:30.000	NEB
Secondary Antibody	Dilution	Source
Anti-mouse-IRDye TM IgG 680LT (goat)	1:15.000	LI-COR TM
Anti-mouse-IRDye TM IgG 800CW (goat)	1:15.000	LI-COR TM

5.9 List of primers

Table 9: Table of forward (fwd) and reverse (rev) primers for Quikchange™ site-directed mutagenesis (SDM) of point mutations of PERK-TMR constructs used in this work. For more information see 6.3.1 .

Name	Sequence (5' → 3')	Description
PP1	CCT GTT CTT CTT TTA CAC TGT TGG AAA GAA ATA GTT GC	W521C (fwd)
PP2	GCA ACT ATT TCT TTC CAA CAG TGT AAA AGA AGA ACA GG	W521C (rev)
PP3	CGC TAG CGA ATT CAA AAA GTG TCC TGT TCT TCT TTT ACA CTG G	D514C (fwd)
PP4	CCA GTG TAA AAG AAG AAC AGG ACA CTT TTT GAA TTC GCT AGC G	D514C (rev)
PP5	GCG AAT TCA AAA AGG ATT GTG TTC TTC TTT TAC ACT GG	P515C (fwd)
PP6	CCA GTG TAA AAG AAG AAC ACA ATC CTT TTT GAA TTC GC	P515C (rev)
PP7	CGA ATT CAA AAA GGA TCC TTG TCT TCT TTT ACA CTG GTG G	V516C (fwd)
PP8	CCA CCA GTG TAA AAG AAG ACA AGG ATC CTT TTT GAA TTC G	V516C (rev)
PP9	CAA AAA GGA TCC TGT TTG TCT TTT ACA CTG GTG G	L517C (fwd)
PP10	CCA CCA GTG TAA AAG ACA AAC AGG ATC CTT TTT G	L517C (rev)
PP11	GAT CCT GTT CTT TGT TTA CAC TGG TGG	L518C (fwd)
PP12	CCA CCA GTG TAA ACA AAG AAC AGG ATC	L518C (rev)
PP13	GAT CCT GTT CTT CTT TGT CAC TGG TGG AAA GAA ATA G	L519C (fwd)
PP14	CTA TTT CTT TCC ACC AGT GAC AAA GAA GAA CAG GAT C	L519C (rev)
PP15	GAT CCT GTT CTT CTT TTA TGC TGG TGG AAA GAA ATA GTT GC	H520C (fwd)
PP16	GCA ACT ATT TCT TTC CAC CAG CAT AAA AGA AGA ACA GGA TC	H520C (rev)
PP17	GCG AAT TCA AAT GTG ATC CTG TTC	K513C (fwd)
PP18	GAA CAG GAT CAC ATT TGA ATT CGC	K513C (rev)
PP19	GCT AGC GAA TTC TGC AAG GAT CCT G	K512C (fwd)
PP20	CAG GAT CCT TAC AGA ATT CGC TAG CG	K512C (rev)
PP21	CTT TTA CAC TGG TGT AAA GAA ATA GTT GC	W522C (fwd)
PP22	GCA ACT ATT TCT TTA CAC CAG TGT AAA AG	W522C (rev)
PP27	CTT TTA CAC TGG TGG TGT GAA ATA GTT GC	K523C (fwd)
PP28	GCA ACT ATT TCA CAC CAC CAG TGT AAA AG	K523C (rev)
PP29	CTG GTG GAA ATG TAT AGT TGC AAC G	E524C (fwd)
PP30	CGT TGC AAC TAT ACA TTT CCA CCA G	E524C (rev)

Table 10: Table of forward (fwd) and reverse (rev) primers for Q5™ SDM of point mutations of PERK-TMR constructs used in this work. For more information see 6.3.3 .

Name	Sequence (5' → 3')	Description
PP31	ACA CTG GTG GTG TGA AAT AGT TGC AAC	K523C (fwd)
PP32	AAA AGA AGA ACA GGA TCC	K523C (rev)

Table 11: Table of forward (fwd) and reverse (rev) primers for In-Fusion™ SDM of point mutations of PERK-TMR constructs used in this work. For more information see 6.3.2 .

Name	Sequence (5' → 3')	Description
PP41	GAA AGA ATG TGT TGC AAC GAT TTT GTT TTC TAT CA	I525C (fwd)
PP42	GCA ACA CAT TCT TTC CAC CAG TGT AAA AGA AGA	I525C (rev)
PP43	AGA AAT ATG TGC AAC GAT TTT GTT TTC TAT CA	V526C (fwd)
PP44	GTT GCA CAT ATT TCT TTC CAC CAG TGT AAA AGA	V526C (rev)
PP45	AAT AGT TTG TAC GAT TTT GTT TTC TAT CAT AGC AA	A527C (rev)
PP46	ATC GTA CAA ACT ATT TCT TTC CAC CAG TGT	A527C (rev)
PP47	AGT TGC ATG TAT TTT GTT TTC TAT CAT AGC AAC A	T528C (rev)
PP48	AAA ATA CAT GCA ACT ATT TCT TTC CAC CAG TG	T528C (rev)

Table 12: Table of forward (fwd) and reverse (rev) primers for sequencing PERK-TMR constructs used in this work. For more information see 6.7.

Name	Sequence (5' → 3')	Origin
LacOp-for (fwd)	CGG ATA ACA ATT TCA CAC AG	Seqlab standard primer
M13F43 (rev)	AGG GTT TTC CCA GTC ACG ACG TT	Eurofins standard primer
malE (fwd)	GGT CGT CAG ACT GTC GAT GAA GCC	Eurofins standard primer
TP 130 (rev)	CAG ACC GCT TCT GCG TTC TG	constructed by Tina Halbleib

5.10 List of plasmids

The minimal PERK-TMR construct -consisting of a maltose-binding protein (MBP)-tag, a polyN linker, a *Tobacco Etch Virus* (nuclear-inclusion-a endopeptidase) (TEV) cleavage site and the predicted TMR region of PERK- was provided by Kristina Pesek. It was generated by her in cooperation with Julian Bruckert during his bachelor thesis by annealing, phosphorylating and cloning the PERK TMR encoding oligonucleotides into the pMAL-C2x TEV *E. coli* expression vector using EcoRI/HindIII restriction sites (Bruckert 2016).

This original construct was further mutagenized by site-directed mutagenesis. All established constructs are listed in Table 13, the primer pairs used for PCR reactions are listed in Table 9, 10 and 11.

Table 13: Table of plasmids used and constructed in this study.

Name	Description	Source
pKP116	MBP-PERK AH+TMH + Rest native cysteine	Provided by Kristina Pesek
pKP120	MBP-PERK AH+TMH + Rest cys-less	Provided by Kristina Pesek
pPP12	MBP-PERK AH+TMH + Rest cys-less K512C	This study
pPP11	MBP-PERK AH+TMH + Rest cys-less K513C	This study
pPP3	MBP-PERK AH+TMH + Rest cys-less D514C	This study
pPP4	MBP-PERK AH+TMH + Rest cys-less P515C	This study
pPP5	MBP-PERK AH+TMH + Rest cys-less V516C	This study
pPP6	MBP-PERK AH+TMH + Rest cys-less L517C	This study
pPP7	MBP-PERK AH+TMH + Rest cys-less L518C	This study
pPP8	MBP-PERK AH+TMH + Rest cys-less L519C	This study
pPP9	MBP-PERK AH+TMH + Rest cys-less H520C	This study
pPP2	MBP-PERK AH+TMH + Rest cys-less W521C	This study
pPP13	MBP-PERK AH+TMH + Rest cys-less W522C	This study
pPP16	MBP-PERK AH+TMH + Rest cys-less K523C	This study
pPP17	MBP-PERK AH+TMH + Rest cys-less E524C	This study
pPP19	MBP-PERK AH+TMH + Rest cys-less I525C	This study
pPP20	MBP-PERK AH+TMH + Rest cys-less V526C	This study
pPP21	MBP-PERK AH+TMH + Rest cys-less A527C	This study
pPP22	MBP-PERK AH+TMH + Rest cys-less T528C	This study

5.11 List of *E. coli* strains

Table 14: *E. coli* strains used in this study.

Name	Genotype
Dh5 α	F- Φ 80lacZ Δ M15 Δ (lacZYA-argF) U169 recA1 endA1 hsdR17 (rK- mK+) phoA supE44 λ - thi-1 gyrA96 relA1
TOP10	F- mcrA Δ (mrr-hsdRMS-mcrBC) Φ 80lacZ Δ M15 Δ lacX74 recA1 araD139 Δ (araleu)7697 galU galK rpsL (StrR) endA1 nupG
HST08	F-, endA1, supE44, thi-1, recA1, relA1, gyrA96, phoA, Φ 80d lacZ Δ M15, Δ (lacZYA-argF) U169, Δ (mrr-hsdRMS-mcrBC), Δ mcrA, λ -
BL21(DE3)pLysS	F- ompT hsdSB (rB-mB-) gal dcm (DE3)pLysS (CamR)
BL21-CodonPlus(DE3)-RIL	F- ompT hsdS(rB-mB-) dcm+TetRgal λ (DE3) endAhte [argU ileY BB leuWCam ^R]

5.12 List of media for *E. coli* cultivation

Table 15: Media for cultivation of *E. coli* Overview of Buffer compositions used in this work.

Name	Compositions
LB _{amp}	1% (w/v) Tryptone, 0.5% (w/v) Yeast Extract, 1% (w/v) NaCl, 100 µg/ml Ampicillin
LB _{Chloramphenicol}	1% (w/v) Tryptone, 0.5% (w/v) Yeast Extract, 1% (w/v) NaCl, 100 µg/ml Ampicillin, 34 µg/ml Chloramphenicol
LB _{plain}	1% (w/v) Tryptone, 0.5% (w/v) Yeast Extract, 1% (w/v) NaCl
LB _{rich}	1% (w/v) Tryptone, 0.5% (w/v) Yeast Extract, 1% (w/v) NaCl, 0.2% (w/v) Glucose
SOB	2% (w/v) Tryptone, 0.5% (w/v) Yeast Extract, 10 mM NaCl, 2.5 mM KCl, 10 mM MgSO ₄
SOC	20 mM Glucose in SOB medium
in plated form:	+ 2% (w/v) Agar in according medium

5.13 List of buffers

Table 16: Buffers used in this work. Overview of buffer compositions used in this work.

Name	Compositions
5x Membrane Sample Buffer, reducing (MSB _{red})	0.1 M Tris-HCl pH 6.8, 8 M urea, 5 mM EDTA, 3.2% (w/v) SDS, 0.15% (w/v) bromphenol blue, 4% (v/v) glycerol, 4% (v/v) β -mercaptoethanol
5x Membrane Sample Buffer, non reducing (MSB _{non-red})	0.1 M Tris-HCl pH 6.8, 8 M urea, 5 mM EDTA, 3.2% (w/v) SDS, 0.15% (w/v) bromphenol blue, 4% (v/v) glycerol
Blocking Buffer	4% (w/v) skimmed milk powder in TBS-T
Blotting Buffer	25 mM Tris-HCl pH 8.3, 190 mM glycine, 20% methanol
Column Buffer	50 mM HEPES pH 7.4, 150 mM NaCl, 1 mM EDTA
Column Wash Buffer	50 mM HEPES pH 7.4, 150 mM NaCl, 1 mM EDTA, 50 mM β -OG
Elution Buffer	50 mM HEPES pH 7.4, 150 mM NaCl, 1 mM EDTA, 50 mM β -OG, 10 mM Maltose
Elution Buffer _{50%-Glyc}	50 mM HEPES pH 7.4, 150 mM NaCl, 1 mM EDTA, 50 mM β -OG, 10 mM Maltose, 50% (w/v) Glycerol
Elution Buffer _{Glyc}	50 mM HEPES pH 7.4, 150 mM NaCl, 1 mM EDTA, 50 mM β -OG, 10 mM Maltose, 20% (w/v) Glycerol
Lysis Buffer	50 mM HEPES pH 7.4, 150 mM NaCl, 1 mM EDTA, 2 mM DTT, 5 U/ml Benzonase, Protease Inhibitor Cocktail (10 μ g/ml Chymostatin, 10 μ g/ml Antipain, 10 μ g/ml Pepstatin)
Neutralization Buffer	200 mM HEPES pH 7.0, 150 mM NaCl
Reconstitution Buffer	20 mM HEPES, pH 7.4, 150 mM NaCl
Reconstitution Buffer _{Glyc}	20 mM HEPES, pH 7.4, 150 mM NaCl, 5% (w/v) Glycerol
Running Buffer	25 mM Tris-HCl pH 8.3, 190 mM glycine, 0.1% SDS
SEC Buffer	50 mM HEPES pH 7.4, 150 mM NaCl, 1 mM EDTA, 50 mM β -OG
TAE Buffer	40 mM Tris-Acetate, 1 mM EDTA, pH 8.0
TB buffer	10 mM PIPES, 55 mM MnCl ₂ , 15 mM CaCl ₂ , 250 mM KCl; pH 6.7
TBS-T	20 mM Tris-HCl pH 8.0, 150 mM NaCl, 0.2% (v/v) Tween 20
Wash Buffer	50 mM HEPES pH 7.4, 150 mM NaCl, 1 mM EDTA, 50 mM β -OG
Wash Buffer _{Glyc}	50 mM HEPES pH 7.4, 150 mM NaCl, 1 mM EDTA, 50 mM β -OG, 20% (w/v) glycerol

6 Methods

6.1 Cultivation and storage of *E. coli*

Competent *E. coli* strains were cultivated to provide an amplification of plasmids or an expression of PERK-TMR constructs. Cells were cultivated in liquid cultures at 37°C and under constant agitation or on solid lysogeny broth (LB)-agar plates unless otherwise noted. Antibiotics (100 µg/ml ampicillin +/- 34 µg/ml chloramphenicol) warrant selection and cultivation of only plasmid-bearing cells.

For long term storage of *E. coli* cells, 5 ml cultures were cultivated overnight. 500 µl of the resulting stationary cell suspension were mixed with 400 µl of 50% (weight per volume (w/v)) glycerol and stored at -80°C for further use.

6.2 Preparation of chemically competent *E. coli*

Competent cells of the strains BL21(DE3)pLysS, DH5 α , HST08, or TOP10 were generated according to protocol established by Inoue et al. (Inoue, Nojima, Okayama 1990).

An aliquot of *E. coli* cells was thawed on ice and used to inoculate 4 ml of Super Optimal Broth (SOB) media. After overnight cultivation, 200 µl of the preculture were used to inoculate a main culture in 100 ml SOB medium. The main culture was cultivated until an optical density (OD)₆₀₀ of 0.5 was reached. The cells were harvested by centrifugation (4,000x g, 10 min, 4°C), resuspended in 16 ml ice-cooled transformation buffer (TB) and the cells collected (4,000x g, 10 min, 4°C). The Pellet was resuspended in 10 ml pre-cooled TB, which was supplemented with 700 µl dimethyl sulfoxide (DMSO). Aliquots of 100 µl were snap frozen in liquid nitrogen and stored at -80°C.

6.3 Site-directed mutagenesis

For the insertion of single cysteines into the PERK-TMR different protocols were used.

6.3.1 QuikChange™ site-directed mutagenesis

For site-directed mutagenesis (SDM) the QuikChange™ methode from Stratagene was used. It relies on two complementary oligonucleotide primers that differ by up to six nucleotides from the template DNA. The differing nucleotides get flanked by up to 20 homologeous nucleotides to assure the binding to the original template DNA. The forward and reverse primers are listed in table 9, the standard reaction mixture can be see in table 17 and the cycling parameters in table 18.

Table 17: Standard reaction mixture for Quikchange™ SDM.

Template (20-50 ng)	x µl
Forward Primer (10 µmol/µl)	2.5 µl
Reverse Primer (10 µmol/µl)	2.5 µl
5x HF Buffer	10 µl
dNTP's (10 mM)	1.25 µl
Phusion™ DNA Polymerase	0.5 µl
autoclaved ddH ₂ O	ad final volume
Final Volume	50 µl

Table 18: Standard reaction conditions for Quikchange™ SDM.

Step	Time	Temperature [°C]
Initial Denaturation	30 s	98
Denaturation	10 s	98
Primer Annealing	20 s	55
Elongation	1 min/kb	72
Final Elongation	20 min	72
Cycles Denaturation → Elongation	30x	

The non-mutated, methylated template DNA was removed from the final product by incubating the reaction mixture with 10 units of *DpnI* for 3 hours at 37 °C.

1 µl of the reaction product was used to transform chemically competent *E. coli* cells (6.5). The success of the mutagenesis and the integrity of the resulting protein-coding sequence was verified by DNA sequencing (6.7).

6.3.2 In-Fusion™ site-directed mutagenesis

The In-Fusion™ (Takara) SDM relies on inverse polymerase chain reaction (PCR). It depends on two primers with a 15 base pair (bp) overlap at the 5' site, which also contains the mutation of interest. Primers used for this method were designed by the Takarabio Primer Design Tool and are listed in Table 11, the standard reaction mixture can be seen in Table 19 and the cycling parameters in Table 20.

Table 19: Standard reaction mixture for In-Fusion™ SDM.

Template (20-50 ng)	x µl
Forward Primer (10 µmol/µl)	0.75 µl
Reverse Primer (10 µmol/µl)	0.75 µl
CloneAmp HiFi PCR Premix	12.5 µl
dNTP's (10 mM)	1.25 µl
autoclaved ddH ₂ O	ad final volume
Final Volume	25 µl

Table 20: Standard reaction conditions for In-Fusion™ SDM.

Step	Time	Temperature [°C]
Hot Start	30 s	98
Denaturation	10 s	98
Primer Annealing	15 s	61
Elongation	30 sec/kb	72
Final Elongation	10 min	72
Cycles Denaturation → Elongation	30x	

To further increase the yield of recombinant clones, the PCR mixture was treated with Cloning Enhancer™. 2 µl of Cloning Enhancer™ was mixed with 5 µl PCR reaction and incubated at first at 37 °C for 15 min and then at 80 °C for 15 min.

7 µl of the final product was used to transform chemically competent HST08 *E. coli* cells (6.5). The mutagenesis was verified by DNA sequencing (6.7).

6.3.3 Q5™-Phusion site-directed mutagenesis

For the site-directed mutagenesis via the Q5™-Phusion polymerase, non-overlapping primers were used, from which only one of the primers contains the mutation at the 5' end. The Q5™ Site-Directed Mutagenesis Kit (NEB) was used according to the manual of the manufacturer. The primers were designed with help of the online NEB Basechanger Tool. The primer pairs used for Q5™-Phusion SDM are listed in Table 10, the standard reaction mixture can be see in Table 21 and the cycling parameters in Table 22.

Table 21: Standard reaction mixture for Q5™ SDM.

Template (1-10 ng)	x µl
Forward Primer (10 µmol/µl)	2.5 µl
Reverse Primer (10 µmol/µl)	2.5 µl
5x Q5 Reaction Buffer	10 µl
dNTP's (10 mM)	1 µl
Q5 High-Fidelity DNA Polymerase	0.5 µl
autoclaved ddH ₂ O	ad final volume
Final Volume	50 µl

Table 22: Standard reaction conditions for Q5™ SDM.

Step	Time	Temperature [°C]
Initial Denaturation	30 s	98
Denaturation	10 s	98
Primer Annealing	20 s	50-72 (calculated with NEBTm Tool)
Elongation	30 s/kb	72
Final Elongation	10 min	72
Cycles Denaturation → Elongation	30x	

To remove non-mutated template DNA, mutagenesis was followed by a kinase, ligase and *DpnI*, (KLD) treatment: 1 µl of the PCR reaction was mixed with 5 µl 2x KLD Reaction Buffer,

1 μ l 10x KLD Enzyme Mix -provided with the commercial kit-, and 3 μ l autoclaved ddH₂O and incubated for 15 min at room temperature.

5 μ l of the KLD product was used to transform chemically competent *E. coli* cells (6.5). The mutagenesis was verified by DNA sequencing (6.7).

6.4 Agarose gel electrophoresis

To separate DNA fragments according to their length, DNA containing samples were mixed with 6x DNA loading dye (NEB) and subjected to a gel consisting of 1% (w/v) agarose in TRIS-Acetate-EDTA (TAE) buffer. Electrophoresis was performed by applying 100-140 V for 50 min. To visualize the DNA, it was stained in an ethidium bromide (0.5 μ g/ml) bath for 30 min.

6.5 Transformation of *E. coli*

50 μ l of competent *E. coli* cells were thawed and incubated for 30 min on ice with 50-100 ng plasmid DNA or PCR product from a mutagenesis. The cells were heat-shocked by incubating at 42 °C for 60 seconds, 600 revolutions per minute (rpm) shaking and cooled down on ice for 2 minutes to induce the uptake of DNA. Cells were resuspended in 1 ml LB_{plain} medium and cultivated for 60 min at 600 rpm. The cells were pelleted by centrifugation (3.000x g, 5 min, room temperature (20-26 °C) (RT)) and the supernatant discarded.

The resulting pellet was resuspended in residual LB_{plain} medium and plated on selective agar plates. This LB-agar plates contained 100 μ g/ml ampicillin if cultivating DH5alpha, HST08, or TOP10 cells or 100 μ g/ml ampicillin and 34 μ g/ml chloramphenicol in the case of BL21 cells. LB-Agar plates were incubated until single colonies became visible: overnight at 37 °C or after 3 days at room temperature.

6.6 Plasmid isolation

The QIAprep Spin Miniprep Kit (Qiagen) was used for *E. coli* plasmid DNA preparation. To this end, a single colony of either plasmid-containing DH5alpha, HST08, or TOP10 cells was used to inoculate 5 ml LB_{Ampicillin (amp)} medium. After overnight cultivation the plasmid preparation was carried out according to the manufacturer's instruction - including all optional washing steps. The DNA yield and purity was determined by ultraviolet/visible light (UV/Vis) measurements at 260 nm using a NanoDropTM photospectrometer.

6.7 DNA sequencing

The DNA sequencing was performed by Microsynth Seqlab (Göttingen) or Eurofins Genomics (Ebersberg). For this 200 ng DNA were premixed with an appropriate sequencing primer at a final concentration of 2 μ M and adjusted to a total volume of 10 μ l with ddH₂O. The oligonucleotide primers used for sequencing are listed in Table 12 .

6.8 Heterologous production of PERK-TMR proteins in *E. coli*

The heterologous expression of MBP fusion proteins was based on established protocols with minor modifications (Halbleib et al. 2017; Contreras et al. 2012). In this study we only used

human-derived PERK-TMR minimal constructs.

Chemically competent *E. coli* BL21(DE3)pLysS cells were transformed using respective plasmids (Table 13). LB_{Chloramphenicol} was inoculated using a single colony from sequenced glycerol stock and cultivated overnight. This preculture was diluted 1:50 in 0.5 l, 1 l or 2 l LB_{rich} medium (LB supplemented with 2% glucose) for 2-3 h until an OD₆₀₀ of 0.6 was reached. Isopropyl β -D-1-thiogalactopyranoside (IPTG) was supplemented to a final concentration of 0.3 mM to induce gene expression. The cells were harvested by centrifugation (20 min, 4.000x g, 4 °C) after being cultivated for 3 h. The cell pellet was resuspended in ice-cold phosphate-buffered saline (PBS) and stored at -20 °C until further use.

6.9 Preparation of amylose resin

5 ml of amylose resin (NEB) slurry was washed with 20 ml H₂O by rotating for 5 min and centrifugation (10 min, 3,000x g, 4 °C) and decanting and discarding the supernatant carefully. These washing steps were repeated with Column Wash Buffer.

6.10 Purification and labeling of MBP-transmembrane helix (TMH) constructs by affinity chromatography

All following steps were carried out at 4 °C in a cold room, or on ice in a water bath: The cell pellet from 1 l bacterial culture (see 6.8) was resuspended in 36 ml Lysis Buffer. The cells were disrupted by sonification (4x 30s, power 30%, pulse 0.7 s/ 0.3 s, 45 s pause after every sonification). To solubilize the membranes the sample was mixed with octyl-beta-glucosid (β -OG) to a final concentration of 50 mM and incubated for 15 min at 4 °C on a rotator. Unsolubilized material was pelleted (60 min, 100,000x g, 4 °C) and the clear supernatant applied to 5 ml of washed amylose resin (NEB) (see 6.9). After incubation (15 min, 4 °C) to allow the binding of the MBP-fusion protein to the amylose matrix, the supernatant with unbound material was removed from the amylose resin using gravity columns. Unbound or unspecifically bound proteins were removed with 26 column volumes of Column Wash Buffer. The protein was either directly eluted or labeled overnight.

The 1-Oxyl-2,2,5,5-tetramethyl-3-pyrroline-3-methyl)methanethiosulfonate (MTS) spin label is light sensitive. The labeling process and the labeled protein were handled under avoidance of direct or bright light and whenever possible shielded with aluminium foil.

A single cysteine containing protein was spinlabeled overnight on an amylose column with 1 mM MTS in a total volume of 4 ml Column Wash Buffer under constant agitation 4 °C. To remove unreacted MTS spin label the column was washed with 13 column volumes of Column Wash Buffer.

PERK-TMR proteins were eluted with Elution Buffer in up to 6 consecutive elution steps (1 ml Elution Buffer, 60 s incubation, elution from the column by gravity). The first elution step, using only 0.5 ml Elution Buffer, was discarded. The purity and concentration of resulting elution fractions were determined using a NanoDropTM spectrophotometer by absorption measurements at 280 nm.

6.11 Size-exclusion chromatography

Size-exclusion chromatography (SEC) separates proteins according to their molecular size and weight. It was used 1.) to remove impurities and aggregates as well as dimers from a protein sample (from 6.10) 2.) to change the buffer environment of a protein sample, and 3.) to reestablish an uniform buffer environment after concentrating a protein sample.

For all ends, the Superdex™ 200 10/300 increase column (24 ml bed volume, GE Healthcare), utilizing a Äkta Pure™ (GE Healthcare) fast protein liquid chromatography system with filtered and degassed SEC buffer, was used with a constant flow rate of 0.5 ml/min. For preparative runs a 500 µl loop, for analytical runs a 100 µl loop was utilized with respective sample volumina used. The separation was monitored by the absorption at 280 nm. 500 µl fractions were collected from the elution fraction.

Before loading the protein sample was concentrated via Amicon centrifugal filters (50 kDa molecular weight cut off). Possible aggregates were removed by centrifugation (20,000x g, 10 min, 4 °C).

Fractions of purified protein were adjusted to 20% (w/v) glycerol, using a Elution Buffer_{50%-Glyc}, ensuring that the contents of the other buffer ingredients remained stable. Protein content was adjusted with Elution Buffer_{Glyc}.

6.12 Preparation of liposomes

Lipids dissolved in chloroform as indicated in Table 23 were mixed in a 2 ml original Eppendorf centrifugation tube to yield a lipid mixture of choice. The following lipids were used to obtain lipid mixtures of choice: 1-palmitoyl-2-oleoyl-*sn*-glycero-3-phosphocholine (POPC), 1,2-dioleoyl-*sn*-glycero-3-phosphocholine (DOPC), cholesterol, 1,2-dipalmitoyl-*sn*-glycero-3-phosphocholine (DPPC), 1-palmitoyl-2-oleoyl-*sn*-glycero-3-phosphoethanolamine (POPE), and L- α -phosphatidylinositol [from Soy plant] (Soy PI).

The lipids were dried under a constant stream of nitrogen in a thermomixer (60 °C, 800 rpm). Residual chloroform was removed by applying a vacuum in a desiccator for 1 h at RT. The lipid cake was rehydrated using 1 ml of Reconstitution Buffer under constant agitation in a thermomixer (60 °C, 800 rpm). The resulting large multilamellar liposomes were sonified at power-level 9 in a USC900D ultrasonic cleaning waterbath (VWR) at 60 °C for 20 min. The resulting liposomes were adjusted to a final lipid concentration of 10 mM by adding the corresponding volume of Reconstitution Buffer. The resulting liposomes were aliquoted, snap frozen in liquid nitrogen and stored at -80 °C.

Table 23: Lipids mixtures for liposome preparation with a 10 mM lipid concentration.

Lipid stock (20 mg/ml)	POPC [μl]	DOPC [μl]	Cholesterol [μl]	POPE [μl]	DPPC [μl]	SoyPI [μl]	Buffer [μl]
POPC	500.0	-	-	-	-	-	317
DOPC POPC	245.8	254.2	-	-	-	-	273
POPC Chol	443.6	-	56.4	-	-	-	460
POPE 20	149.1	257.0	-	93.9	-	-	309
POPE 40	50.3	259.9	-	189.9	-	-	323
CHO2	52.6	-	26.7	198.8	101.6	120.1	386
Cholesterol 5	239.5	247.7	12.8	-	-	-	327
Cholesterol 10	232.9	240.8	26.3	-	-	-	362
Cholesterol 20	218.4	226.0	55.6	-	-	-	438
Cholesterol 30	202.4	209.3	88.3	-	-	-	523
Soy 10	194.0	250.7	-	-	-	55.3	277
Soy 20	143.5	247.4	-	-	-	109.1	259
Soy 30	94.4	244.1	-	-	-	161.5	243

6.13 Testing lipid density by C-Laurdan fluorescence spectroscopy

C-Laurdan is a probe which intercalates into lipid bilayers. It is sensitive to the polarity of its nanoenvironment and changes its emission spectrum depending on the degree of water permeation of the bilayer (Kaiser, Lingwood, et al. 2009). A high permeation of water into the lipid bilayer indicative for loose lipid packing causes a shift of the emission spectrum towards 485 nm. A densely packed membrane with a low degree of water permeation causes a shift of the emission peak to around 440 nm.

From the C-Laurdan spectrum the generalized polarization (GP) value can be calculated (see Equation 1). It is calculated using the ratio of the integrals of fluorescence intensity from 400-460 nm (I_{Chl1}) and 470-530 nm (I_{Chl2}). The GP value is a measure of the membrane order and could theoretically range from -1 (less ordered state) to +1 (most ordered state) (Kaiser, Lingwood, et al. 2009). The GP value is an instrument-specific, semiquantitative value.

$$GP = \frac{I_{Chl1} - I_{Chl2}}{I_{Chl1} + I_{Chl2}} \quad (1)$$

In this study, liposomes (corresponding to 0.33 mM lipids) were mixed with 0.4 μM C-Laurdan in 150 μl reconstitution buffer. The mixture was incubated for 5 min at 30 °C and excited with an excitation wavelength of 375 nm (3 nm bandwidth) in a quartz cuvette. The emission spectrum was recorded from 400-600 nm (3 nm bandwidth) and a blank measurement, recorded without C-Laurdan dye, was subtracted.

6.14 Preparation of SM-2 Biobeads™

To activate the SM-2 Biobeads™ they were washed twice with 10-fold volume of methanol (e.g. 4 g Biobeads™, 40 ml methanol), further twice more with 10-fold volume of ddH₂O as well as once with 10-fold volume of reconstitution buffer by rotating for 10 min. The used solvent was removed

by a syringe and cannula (\varnothing 0,60 mm) after each washing step. The biobeads were aliquoted for one reconstitution step and stored at 4 °C.

Beads were stored at the end of the second ddH₂O washing step for up to one week at 4 °C if not used on the same day.

6.15 Reconstitution of PERK-TMR proteins in liposomes

Purified and spin-labeled protein was reconstituted in liposomes with defined lipid compositions. Different molar protein-to-lipid ratios (P:L) were utilized. 207.6 μ l liposomes (10 mM of lipids) were mixed with 33.3 μ l protein (20.77 μ M) (for a P:L of 1:3000) or 200 μ l protein (for a P:L of 1:500) in Reconstitution Buffer. The mixture was adjusted to a final concentration of 37.5 mM β -OG and a final volume of 1 ml. The sample was incubated for 10 min at room temperature on a rotator to fully solubilize the liposomes. The detergent was removed by adding at first 400 mg of activated BioBeads™ and incubating for 90 min at RT on a rotator, then by repeating the incubation in a fresh tube containing 100 mg Biobeads™. To transfer the sample, a syringe and cannula (\varnothing 0,60 mm) were used. The proteoliposomes were harvested by centrifugation (575,000x g, 16 h, 4 °C). Centrifugation tubes were marked on the outwards facing edge before centrifugation. This aids in locating the hardly visible pellets.

The resulting pellet was resuspended in Reconstitution Buffer_{Glyc} (20 mM 4-(2-hydroxyethyl)-1-piperazineethanesulfonic acid (HEPES), pH 7.4, 150 mM NaCl, with 5% (w/v) glycerol) to a final volume of 50 μ l. The proteoliposomes were transferred into an EPR tube, snap frozen in liquid nitrogen and stored at -80 °C or liquid nitrogen during transport.

6.16 Electron paramagnetic resonance (EPR) spectroscopy

Room temperature (RT) spectra were recorded by an ESP300e, X-Band 9,5 GHz spectrometer manufactured by the company Bruker. The spectrometer was supplemented with a frequency counter (HP 5130A), an NMR gaussmeter (Bruker), a signal channel, and a computer containing all the spectrometer parameters for measurement (see Table 24). A 4102st cavity resonator and the continuous-wave (CW) mode were used for testing.

For measuring low temperature (-196 °C) (LT) spectra, a fully equipped Elexsy 600-spectrometer by Bruker was used in continuous-wave (CW) mode with 9.5 GHz and a ST cavity resonator.

RT and LT continuous-wave electron paramagnetic resonance (cwEPR) spectra were recorded in one recording session.

For measurements at LT, 707-SQ-250M clear fused quartz tubes (rototec-spintec/wilmad-labglass) were used, with a total length of 250 mm. In preparation the tubes were halved using a glass cutter and the ends closed by melting with an AT 3000 special gas (CFH) flame. Samples were transferred into the LT EPR tube using a micro syringe pipette (Hamilton) and plastic tubing.

Samples stored at -80 °C in LT EPR tubes were transported and stored in liquid nitrogen. Each tube was wiped clean from ice crystals before measuring. The tubes were breathed upon before transferring them into the with liquid nitrogen filled LT cavity resonator. This leads to the forming of small and homogeneous ice crystals, which improve signal quality. The tube was further locked in place to reduce noise caused by nitrogen bubbles.

Table 24: Default recording options for EPR spectra.

Parameter	RT	LT
numbers of scans []	8	12
data points []	1024	1024
center field [Gauss]	3490	3390
field sweep width [Gauss]	60	160
sweeping speed [s]	61.44	81.92
modulation amplitude [Gauss]	2.02	5.0
modulations frequency [kHz]	100	100
conversion time [ms]	60	80
time constant [ms]	40.96	40.96
receiver gain [dB]	60	60
attenuation [dB]	10	10
power [mW]	20	20
microwave power []	non saturating	non saturating

After recording the LT spectra, the sample was thawed and transferred to 50 μ l capillary tubes (ringcapsTM by Hirschmann). The capillary tubes were sealed with haematocrit capillary sealing wax (Hirschmann), positioned into the cavity resonator and the RT spectrum was recorded.

6.17 SDS-polyacrylamide gel electrophoresis

To separate proteins by their molecular weight, discontinuous sodium dodecyl sulfate polyacrylamide gel electrophoresis (SDS-PAGE) was performed.

Two buffer environments for the samples were chosen: the 5x Membrane Sample Buffer (MSB)_{red} buffer to reduce cysteine oxidation and disulfide bridges and the 5x MSB_{non-red} buffer to examine the effects of cysteines.

For InstantBlueTM staining a final content of 0.1 OD equivalents or 1 μ g protein per lane and for immunoblotting a final protein content of 2-5 ng protein per lane was intended.

Samples were mixed 5:1 with the according buffer and denaturated (5 min at 95 °C). The denaturated sample was loaded onto premade 4-15% Mini-PROTEAN-TGX gels (Biorad) and electrophoresis was performed (180 V, 35 min) in Running Buffer.

The separated proteins were detected by InstantBlueTM staining (see 6.18) or immunoblotting (see 6.19)

6.18 InstantBlueTM staining

For InstantBlueTM staining an SDS-Page (see 6.17) was subjected to InstantBlueTM staining solution (Expedeon) and incubated at RT for 1 h or at 4 °C for 16 h under constant agitation followed by a 1 h incubation with ddH₂O. The InstantBlueTM stain selectively stains proteins which results in a macroscopically visible blue signal for all stained proteins in the gel.

The stained gel was scanned using the Odyssey CLxTM system (LI-COR).

6.19 Immunoblotting

Proteins separated by SDS-PAGE (see 6.17) were transferred onto a nitrocellulose membrane by semi-dry Western-blotting in Blotting Buffer. For this the standard program (25 V, 1.0 A, 30 min) of the TransBlot™ Turbo™ System (BioRad) was utilized for all immunoblots.

All subsequent incubation steps were performed under constant agitation and at RT unless otherwise specified. Initially, the membrane was incubated in Blocking Buffer for 15 min in order to block unspecific binding sites, then for 1 h or overnight at 4 °C in the primary anti-MBP monoclonal antibody (NEB) solution (1:30,000 in Blocking Buffer).

The membrane was washed (5 x, 5 min, 5 ml Tris-buffered saline with Tween20 (TBS-T)) and incubated for 1 h in the secondary anti-mouse antibody (LI-COR) solution (1:15,000 in Blocking Buffer). The washing step was repeated.

The immobilized proteins were detected by near-infrared fluorescence using the LI-COR Odyssey CLx™ imaging system and protein signals quantified by the software ImageStudio™ lite (LI-COR).

6.20 Tobacco Etch virus protease cleavage

To analyze the orientation of PERK-TMR constructs in proteoliposomes, proteoliposomes were treated with TEV. The TEV cleavage site between the MBP-tag and the PERK-TMR domain is only accessible for the protease if this part of the PERK-TMR construct is outside the lumen of the proteoliposomes. 3.75 µl of freshly prepared TEV Buffer (10 µl Reconstitution Buffer with 20 mM Dithiothreitol (DTT), 9 µl Reconstitution Buffer, 1 µl TEV (10 mg/ml)) was mixed with 30 µl of proteoliposomes (equals one reconstitution approach from 6.15). The mixture was incubated at 30 °C and samples (10 µl) for an immunoblot were taken after 1 h and after 2 h.

6.21 Sucrose density gradient centrifugation of proteoliposomes

A sucrose density gradient can separate proteoliposomes from protein aggregates, provide information about the density of proteoliposomes and the success of reconstitution. For this, a sucrose step gradient with final sucrose concentrations of 40% (w/v), 30% (w/v), 25% (w/v), 20% (w/v), 10% (w/v) and 0% (w/v) in Reconstitution Buffer was prepared.

All sucrose solutions were pre-cooled in an ice-bath. Proteoliposomes were resuspended in 100 µl Reconstitution Buffer and mixed with 200 µl of 60% (w/v) and 700 µl of 40% (w/v) sucrose solution. The resulting bottom fraction was overlaid with 2 ml of each sucrose solution in the order of decreasing sucrose-concentration. The resulting step gradient of sucrose was centrifuged (16 h, 100.000x g, 4 °C, without breaks and minimal acceleration) utilizing a SW 41 Ti swing out rotor. Fractions of 1 ml were collected from the top to the bottom. The most bottom fraction was vigorously resuspended to remove a possible protein pellet from the tube wall and filled up ad 1 ml with Reconstitution Buffer if necessary.

6.22 Estimating lipid content using Hoechst 33342 fluorescence

The fluorescence dye Hoechst 33342 (Cayman Chemicals) is environment-sensitive. Its fluorescence intensity is vastly enhanced in the presence of hydrophobic environments like membranes

(Jumpertz et al. 2011). Thus it is possible to estimate the relative lipid content of different samples semi-quantitatively. Hoechst 33342 is light sensitive. All steps were carried out under avoidance of direct light.

To determine the relative lipid contents of different fractions of a sucrose gradient (see 6.21), 135 μ l of each 1 ml fraction of the sucrose step gradient were mixed with 15 μ l 70 μ M Hoechst 33342 in a black 96-well plate. The intensity of fluorescence in the individual samples were determined by a TECANTM reader using an excitation at 355 nm and an emission wavelength at 459 nm with a bandwidth of 20 nm. The fluorescence values were baseline corrected using the fluorescence values of an empty sucrose step gradient.

6.23 Sodium carbonate extraction from proteoliposomes

A membrane extraction assay was conducted to investigate the integration of PERK-TMR protein in liposome membranes.

Proteoliposomes (from 6.15) were resuspended in 1 ml of Reconstitution Buffer. The resulting sample was divided into equal parts of 200 μ l. Each sample was mixed with 300 μ l of Reconstitution Buffer, containing additionally **I**) 0.2 M Na₂CO₃ **II**) 2% (volume per volume (v/v)) Triton X-100 **III**) 8 M Urea or **IV**) no additives. The samples were incubated on a rotator for 30 min at RT after which sample **I**) was neutralized by addition of two-fold volume of Neutralization Buffer, whereas sample **II**) **III**) and **IV**) were diluted with a two-fold volume of Reconstitution Buffer. 200 μ l of each resulting sample were taken and mixed with 800 μ l of low salt buffer and transferred to a 1 ml centrifugation tube. Because possible pellets would be macroscopically invisible, the outwards facing edges of the centrifugation tube were marked prior to centrifugation (575,000x g, 16 h, 4 °C).

The supernatant and potential pellets were carefully separated by pipetting and further characterized by an immunoblot (6.19).

7 Results

7.1 Bioinformatic analysis of the predicted PERK-TMR

TOPCON (Bernsel et al. 2009) and TMHMM (Sonnhammer, von Heijne, Krogh 1998; Krogh et al. 2001) analysis was used to predict the TMR region of PERK. There is only one transmembrane helix (TMH) in the full-length PERK protein. A Heliquet analysis (Gautier et al. 2008) was performed on the TMR (aa 512-551; see Figure 6 **A**) of PERK and identified analytical amphipathic helix (AH) adjacent to the TMH. The analysis revealed a possible, juxta membrane AH N-terminally of the TMH (see Figure 6 **B**). The AH has a predicted hydrophobicity $\langle H \rangle$ of 0.709 and a hydrophobic moment $\langle \mu H \rangle$ of 0.460. The TMH has a predicted hydrophobicity $\langle H \rangle$ of 1.084 and a hydrophobic moment $\langle \mu H \rangle$ of 0.227. When ignoring the amino acid residues that contribute to either the TMH or the AH (see Figure 6 **A**) it is notable that the PERK TMH with 11 amino acids is relatively short when compared to the TMH of other proteins (Sharpe, Stevens, Munro 2010). This overall transmembrane organization resembles the transmembrane region of Ire1 from *S. cerevisiae*, which has been firmly implicated in sensing lipid bilayer stress (Halbleib et al. 2017).

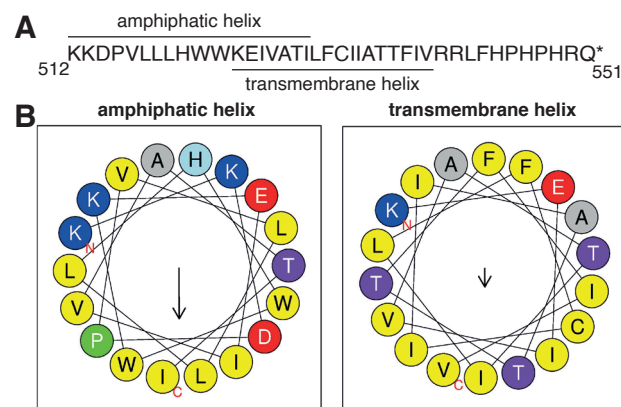


Figure 6: Bioinformatical analysis of the human PERK-TMR.

(A) The amino acid sequence of the human PERK-TMR (512-551) with predicted TMH and AH.

(B) Heliquet (Gautier et al. 2008) analysis of the predicted TMH and AH of human PERK-TMR.

7.1.1 Evolutionary conservation of the predicted PERK-TMR

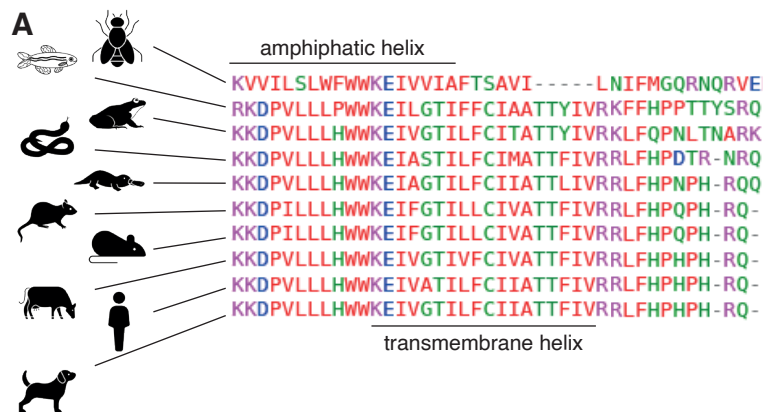


Figure 7: The sequence of PERK-TMR is highly conserved in varying animals.

(A) The sequence of PERK-TMR of different animals derived from the National Center for Biotechnology Information (NCBI Resource Coordinators 2018) and processed by Clustal Omega (Sievers et al. 2011). The animals from top to bottom are: [Name (Latin name, NCBI-sequence ID)], fruit fly (*Drosophila melanogaster*, Q9NIV1.2), zebrafish (*Danio rerio*, XP_{005156642.2}), western clawed frog (*Xenopus tropicalis*, XP_{031751153.1}), king cobra (*Ophiophagus hannah*, ETE71524.1), platypus (*Ornithorhynchus anatinus*, XP_{028902324.1}), brown rat (*Rattus norvegicus*, XP_{008761199.1}), house mouse (*Mus musculus*, AAH54809.1), cattle (*Bos taurus*, AAI40472.1), Human (*Homo sapiens*, AAI26357.1), domesticated dog (*Canis lupus familiaris*, XP_{854775.1}). The topical classification of transmembrane and amphipathic helix pertain the human PERK-TMR.

The predicted PERK-TMR from different species was aligned and compared to examine regions of high sequence conservation. Sequence information was retrieved from the National Center for Biotechnology Information database (NCBI Resource Coordinators 2018). The sequences were compared utilizing Clustal Omega (Sievers et al. 2011). The PERK-TMR is highly conserved in various animals (see Figure 7). Notably: Not only the PERK-TMR is highly conserved, there are several different regions of high conservation.

7.2 Preparation of PERK-TMR protein

7.2.1 Heterologous production, purification and labeling of the PERK-TMR in *E. coli*

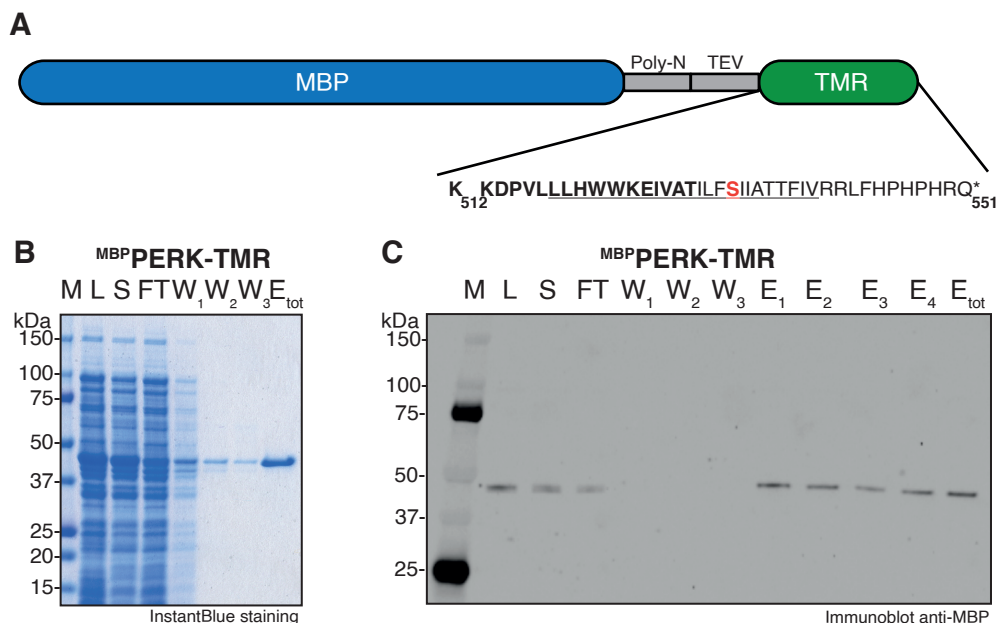


Figure 8: Purification of the PERK-TMR minimal sensor construct.

(A) Schematic illustration of the minimal sensor construct. The construct encompassed an N-terminal Maltose-binding-protein (MBP; blue) as solubility and purification-tag, a flexible poly-N linker (gray), a TEV (Tobacco Etch Virus) cleavage site (gray) and at the C-terminus the extended TMH region of PERK (green), containing the predicted TMH and juxtamembrane residues (residues 512 to 551 of the native protein). The native cysteine (residue 532; red) was mutated to serin to yield a cysteine-less construct. All residues mutated to cysteine for labeling and a subsequent structural characterization via EPR spectroscopy are indicated in bold. **(B)** Affinity purification of PERK-TMR from *E. coli*. Purification was monitored by subjecting 0.1 OD equivalents of total cell lysate (L), the soluble fraction (S), the flow through (FT) from the affinity purification, as well as individual wash fractions (W_{1-3}), and the pooled eluate (E_{tot}) from a SDS-PAGE followed by InstantBlueTM staining. **(C)** Diluted fractions from the affinity purification were analyzed by immunoblotting. MBP-positive proteins were detected using specific anti-MBP antibodies.

The construct contains an MBP-tag, a poly-N linker, a TEV cleavage site and a minimal PERK-TMR region. To characterize the PERK-TMR using EPR, a cysteine-less minimal PERK-TMR construct was generated and produced in *E. coli*. The native cysteine (residue 532) was substituted with a serine. The MBP-tag of the construct assured an economical purification from *E. coli* lysate (for a graphical representation of the construct see Figure 8 A).

The signal of the PERK-TMR construct runs on the SDS-PAGE at 42 kDa. The fraction containing PERK-TMR was already to guess in the signal-enrichment of the cell lysate at 42 kDa in the InstantBlueTM staining. Through affinity purification and several washing steps, it was possible to remove other proteins, so that a single protein signal remained in the final pooled eluate. During the three consecutive washing steps the signal intensity at 42 kDa decreased around 25% per washing step (see Figure 8 B).

To confirm that the protein signal in the InstantBlueTM SDS-PAGE was indeed the MBP-tagged PERK-TMR construct, an anti-MBP immunoblot was done (see Figure 8 C). A clear MBP-

positive signal can be seen at 42 kDa which indicates that the purified protein is indeed the protein of interest. The signal in the FT-band shows a loss of unbound protein - indicating either that the incubation step was too short and the protein was not able to fully bind to the amylose resin or that the quantity of amylose resin was insufficient. No signal can be seen on the W1-W3 washing-step-bands which indicates that no protein of interest is lost during the washing steps. The loss of signal at 42 kDa in the InstantBlue™ staining appears to be due to the removal of other proteins.

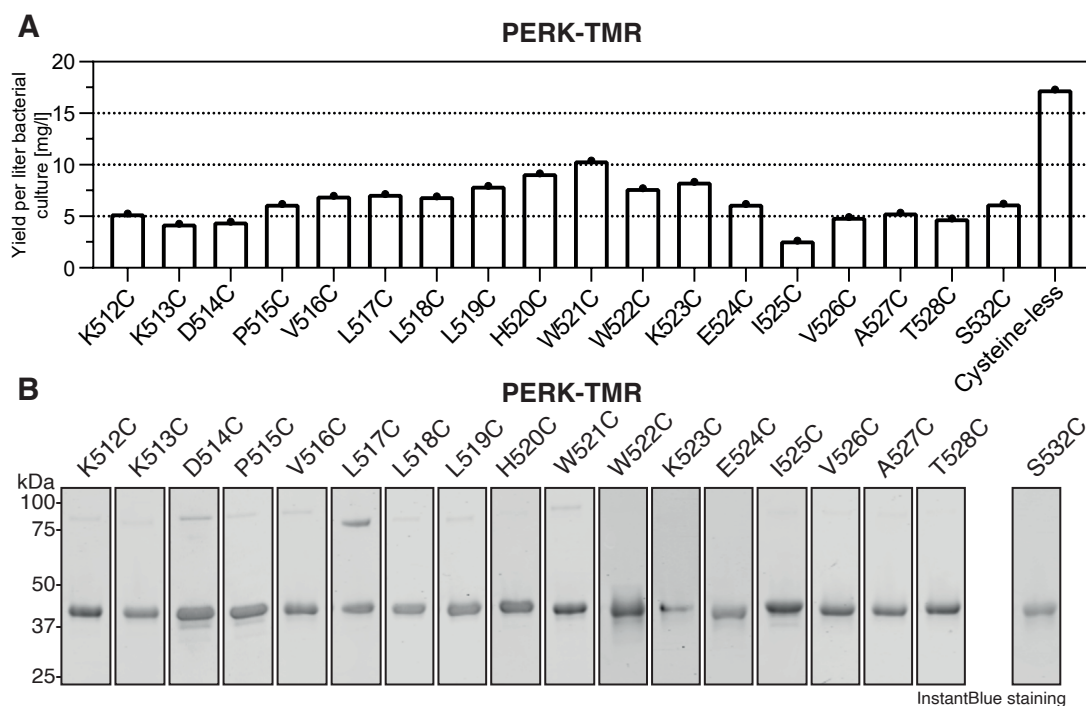


Figure 9: Isolation of single-cysteine variants of PERK-TMR.

(A) The total yield of purification from a 1 l bacterial culture for the indicated variants of PERK-TMR (Notable differences in the protocol of presented data: D514C: sub optimal sonification of bacterial pellet; V516C: "Codon+" instead of "Plys" *E. coli*; I525C and T528C: Overnight leakage during labeling step). **(B)** The indicated 19 PERK-TMR proteins were labeled with MTS, isolated by affinity purification and subjected to an SDS-PAGE. 1 μ g protein was loaded per lane and the gel was stained with InstantBlue™.

To examine the PERK-TMR and get structural and functional data of the interaction between protein and lipid bilayer we used EPR spectroscopy. EPR spectroscopy enables to gather data on the micro-environmental properties which directly surround an EPR spin probe (properties e.g. polarity or spin probe mobility) while having a high resolution of 1-2 nm. It can answer for example if a certain residue of the protein TMH is inside or outside of the lipid bilayer - seen by a change of the environmental polarity.

EPR needs a spin-label containing a free electron radical. We used the MTS-label, which is small and unpolar - thus non-disturbing to the lipid bilayer or the protein-structure - and binds reliably to cysteine residues by disulfide bonds. To get reliable data on different positions of the protein helix it is required to introduce single cysteine mutants to an otherwise cysteineless protein.

Single cysteine variants of PERK-TMR were labeled on the amylose resin column during affinity purification. The 18 different variants of PERK-TMR show a yield between 2.4 - 17.2 mg/ml per 1 l bacterial culture which is sufficient for further experiments in all cases. The variants also show different quantities of byproduct in the final product (see Figure 9 B). This byproduct runs at

around 80 kDa and is MBP-positive. It most likely represents PERK-TMR disulfide-bridged dimers. Because dimers already formed disulfide bonds between each other they can not be labeled with MTS-label, thus they do not interfere with the EPR signal. L517C shows the biggest fraction of dimers followed by variant D514C. The variants D514C, P515C and I525C show a second byproduct running at 37 kDa, the origins of which are unknown. Because the second byproduct is also MBP-positive we suspect that it is the MBP-tag or not fully produced PERK-TMR construct.

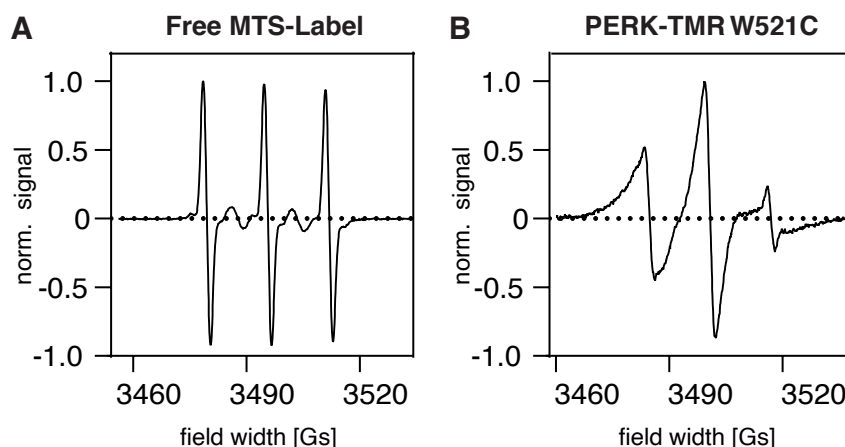


Figure 10: EPR spectroscopy reveals free MTS labels in preparations of PERK-TMR.

(A) A cwEPR spectrum of the free MTS-label (1 nmol in wash buffer) was recorded at RT (20-26°C) as a reference. **(B)** Exemplarily shown is the cwEPR spectrum recorded for the labeled PERK-TMR_{W521C} (1.11 mg/ml in wash buffer_{Glyc}) construct. The spectra were baseline corrected and normalized relative to the highest value of the data set.

To test if the labeling was successful, a EPR spectrum was recorded from a protein sample.

Figure 10 **A** shows the unique EPR spectrum from the unbound MTS-label with its unique 3-peaked signature at 3480, 3495 and 3510 Gs.

Figure 10 **B** shows an EPR spectrum of the isolated and labeled PERK-TMR. The unique signal of the MTS-label changed. The 3 sharp spikes of the MTS-label widened and a connected wave form can be seen. This indicates that the spin label has become more immobile by having formed a disulfide bond with a cysteine residue of the PERK-TMR. This protein-label-complex is not as mobile as a free MTS-label itself, thus changing the EPR spectrum.

At 3515 Gs in Figure 10 **B** a sharp wave form can be seen, which corresponds with the third spike of the EPR spectrum from the free MTS-label. This indicates that the raw purification product still contains a substantial part of free spin-label.

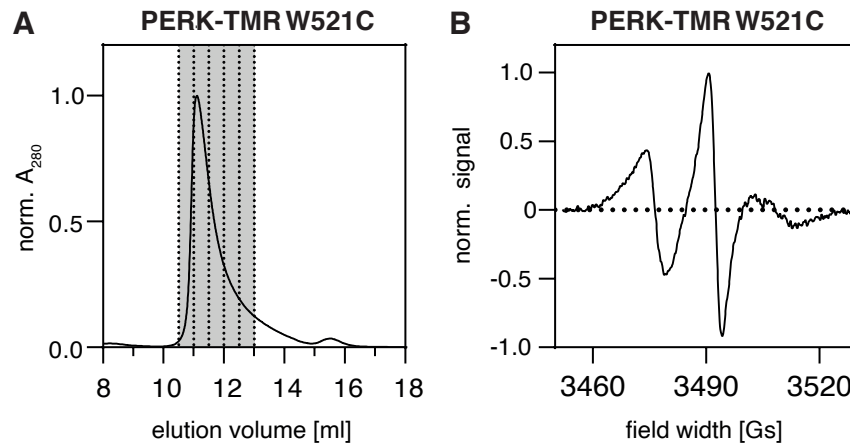


Figure 11: Size-exclusion chromatography indicates a monodisperse preparation of MTS-labeled PERK-TMR constructs and removes free MTS labels.

(A) The affinity purified and labeled PERK-TMR_{W521} protein was concentrated to a final volume of 0.1 ml and loaded onto a Superdex 200 10/300 Increase column (void volume 8.8 ml, flow rate 0.5 ml/min, SEC Buffer). The gray shaded fractions were pooled for further experiments. **(B)** A cwEPR spectrum of PERK-TMR_{W521} (0.57 mg/ml in wash buffer_{Glyc}) purified by size exclusion chromatography was recorded at RT. cwEPR measurements were recorded at RT (20-26 °C), baseline corrected, and normalized relative to the highest value of the data set.

Free MTS-label increases the noise of the EPR signal and hinders a straightforward interpretation of the spectrum. Because of this, the protein was further purified by SEC. SEC helped to remove the free spin-label from the sample (see Figure 12) and standardized the buffer environment of the PERK-TMR constructs. The peak caused by the free MTS-label at 3515 Gs is no longer visible (see Figure 12 B).

7.2.2 Determining the spin labeling efficiency of PERK-TMR variants

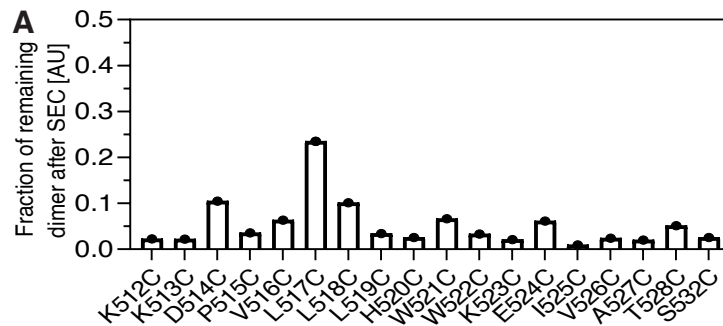


Figure 12: Dimers of PERK-TMR protein remain in the final preparation after SEC.

(A) Quantification of dimers in the final protein preparation. Anti-MBP immunoblots of the SEC derived fractions were quantified. The signal of the dimer signal was normalized to the overall signal of each lane.

Even with the additional SEC purification step, a substantial part of the final protein samples is constituted by protein dimers (see Figure 12 **A**). The highest fraction of protein dimers was seen in variant L517C, accounting for 26% of the whole protein signal. These dimers are highly imperious against reducing agents. They can be attributed to disulfide bonds between two PERK-TMR proteins. Because the MTS-label labels free cysteines, dimers consist of unlabeled protein and therefore do not contribute to the EPR signal. Even though the presence of PERK-TMR dimers in the preparation may have had an impact on the physicochemical bilayer properties and inter-variant-comparability, it was decided to analyze all samples without any further sample purification. In particular the results related to D514C, L517C and L518C should be interpreted with care.

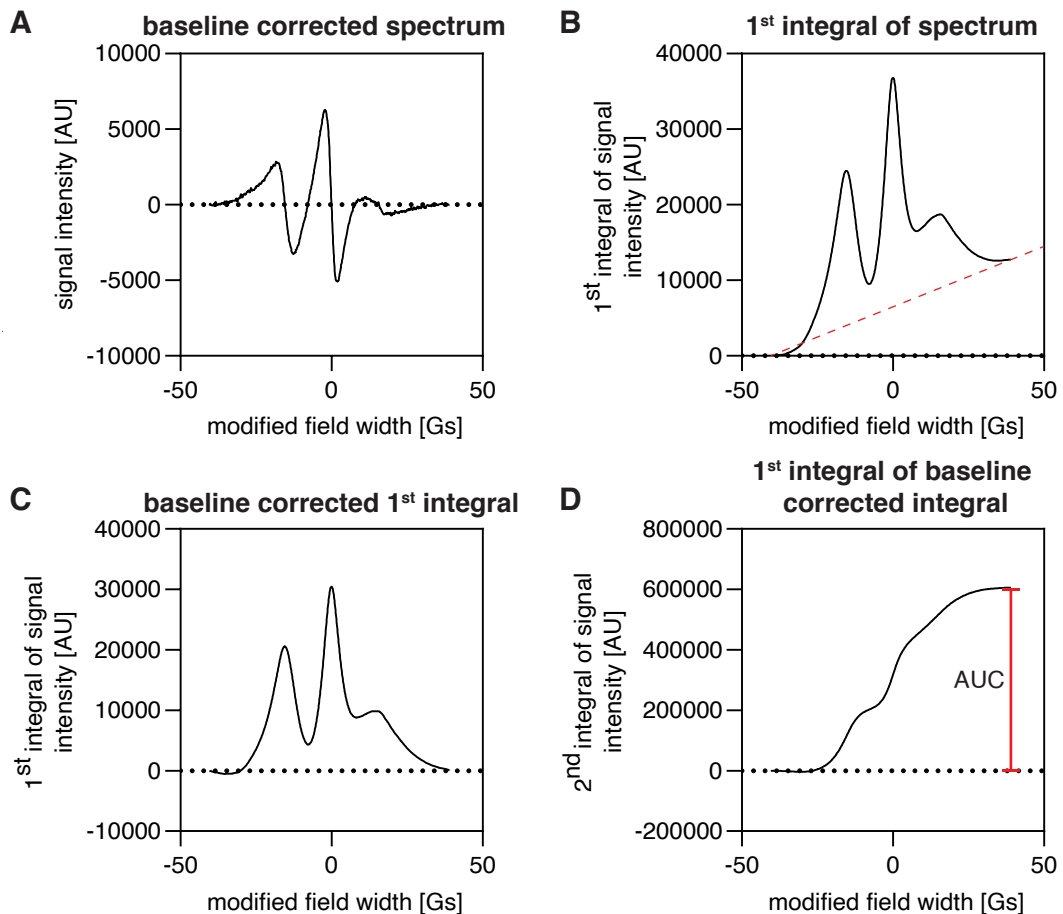


Figure 13: Walkthrough of the calculation of the labeling efficiency.

(A) Baseline corrected spectrum recorded at RT (21-26 °C). The EPR spectrum itself is the 1st derivate of the absorption spectrum. (B) The 1st integral of the spectrum from A. We subtracted a linear baseline, so that the integral starts and ends at y=0. (C) The baseline corrected integral is the absorption spectrum as measured by cwEPR. (D) The integral of the absorption spectrum. Here the area under the curve (AUC) of (C) can be determined, which is a measure of the total spin signal intensity.

The labeling efficiency of PERK-TMR protein was determined by EPR measurements of solubilized protein at a known concentration. The EPR spectrum was baseline corrected and a first integral was calculated. This first integral was baseline corrected. The area under the curve was determined by the first integral of the baseline corrected first integral (see Figure 13). The area under the curve is a measure of the total spin signal intensity of the sample. The total spin signal intensity of the protein sample was compared to a 1 nmol MTS sample. Labeling efficiencies of e.g. over 100% can be explained by cumulative pipetting error. The variant L517C shows the lowest labeling efficiency of 63% which can be partially explained by the high fraction of disulfide linked PERK-TMR proteins (see Figure 12 A). Most variants show a labeling efficiency of >75% (see Figure 14 A).

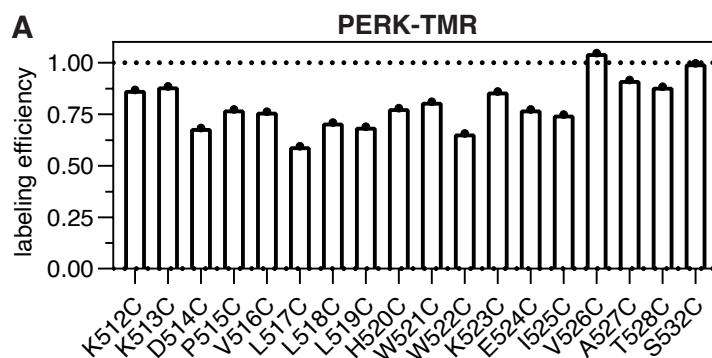


Figure 14: MTS labeling efficiency of single-cysteine variants of PERK-TMR.

(A) cwEPR spectra of indicated variants of SEC-purified PERK-TMR protein (0.5-1.2 nmol) were recorded in wash buffer_{Glyc} and baseline corrected. The samples were recorded at RT and the total spin signal intensity was determined as outlined in figure 13. The experimentally determined signal was used to simulate a spectrum at a concentration of 1 nmol. The total spin signal intensity of this simulated spectra were normalized to the total spin signal intensity of a solution containing 1 nmol MTS label.

7.3 Optimization of the reconstitution of PERK-TMR protein in liposomes

To establish a reliable reconstitution approach of the PERK-TMR with a lipid bilayer, all 18 PERK-TMR variants were reconstituted in liposomes composed only of phosphatidylcholin lipids and an acyl chain composition with 50% saturated and 50% unsaturated acyl chains (POPC). The POPC environment shows a higher degree of lipid saturation than is normally observed in the membrane- and presumably the ER-membrane- of unstressed cells, where >75% unsaturated lipid acyl chains are found in membrane glycerophospholipids (Pineau et al. 2009).

The POPC-only environment was chosen because POPC is one of the most abundant lipids in biological membranes (van Meer, Voelker, Feigenson 2008) and to minimize lipid complexity with its unified lipid headgroup matrix. It is used as the default lipid environment for in vitro experiments regarding the eukaryotic membrane. Its low lipid packing density presumably eases the reconstitution of TMH proteins.

When creating proteoliposomes by reconstitution, different pitfalls have to be considered: 1. a loss of protein during reconstitution which can lead to a loss of enough spin-label that an EPR measurement is no longer feasible, 2. the monitoring of protein aggregation during reconstitution and 3. the forming of an inhomogenous distribution of protein among different populations of proteoliposomes. The latter two can lead to significant changes in the EPR spectra, causing misleading data-points.

The loss of protein during reconstitution is mainly an economic concern and most relevant after an optimized protocol has been found, which sufficiently evades pitfall 2 and 3 (See Chapter 7.4.1). To get an indication of both protein aggregation, as well as proteoliposome-distribution, sucrose gradients were used.

A sucrose gradient separates material by density. Proteoliposomes with a low protein to lipid ratio float higher than proteoliposomes with a high protein content. Protein-aggregates pellet on the bottom of the sucrose gradient. The distribution of proteins can be monitored by an immunoblot of the sucrose fraction. The distribution of lipids in the sucrose gradient can be estimated by a Hoechst 33342 assay. A comparable distribution of lipid and protein in one sample and

a low ratio of protein aggregates indicate a successful reconstitution. For a schematic illustration of the used sucrose gradient see Figure 15 A.

7.3.1 Comparing the reconstitution of the cysteine-less PERK-TMR to the native cysteine-containing PERK-TMR

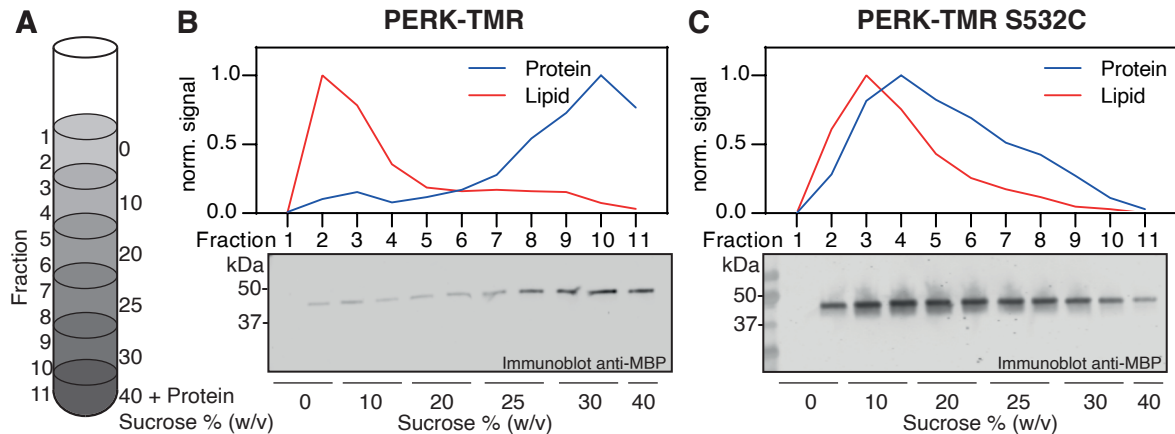


Figure 15: The cysteine-less PERK-TMR is prone for aggregation during reconstitution in liposomes.

(A) Schematic illustration of the sucrose gradient used for validating the reconstitution of PERK-TMR in liposomes. A proteoliposomal preparation was adjusted to a final concentration of sucrose of 40% w/v and overlaid with indicated sucrose solutions of decreasing density in a centrifugation tube. The sample was centrifuged (16h; 4°C; 100,000 g; slowest acceleration and no breaks). While proteoliposomes are expected to float during centrifugation due to their buoyant density, protein aggregates are expected to remain in the bottom fraction(s) of the gradient. 1 ml fractions were removed from the gradient after centrifugation (from top to bottom) and further analyzed for their relative lipid and protein content. **(B)** Quality control of proteoliposomes containing reconstituted PERK-TMR and **(C)** Reconstituted PERK-TMR_{S532C}. **(B, C)** Both proteins were reconstituted in liposomes at a desired protein to lipid ratio of 1:500 in a 100% POPC environment. Fraction samples from **A** were analyzed by an immunoblot using anti-MBP antibodies to get an indication of the dispersion of protein in the sucrose gradient. Further fraction samples were analysed using an Hoechst 33342 assay to get an rough indication of lipid distribution in the sucrose gradient. The signals were normalized, relative to the highest intensity in each data set.

To examine the potential differences in reconstitution of the endogenous cysteine-containing PERK-TMR variant (PERK-TMR_{S532C}) and the cysteine-less PERK-TMR (PERK-TMR) construct, both variants were reconstituted with a P:L of 1:500 in a 100% POPC environment.

In the case of the cysteine-less construct, the signals for lipid and protein are distributed vastly different among the fractions of the sucrose density gradient (see Figure 15 B). This indicates an inhomogenous distribution of the cysteine-less construct, which suggests different populations of proteoliposomes with higher and lower protein-to-lipid ratio, respectively. Furthermore, a substantial amount of the cysteine-less construct was detected in the lipid-free bottom fractions of the gradient, suggesting a significant degree of protein aggregation during or after the reconstitution procedure.

In contrast to that, the PERK-TMR_{S532C} construct reconstituted sufficiently, as indicated by

the much higher correlation of protein and lipid signals in the fractions of the sucrose gradient and the negligible protein content in the most bottom fraction of the sucrose gradient (see Figure 15 **C**).

This indicates that the cysteine-less construct cannot be reconstituted with the same efficiency as the wild type (WT) counterpart potentially due to the more polar serine residue at the position of the native cysteine 532. This was a particularly important as well as surprising observation, because all single-cysteine variants are based on the cysteine-less construct and may cause similar technical challenges for a successful reconstitution.

Because the successful reconstitution of cysteine-less constructs and its derivatives is important for further experiments, we optimized the reconstitution protocol by changing the different variables in the reconstitution mixture: the lipid environment and the protein to lipid ratio (P:L).

7.3.2 The effect of different lipid environments on the reconstitution of PERK-TMR

In the search for an optimized reconstitution protocol for the cysteine-less PERK-TMR constructs, different lipid environments were used. The lipid environment consisting of 50 mol% of each POPC and DOPC mimics the acyl chain composition of the unstressed ER. Thus it may represent a more suitable environment for the PERK-TMR.

The 100 mol% POPC environment is used as a reference point from earlier experiments. It has a slightly higher lipid packing density than the POPC DOPC environment.

The 80 mol% POPC and 20 mol% cholesterol containing environment represents the stressed ER. It shows the highest lipid packing density of the examined lipid environments. The ability of the PERK-TMR to sense lipid bilayer stress (Volmer, Ploeg, Ron 2013; Radanović, Ernst 2021) may make the PERK-TMR particularly sensitive to abnormally increased levels of lipid saturation, thus the reconstitution of the PERK-TMR should be even more problematic.

The cysteine-less PERK-TMR was reconstituted in all three lipid environments and the resulting proteoliposomes were examined by a sucrose gradient.

The lipid packing density (LPD) and lipid environment have an impact on the success of reconstitution of cysteine-less PERK-TMR (see Figure 16). With the decrease of lipid packing density (see Figure 25) of the lipid environment, the reconstitution success increases.

A higher LPD leads to an increase of protein aggregates as well as a dis-unification of the protein peak. Although the DOPC POPC environment has the most promising reconstitution success, POPC was used as default lipid environment in all further experiments, because it is the most simple lipid environment. Still: The reconstitution of the cysteine-less PERK-TMR at a protein to lipid ratio of 1:500 is insufficient for all tested lipid environments.

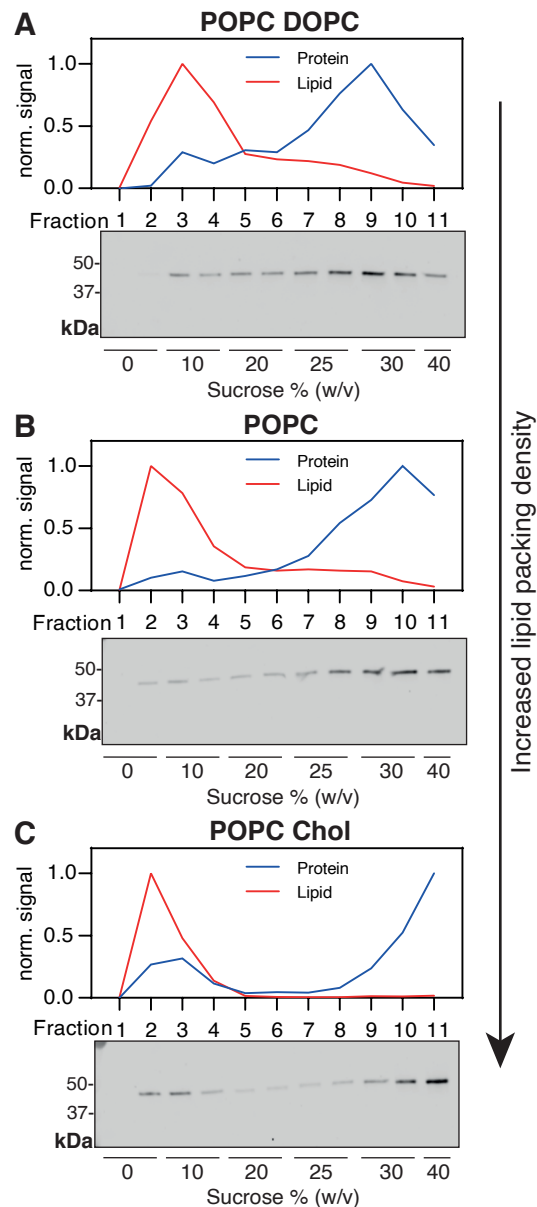


Figure 16: Lipid environment and lipid package density have a big impact on the success of reconstitution of cysteine-less PERK-TMR.

(A-C) Cysteine-less PERK-TMR proteins were reconstituted at a desired protein to lipid ratio of 1:500 in according lipid environments. Lipid environments differ in composition and lipid packaging density. Fraction samples from a sucrose gradient were analyzed by an immunoblot using anti-MBP antibodies to get an indication of the dispersion of protein in the sucrose gradient. Further fraction samples were analyzed using an Hoechst 33342 assay to get an rough indication of lipid distribution in the sucrose gradient. The signals were normalized, relative to the highest intensity in each data set. (A) Quality control of proteoliposomes reconstituted in DOPC POPC. (B) Quality control of proteoliposomes reconstituted in POPC. (C) Quality control of proteoliposomes reconstituted in POPC Chol.

7.3.3 The effect of different protein to lipid ratios on the reconstitution of PERK-TMR

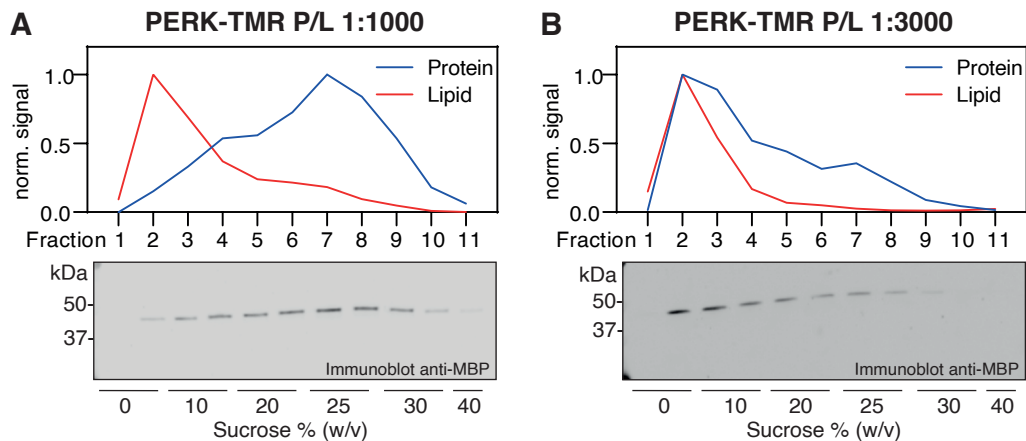


Figure 17: Lowering the ratio of protein to lipid improves the reconstitution of PERK-TMR in liposomes.

(A, B) Proteins were reconstituted in an 100% POPC containing liposomes. The preparation was subjected to a sucrose gradient. An anti-MBP immunoblot was used to determine the protein distribution. A Hoechst 33342 assay was conducted to get an indication of the lipid distribution of the sucrose gradient. The signal was normalized to the maximum intensity of each respective data set. **(A)** Reconstituted PERK-TMR with a protein to lipid ratio of 1:1000. **(B)** Reconstituted PERK-TMR with a protein to lipid ratio of 1:3000.

To examine the effect of lower P:L on the reconstitution success, cysteine-less PERK-TMR was reconstituted at a P:L of 1:1000 and 1:3000 in a 100% POPC environment.

A lower P:L ratio leads to an increased association of protein and lipid signals as well as a decrease of protein aggregates in the sucrose gradient (see Figure 17).

These experiments revealed that it is possible to successfully reconstitute cysteine-less PERK-TMR at a low protein-to-lipid ratio (1:3000, see Figure 17 **B**) and when the fatty acyl chain composition mimics the loosely packed composition of the ER. Notably, a protein-to-lipid ratio of 1:3000 is still suitable for EPR experiments as planned.

However, the presented data indicates that the reconstitution of PERK-TMR is technically challenging and that already a protein-to-lipid ratio of 1:1000 causes substantial inhomogeneities in the reconstitution process as indicated by a distinct distribution of lipids and proteins in the sucrose density gradient (see Figure 17 **A**).

7.4 Quality control of the reconstitution of PERK-TMR in liposomes

7.4.1 Loss of protein during the reconstitution of cysteineless PERK-TMR

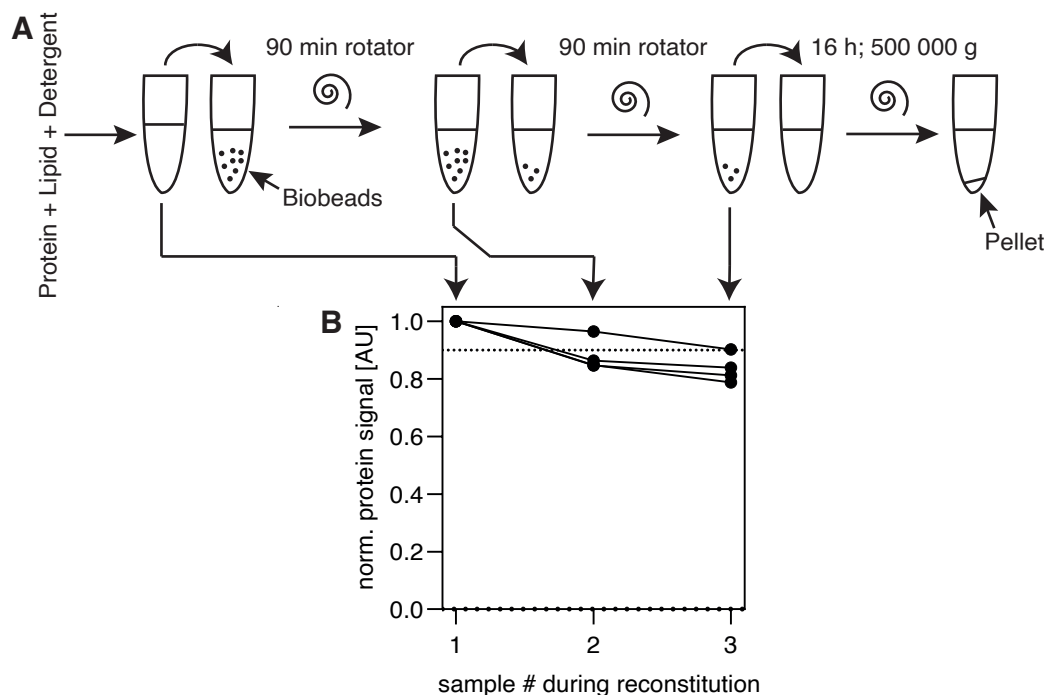


Figure 18: The loss of protein during reconstitution is negligible.

(A) Illustration of the reconstitution process and the points where samples were taken to monitor the loss of protein during reconstitution. Samples were taken from 4 independent PERK-TMR reconstitutions in a 100% POPC environment with a protein to lipid ratio of 1:3000. **(B)** Samples derived from **A** were subjected to an SDS-PAGE and further analyzed using an anti-MBP immunoblot. The protein signal was normalized to the signal intensity of the input sample.

The reconstitution of the cysteine-less PERK-TMR in liposomes is challenging. Only a decrease of the P:L ratio and a suitable lipid environment make a successful reconstitution possible. A low P:L ratio directly leads to less available protein and - directly corresponding - less EPR-spin signal.

To examine if a substantial part of the protein is lost during reconstitution, samples were taken at different stages in the reconstitution process (see Figure 18 **A**) and the overall protein content was measured using SDS-PAGE analysis and densitometric determination of the protein signal.

During reconstitution the overall protein content in the sample decreases only slightly. More than 80% of the starting protein remains after reconstitution (see Figure 18 **B**). This small decrease in protein content is negligible for the EPR measurements.

The decrease in protein can occur because protein binds to the BioBeads™, or because of an diluting effect of the BioBeads™. The BioBeads™ are soaked in Reconstitution Buffer before

being subjected to the sample mixture. This extra buffer inside the BioBeads™ can lead to an overall dilution of the sample and thus to the impression of a decreased protein content in the sample.

The cysteine-less PERK-TMR can be successfully reconstituted at a P:L of 1:3000 in a 100% POPC environment without a substantial loss of protein.

7.4.2 Stability of insertion of reconstituted cysteine-less PERK-TMR in a POPC environment

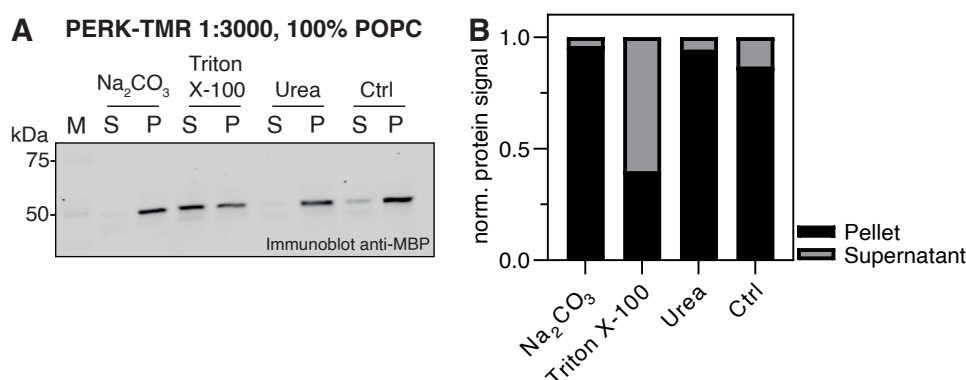


Figure 19: Cysteineless PERK-TMR protein integrates successfully into a 100% POPC membrane.

(A) Anti-MBP immunoblot of a membrane extraction assay. The assay was conducted with a cysteineless PERK-TMR protein reconstituted in a 100% POPC environment with a P:L of 1:3000. (B) Quantification of the immunoblot from A. Each dataset was normalized to the sum of respective supernatant and pellet fraction.

Although the sucrose gradient is a reliable and important quality control of the reconstitution, it can not differentiate between PERK-TMR which successfully inserted into the lipid bilayer and PERK-TMR which merely is attached to the outer surface of an liposome. To examine the success of the reconstitution further, an extended membrane extraction assay was carried out.

By subjecting proteoliposomes to a stark change of pH or to high levels of Urea, only peripherally attached trans-membrane proteins get removed from the liposome-surface. After centrifugation the proteoliposomes are pelleted whereas the solubilized proteins remain in the supernatant.

The membrane extraction assay with carbonate was carried out as extended assay (carbonate, detergent (Triton X-100), urea, control), and a light version (carbonate only). The full version of the membrane extraction assay was used as a proof of principle for the optimized reconstitution protocol with a cysteineless PERK-TMR.

In the extended assay, the cysteineless PERK-TMR shows a strong signal in all pellet fractions independent of solvent. The supernatant fraction of the Triton X-100 fraction also shows a strong protein signal (see Figure 19 A). Neither 0.2 M Na₂CO₃ nor 8 M Urea were able to remove

PERK-TMR from the proteoliposomes, indicating a stable insertion of the PERK-TMR.

Triton X-100 is a non-ionic detergent and solubilizes the lipid bilayer directly. It serves as positive control. Under optimal conditions, all protein will be solubilized by the Triton X-100 and no protein signal is detectable in the pellet fraction. In this case the content of Triton X-100 in the sample was not enough to solubilize all proteoliposomes, so that 40% of the protein signal remains in the pellet fraction (see Figure 19 **B**).

The light version of the assay was used for most of the proteoliposomes with a 100% POPC environment and a P:L of 1:3000 and reliably shows a stable insertion of the PERK-TMR protein of over 90%.

7.5 Processing and interpretation of EPR-spectra

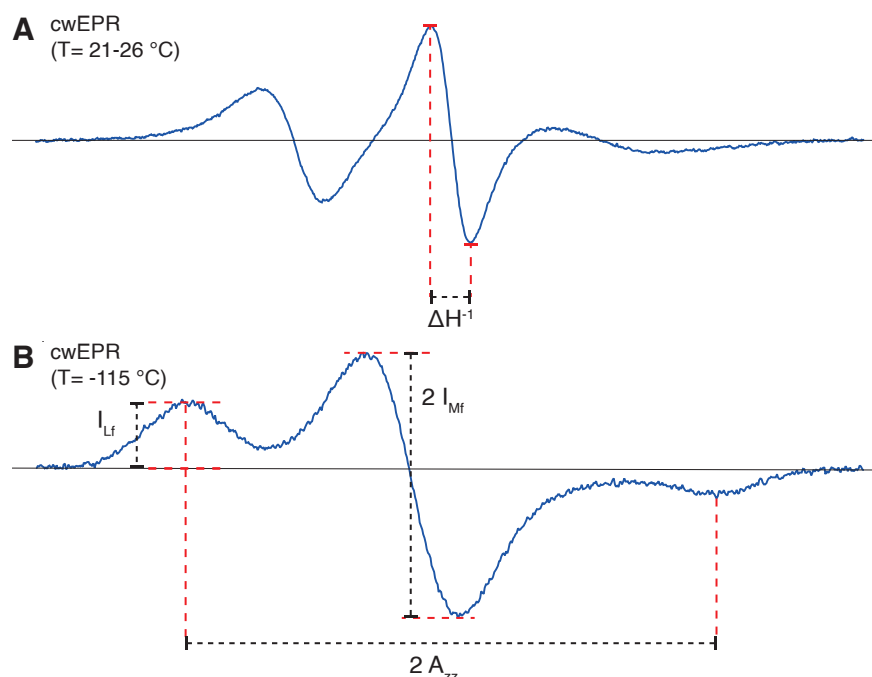


Figure 20: Illustration of spectra analysis on representative cwEPR spectra recorded at different temperatures.

(A) A cwEPR spectrum recorded at RT (21-26 °C) is shown to visualize the line width of the middle field peak (ΔH). The inversion of the middle field peak width (ΔH^{-1}) serves as a mobility parameter. A higher value of ΔH^{-1} , respectively a narrower middle field peak, indicates higher mobility of the spin probe. **(B)** A cwEPR spectrum was recorded at -115 °C. Derived from this spectra was the $2A_{zz}$ parameter (the differences of field strength of the low field maximum and the high field minimum value). The $2A_{zz}$ functions as a sign of micro-environmental polarity (a high $2A_{zz}$ indicates a high polarity). The intensity of low (I_{Lf}) and middle ($2I_{Mf}$) field peak serve as parts of the proximity index (I_{Lf}/I_{Mf}). Interspin distances between 1 and 2 nm lead to broadening of the spectrum and an increase of the proximity index.

Different parameters can be derived from the cwEPR spectra at different temperatures. In this study the micro-environmental polarity parameter " $2A_{zz}$ ", the proximity index " I_{Lf}/I_{Mf} ", and the

mobility parameter " ΔH^{-1} " were examined.

The $2A_{zz}$ parameter reports on the polarity in the nano-environment of the spin probe, which is affected by the position of the probe relative to the lipid bilayer and by neighboring residues in the PERK-TMR construct (Bordignon, Steinhoff 2007).

The I_{Lf}/I_{Mf} index indicates the distance between two MTS-labels around less than 6 nm (Jeschke 2012; Bordignon, Steinhoff 2007) and can be used to examine the state of dimerization in the sample (Covino et al. 2016).

The ΔH^{-1} parameter indicates the mobility of the spin probe and can suggest whether a part of the TMH is buried or otherwise restricted in its movement (high lipid-packing-density; high protein-to-lipid-ratio) and thus less mobile, or outside of the membrane and thus unhindered in its mobility (Ballweg et al. 2020).

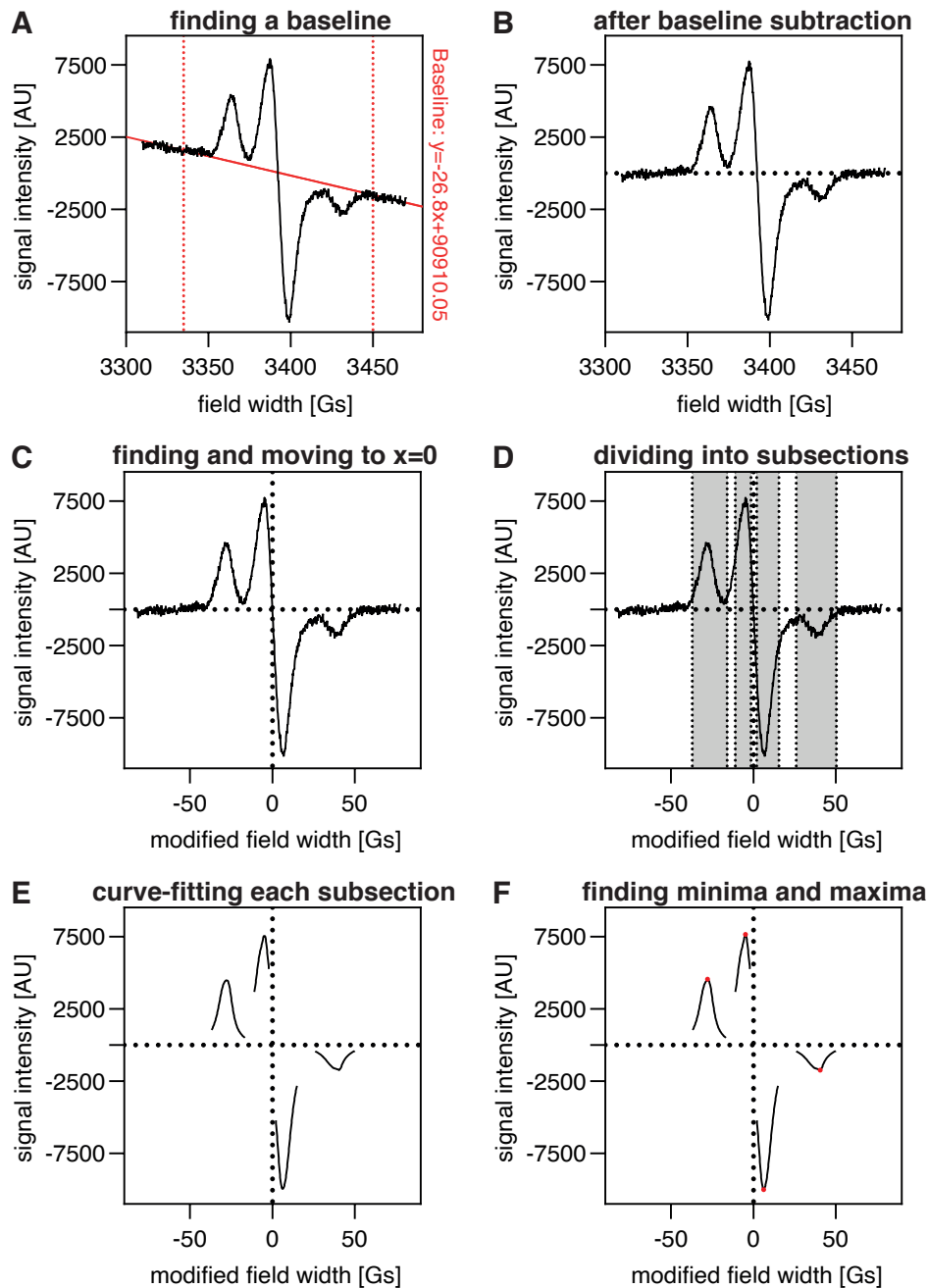


Figure 21: Establishing the pipeline for automatic processing of EPR-spectra.

(A) The baseline of the cwEPR spectrum (exemplarily shown is a spectrum recorded at $-115\text{ }^{\circ}\text{C}$) was defined by two hard-coded points at $x_{\text{beginning}}=3335\text{ Gs}$ and $x_{\text{end}}=3450\text{ Gs}$ (dotted red). x_1 and x_2 are the immediately following x values of $x_{\text{beginning}}$ or x_{end} , whereas y_1 and y_2 were calculated as the mean Y-value of the 10 consecutive value pairs following $x_{\text{beginning}}$ or x_{end} . The baseline (red) was calculated with the two known points (x_1/y_1) and (x_2/y_2) . (B) cwEPR spectrum after subtraction of the baseline. (C) After finding the point between the mid field peaks in which the cwEPR spectrum crosses $y=0$, the graph is moved, so that this point represents the new origin ($x=0, y=0$). (D) Four sections (grey) of the cwEPR spectrum get defined near hard coded x-values $(-37, -16; -11, -1.5; 2, 15.5; 26, 50.5)$. They represent the region where a maximum or minimum value is to be expected. (E) The sections of the cwEPR spectrum were fitted individually using the sum of two Lorentzian curves or a polynomial equation. (F) The point of a minimum or maximum value can be determined reliably.

In order to establish a procedure to extract the specific parameters (see 7.5) from an EPR spectrum, an automated routine was established using the scripting language "python" (for the source code see 9.1) in the course of this study. The individual steps performed by the python program are illustrated in Figure 21.

A cwEPR spectrum served as input data from which the spectrum of a buffer-only sample was subtracted (for both RT and LT cwEPR spectra), which was then converted in an ASCII-format by the program "Medeia". Then, a baseline was detected by linear fitting, using the average of 10 consecutive data points at both the beginning and the end of the spectrum. The baseline was subtracted from the EPR spectrum. The intersection of the x axis and the spectrum between the mid-field high and the mid-field low was defined as $X=0$. Now having uniform spectra, each spectrum was divided into subsections to isolate each peak. The isolated peaks were further curve fitted individually using the sum of two lorentzian curves or a polynomial equation. The X/Y-coordinates of the minima and maxima can be reliably determined from the fitted curve.

The plausible range of EPR parameter (see Figure 20) values is rather narrow. For example: The 2Azz-parameter has a variability of 6 Gs, deciding between an extremely polar or extremely non-polar nano-environment and is derived from a spectrum that ranges from 3335 to 3450 Gs (= 115 Gs) consisting of 1024 data-points. Because of this even a slight difference in the handling of the cwEPR spectra assessment by -for example- a biased evaluator skews the final evaluation of the spectrum.

A rather small measuring error has a high impact on the interpretation of the data. The program was established to guarantee a reproducible, unbiased, and precise evaluation of the cwEPR spectra, to standardize the analysis, and to make the analysis more time efficient.

It was coded to ease and standardize the evaluation process internally. Mathematical efficiency, elegance of the execution, and code readability ranked behind.

7.6 EPR spectra of the PERK-TMR

7.6.1 EPR-Spectra of spin-labeled PERK-TMR at room temperature

To examine the structural properties of the in a lipid membrane inserted PERK-TMR, we recorded cwEPR spectra of various PERK-TMR constructs. Each PERK-TMR construct contains a single position where the native amino acid was substituted by a MTS-labeled cysteine. Through this approach it is possible to get proximity, polarity, and mobility data of different positions of the inserted PERK-TMR. We chose a part of the N-terminal half of the inserted PERK-TMR.

Information about the mobility can be gathered by this approach through RT cwEPR spectra (see Figure 22). The mobility data can indicate locations of high friction inside the protein-lipid interface. If protein-protein or protein-lipid interactions occur, for example, during which the mobility of the protein gets stereochemically inhibited. This can happen at the location of the insertion - when the protein helix interacts with the rather dense and polar area of lipid headgroups. The contrary is also possible: The mobility parameter indicates areas of high mobility and unhindered movement of the MTS-label, for example in the middle of a lipid bilayer, where the non-polar fatty acid chains of both sides of the lipid bilayer end and form a kind of short atomical gap.

It was possible to record significant and meaningful RT cwEPR spectra of nearly all tested PERK-TMR constructs. Only of the E524C-PERK-TMR construct was it impossible to record an evaluateable cwEPR spectrum even after repeated reconstitution.

The evaluation of the RT cwEPR spectra indicates:

1. There is no apparent helical topic in the mobility of the amphipathic helix. If the amphipathic helix would insert into the membrane shallowly over its full length the residues one helical turn apart (513 and 516) would also insert into the membrane, showing a hindered movement. This indicates that the amphipathic helix arches over the membrane, but does not insert into the membrane in its entire length. The valin residue 516 is one of the most mobile residues, following the structural disruptor proline. To further investigate the insertion of the PERK-AH, quenching experiments could be promising.
2. The mean mobility of the PERK-TMR decreases throughout our dataset only to increase at the end of it. Or, speculatively, the part of the PERK-TMR helix which is inserted in the lipid bilayer is less mobile than the non-inserted part. The most deeply inserted part is then more mobile than the rest of the helix, speculatively being in the middle of the membrane ("near the "atomical gap").
3. The least mobile parts of the dataset are residues 520-521 and 525-527. 522 and 521 are both tryptophane residues which are known as membrane anchoring residues through their indole (Johnston et al. 2015), stabilizing their surroundings, and are often enriched in the lipid headgroup region of transmembrane proteins (Situ et al. 2018) where a high atomic density is present. We were not able to record an EPR spectra from residue E524C. This could speculatively derive from spin-spin interactions leading to a signal cancellation if two spin labels are near each other to a few nm. If this is the case, residue 524 marks the point where the homodimers are most near to each other, hindering the movement of following residues (525-527) by stereo-chemical interactions.

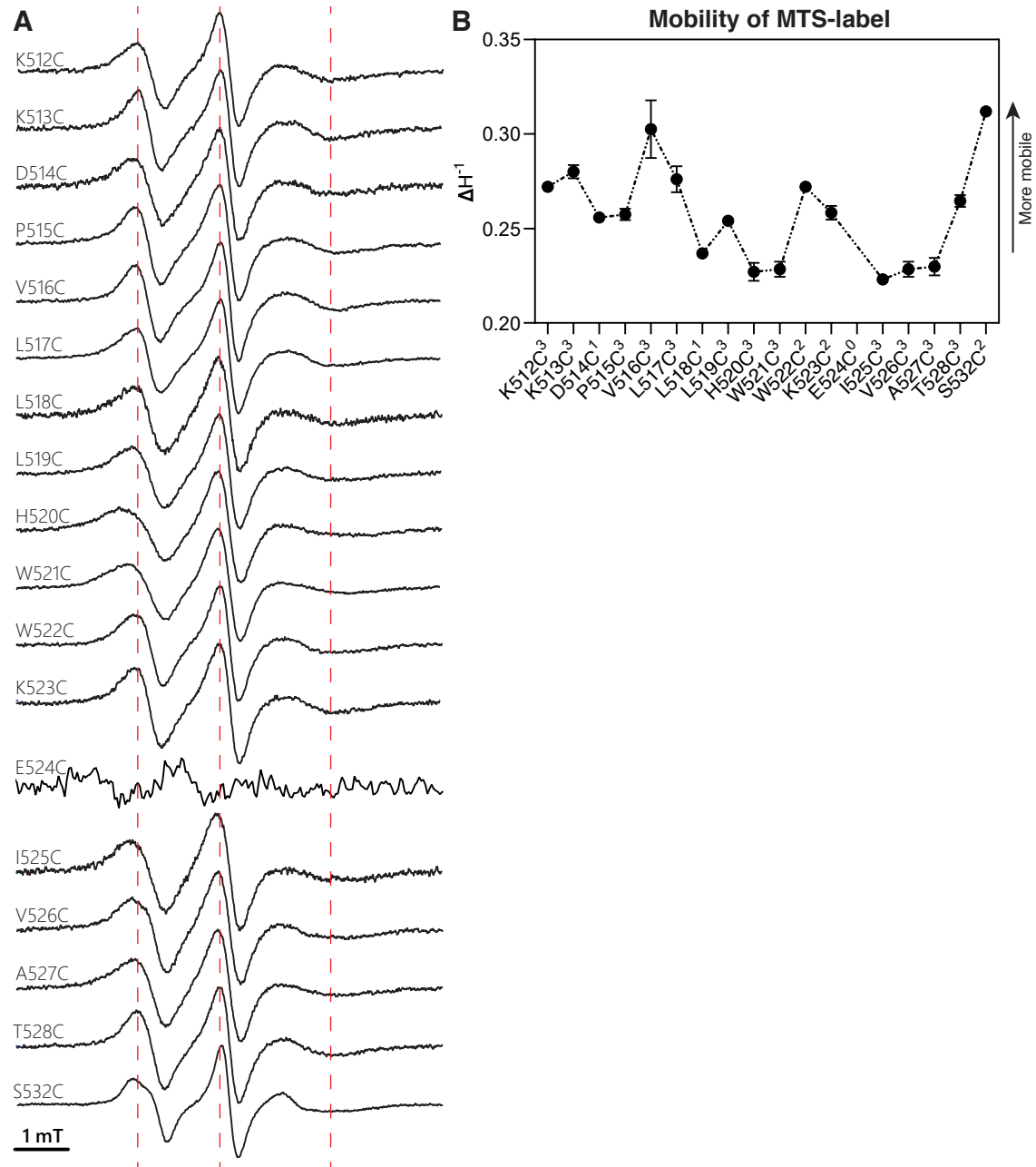


Figure 22: Mobility data of the PERK-TMR helix through RT cwEPR spectra.

(A) Representative EPR spectra from according PERK-TMR constructs reconstituted in a 100% POPC environment with an P:L of 1:3000, recorded at RT. The red lines act as visual aid. Each spectrum was processed by our script and normalized to the highest value being 100%. (B) The ΔH^{-1} value, which indicates the mobility of the MTS-label during the recording, was derived from spectra from A among others. n of used spectra equals the superscript number after the according protein specification. The points were connected to guide the eye.

7.6.2 EPR-Spectra of spin-labeled PERK-TMR at low temperature (-196 °C)

To get more indications of possible landmarks of the protein to lipid interface and possibly the exact location where the protein inserts into the lipid bilayer or where the PERK-TMR helix possibly experiences stereochemically protein-protein interactions (assuming a symmetrical dimerization behaviour and no intra-protein interactions), the polarity parameter ($2A_{zz}$) and the proximity parameter (L_f/M_f) had to be gathered from LT cwEPR spectra.

It was also possible to record significant and meaningful LT cwEPR spectra of nearly all tested PERK-TMR constructs (see Figure 23). The exception being again the E524C-PERK-TMR construct of which it was impossible to record an evaluateable cwEPR spectrum.

The polarity evaluation indicates:

1. The mean polarity decreases throughout the dataset. A deeper inserted part of the PERK-TMR has a more non-polar micro-environment than a part of PERK-TMR that is located in the solution surrounding the lipid bilayer.
2. The residues 520 and 521 are the most polar residues. This supports the theory that the residues 520-522 are in the plane of polar headgroups of the lipid bilayer and that the tryptophane act as anchoring residues.
3. Interestingly, the polarity does not decrease significantly until residue 525. The polar glutamate at position 524 is inside the plane of acyl-chains, which is energetically costly. It could potentially influence the water-membrane-interface by indenting the membrane, increasing the hydrophobic mismatch further and influencing the polarity of neighboring residues.

The proximity evaluation indicates:

1. Although the PERK-TMR was reconstituted at a low protein to lipid ratio of 1:3000 in a 100% POPC environment the EPR screening shows a signal, which happens if spin labels come close to each other. This indicates that a dimerization already occurs at such reconstitution parameters and that PERK is highly sensitive and prone to dimerization and maybe even oligomerisation.
2. The proximity increases C-terminally, indicating that the homodimers are coming near each other inside the acyl-chain plane of the membrane, whereas the N-terminus are facing away from each other.
3. Again the not recordable EPR spectrum of E524C could be caused by spin-spin interactions and spin exchange phenomena, if two spin-labels get extremely near to each other, indicating the glutamate as possibly the nearest point between to dimerising proteins (Molin, Salikhov, Zamaraev 1980).

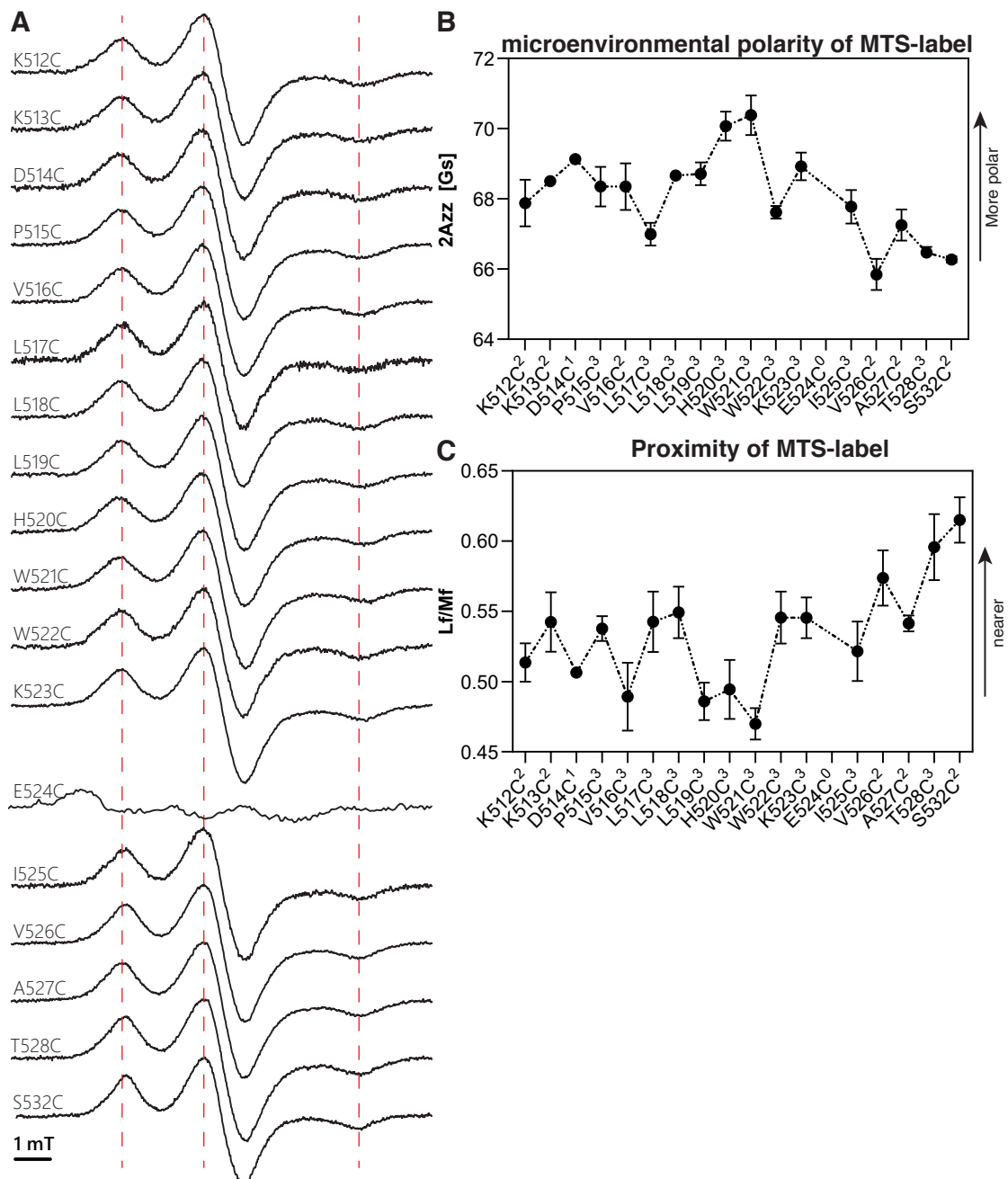


Figure 23: Proximity and micro-environmental polarity data of the PERK-TMR helix through low temperature cwEPR measurements.

(A) Representative EPR spectra from according PERK-TMR constructs reconstituted in a 100% POPC environment with a P:L of 1:3000, recorded at LT. The red lines act as visual aid. Each spectrum was processed by our script and normalized to the highest value being 100%. **(B)** The 2Azz value, which indicates the micro-environmental polarity around the MTS-label during the recording, was derived from spectra from **A** among others. n of used spectra equals the superscript number after the according protein specification. **(C)** The Lf/Mf ratio, which indicates the proximity of MTS-label during the recording, was derived from spectra from **A** among others. n of used spectra equals the superscript number after the according protein specification. **(B, C)** Points were connected to guide the eye.

7.7 The effect of different lipid environments on the PERK-TMR

The PERK-TMR was reconstituted into different lipid environments and cwEPR spectra recorded to further characterize the protein-lipid interface and to describe the mode of action of the PERK-TMR. If the PERK-TMR has a higher rate of dimerization at certain lipid environments, a general lipid dependence can be accepted.

7.7.1 Characterization of the used lipid environments

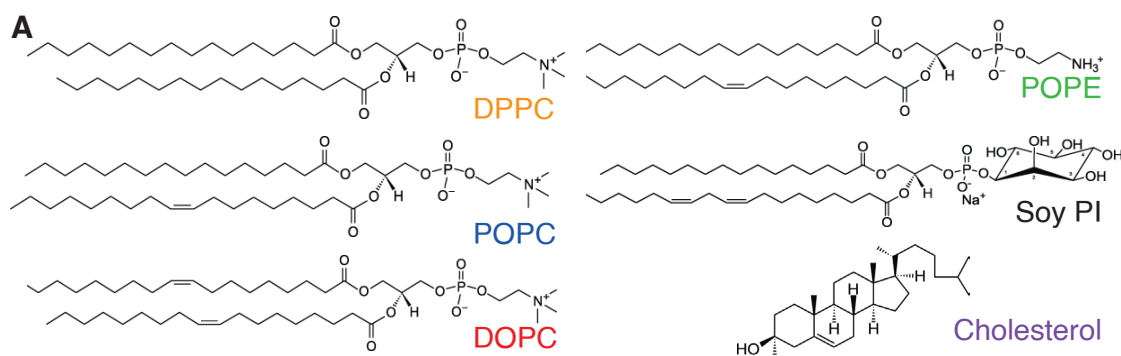


Figure 24: Structural formula of lipids used to engineer different lipid environments.
(A) Structural formula of lipids used in this work, derived from AvantiTM website.

To examine the possibility of a lipid dependent function of the PERK-TMR, different lipid environments were engineered using the lipids shown in Figure 24. They possess a wide range of different properties, e.g. different headgroups, different grade of saturation, and different physico-chemical properties.

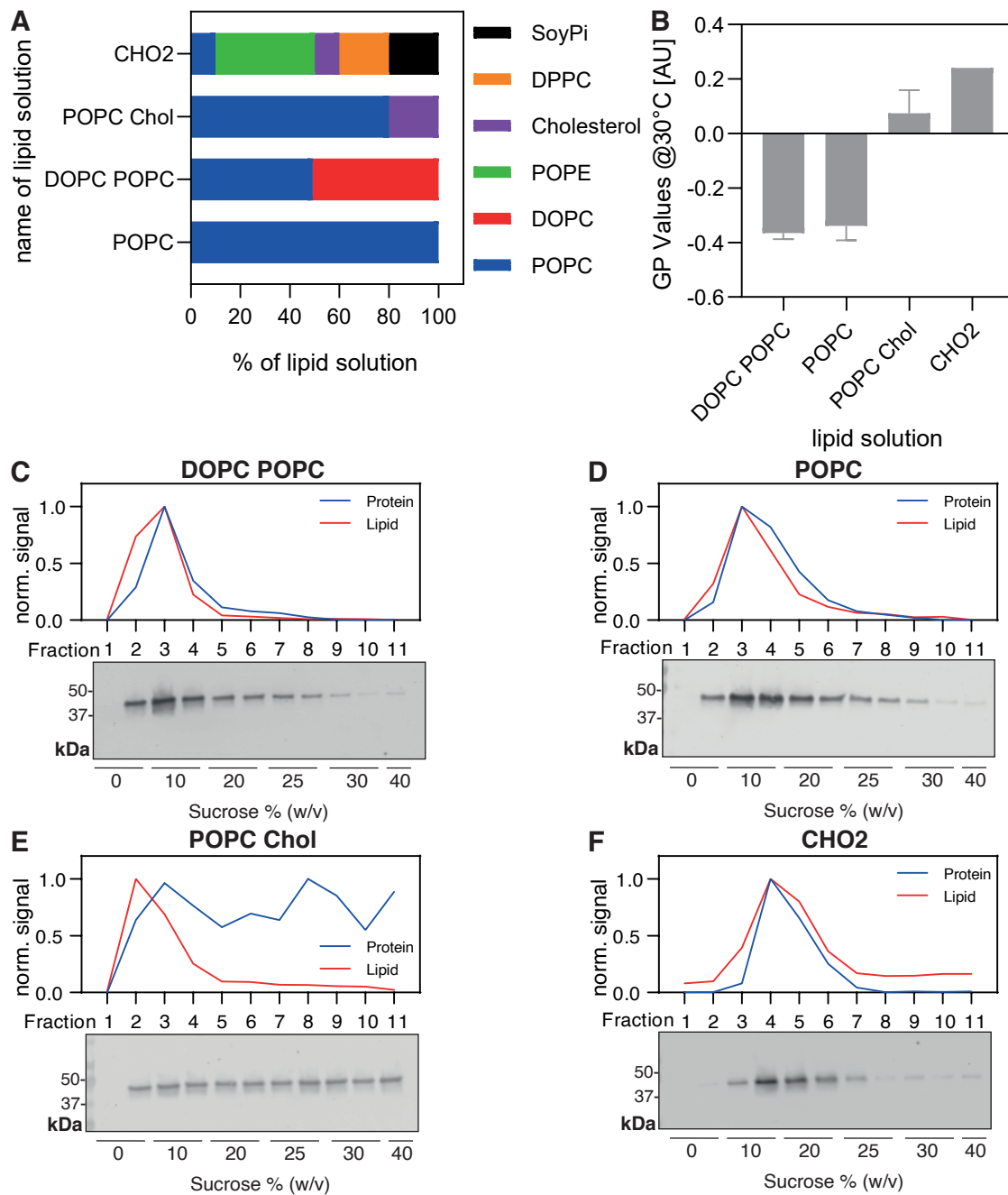


Figure 25: Characterization of the lipid mixtures used to simulate "ON" and "OFF" conditions of the UPR.

(A) The lipid compositions used in this step. Percentages of ingredients are indicated in mole percent. (B) GP values of lipid compositions from A recorded at 30 °C. N=2 for datasets with error bars otherwise n=1. The data is consistent with previously published data (Halbleib et al. 2017). (C-F) Quality control of reconstitution by sucrose gradient. Purified and labeled S532C PERK-TMR proteins were reconstituted in liposomes at a desired protein to lipid ratio of 1:1000 in according lipid environments. (C) Reconstituted in DOPC POPC environment. (D) Reconstituted in POPC environment. (E) Reconstituted in POPC Chol environment. (F) Reconstituted in CHO2 environment. (D-G) The signals were normalized, relative to the highest intensity in each data set.

In our research group different lipid environments were characterized as being an "ON" or "OFF" condition for the unfolded protein response (see Figure 25). This differentiation was established by experiments with yeast IRE1. The POPC as well as the DOPC POPC environment with its low packaging densities and general low headgroup complexity are seen as an "OFF" condition. The POPC Chol environment on the other hand is regarded as an "ON" condition, having a high lipid packaging density. The lipid mixture CHO2 is complex. It combines different characteristics, which are comparable to lipidome changes in yeast cells leading to lipid bilayer stress: increased PE:PC ratio, increased degree of lipid saturation, and an increased sterol content (Thibault et al. 2012; Pineau et al. 2009). The CHO2 environment is regarded as an "ON" condition.

The PERK-TMR reconstitutes differently into the various lipid environments, as the sucrose gradient in Figure 25 **C-F** suggests: The lipid and protein intensity peaks overlap by a high margin in case of the POPC, DOPC POPC and CHO2 environment, suggesting a successful reconstitution, whereas the lipid-protein intensities of the POPC Chol reconstitution deviate, suggesting a failed stable integration of the PERK-TMR into the POPC Chol lipid environment.

7.7.2 Lipids lead to a pronounced change in the cwEPR spectra of PERK-TMR

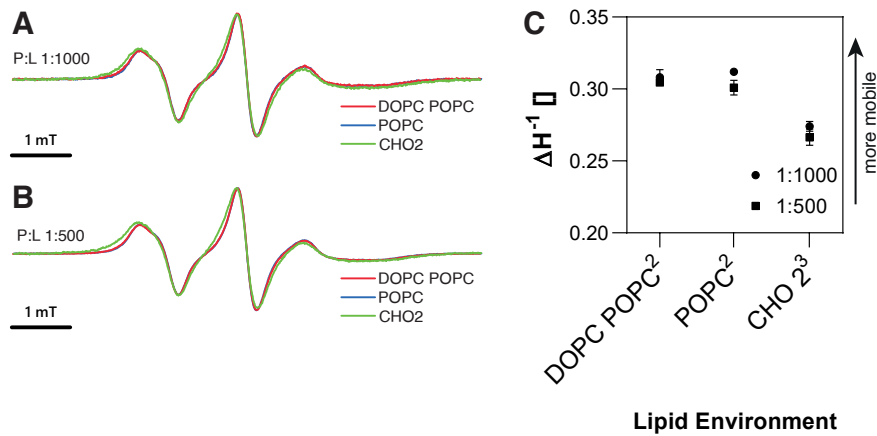


Figure 26: The CHO2 lipid mixture leads to a pronounced broadening of the RT EPR spectrum of our native cysteine construct.

(A) Representative EPR spectra from our native cysteine PERK-TMR construct reconstituted in according lipid environments with a P:L of 1:1000, recorded at RT. Each spectrum was processed by our script and normalized to the highest value being 100%. (B) Representative EPR spectra from our native cysteine PERK-TMR construct reconstituted in according lipid environments with a P:L of 1:500, recorded at RT. Each spectrum was processed by our script and normalized to the highest value being 100%. (C) The ΔH^{-1} value, which indicates the mobility of the MTS-label during the recording, was derived from spectra from A and B among others. n of used spectra equals the superscript number after the according lipid environment.

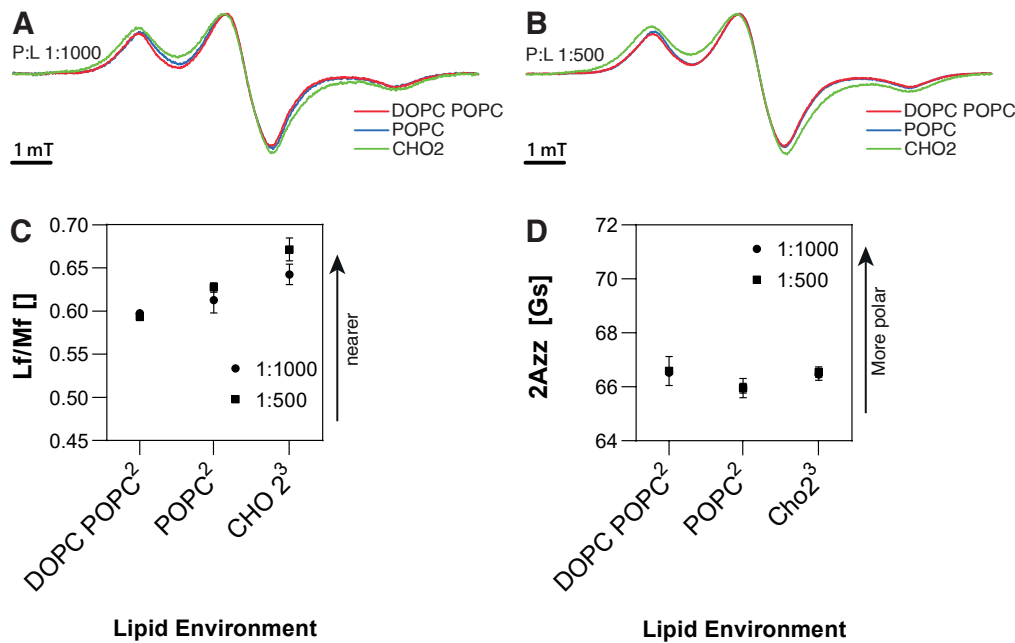


Figure 27: The CHO2 lipid mixture leads to a pronounced broadening of the LT EPR spectrum of our native cysteine construct.

(A) Representative EPR spectra from our native cysteine PERK-TMR construct reconstituted in according lipid environments with a P:L of 1:1000, recorded at LT. Each spectrum was processed by our script and normalized to the highest value being 100%. **(B)** Representative EPR spectra from our native cysteine PERK-TMR construct reconstituted in according lipid environments with a P:L of 1:500, recorded at LT. Each spectrum was processed by our script and normalized to the highest value being 100%. **(C)** The Lf/Mf ratio, which indicates the proximity of MTS-label during the recording, was derived from spectra from **A** and **B** among others. n of used spectra equals the superscript number after the according lipid environment. **(D)** The 2Azz value, which indicates the micro-environmental polarity around the MTS-label during the recording, was derived from spectra from **A** and **B** among others. n of used spectra equals the superscript number after the according protein specification.

The CHO2 lipid environment leads to pronounced changes in both the RT as well as the LT cwEPR spectra (see Figures 26 and 27). If the PERK-TMR helix is inserted in a CHO2 lipid environment, the MTS label is less mobile and nearer to a second MTS label, in comparison to the DOPC POPC and POPC environment. This could possibly follow from an even higher proportion of dimerization. The micro-environmental polarity is not influenced by CHO2.

The lipid environment indeed has an influence on the lipid-protein interface of the PERK-TMR. This effect can be attributed to different lipid properties of the CHO2 environment: A high lipid packaging density, a different PE:PC ratio, an increase in sterol content, the Soy PI headgroup, or DPPC content.

To further characterize the influence of CHO2 to the protein-lipid interface of the PERK-TMR, the properties of the CHO2 environment were disassembled and tested individually.

7.7.3 POPE has no effect on the dimerization of PERK-TMR

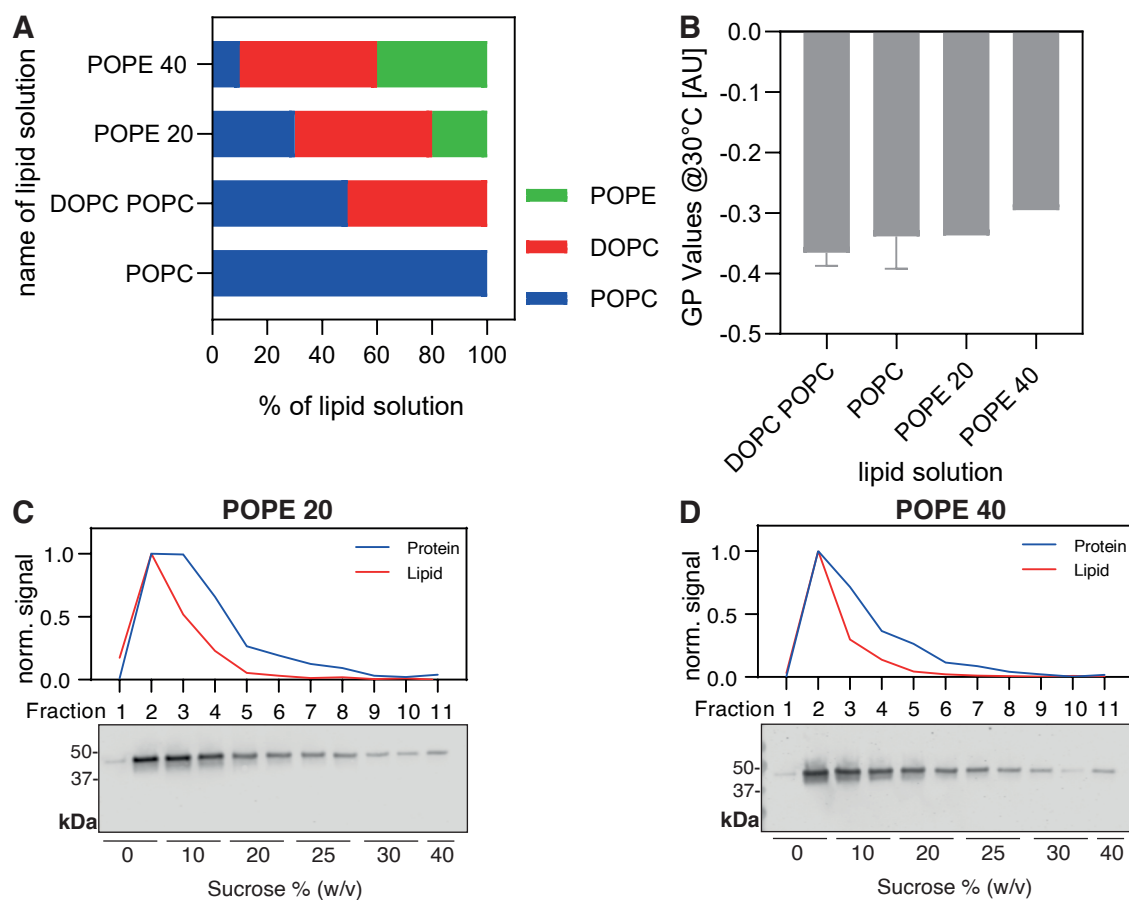


Figure 28: Characterization of the lipid mixtures used to examine the effect of various PE:PC ratios on the PERK-TMR and its reconstitution success.

(A) The lipid compositions used in this work. Percentages of ingredients are indicated in mole percent. (B) GP values of lipid compositions from A recorded at 30 °C. N=2 for datasets with error bars, otherwise n=1. The data is consistent with previously published data (Halbleib et al. 2017). (C-D) Quality control of reconstitution by sucrose gradient. Purified and labeled S532C PERK-TMR proteins were reconstituted in liposomes at a desired protein to lipid ratio of 1:1000 in according lipid environments. (C) Reconstituted in POPE 20 environment. (D) Reconstituted in POPE 40 environment. (C-D) The signals were normalized, relative to the highest intensity in each data set.

The effect of different PE:PC ratios can be examined with POPC, DOPC POPC, POPE 20, and POPE 40 (see Figure 28). All lipid environments have a comparably low GP value. The PERK-TMR can be successfully reconstituted in all lipid environments.

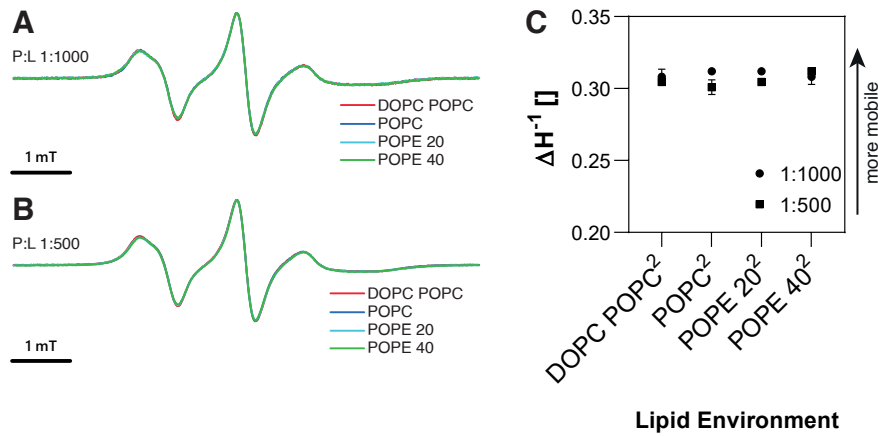


Figure 29: A increase of POPE in the lipid mixture has no effect on the RT EPR spectrum of our native cysteine construct.

(A) Representative EPR spectra from our native cystein PERK-TMR construct reconstituted in according lipid environments with a P:L of 1:1000, recorded at RT. Each spectrum was processed by our script and normalized to the highest value being 100%. (B) Representative EPR spectra from our native cystein PERK-TMR construct reconstituted in according lipid environments with a P:L of 1:500, recorded at RT. Each spectrum was processed by our script and normalized to the highest value being 100%. (C) The ΔH^{-1} value, which indicates the mobility of the MTS-label during the recording, was derived from spectra from A and B among others. n of used spectra equals the superscript number after the according lipid environment.

The POPE content in the lipid environment has no effect on the RT cwEPR spectrum of the samples. POPE does not effect the mobility of the native S532C of the PERK-TMR.

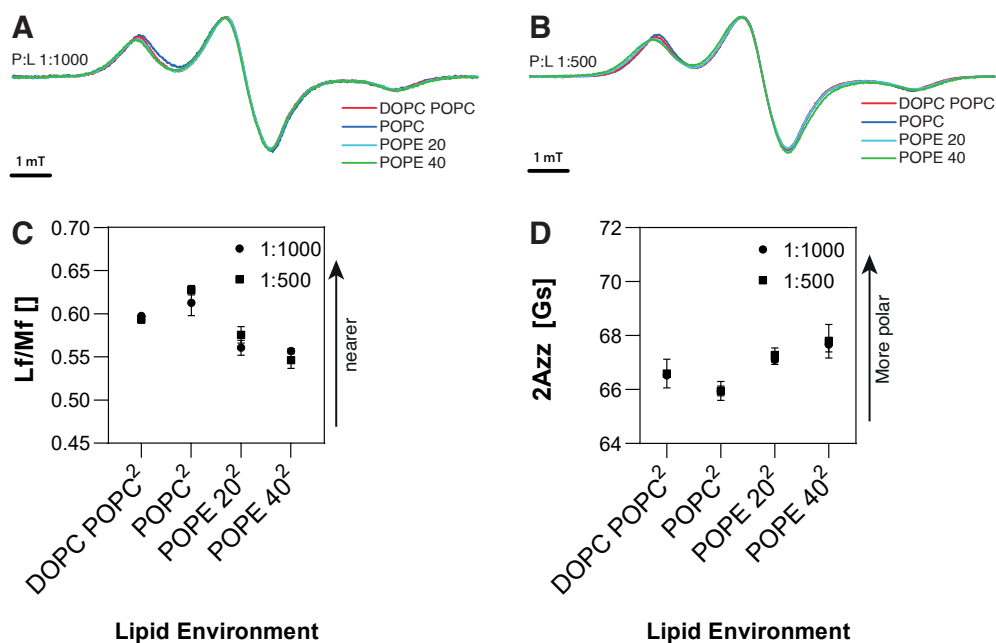


Figure 30: A increase of POPE in the lipid mixture leads to a minuscule broadening of the LT EPR spectrum of our native cysteine construct.

(A) Representative EPR spectra from our native cystein PERK-TMR construct reconstituted in according lipid environments with a P:L of 1:1000, recorded at LT. Each spectrum was processed by our script and normalized to the highest value being 100%. (B) Representative EPR spectra from our native cystein PERK-TMR construct reconstituted in according lipid environments with a P:L of 1:500, recorded at LT. Each spectrum was processed by our script and normalized to the highest value being 100%. (C) The Lf/Mf ratio, which indicates the proximity of MTS-label during the recording, was derived from spectra from A and B among others. n of used spectra equals the superscript number after the according lipid environment. (D) The 2A_{zz} value, which indicates the micro-environmental polarity around the MTS-label during the recording, was derived from spectra from A and B among others. n of used spectra equals the superscript number after the according protein specification.

The POPE content in the lipid environment leads to a minuscule broadening of the LT cwEPR spectrum. POPE leads to no increase of the dimerization of the PERK-TMR. It leads to an increase of the micro-environmental polarity around the native S532C of the PERK-TMR.

The POPC content is not able to explain the changes which occur to the PERK-TMR in connection with the CHO2 lipid environment.

7.7.4 Cholesterol at high concentrations make an reconstitution of PERK impossible

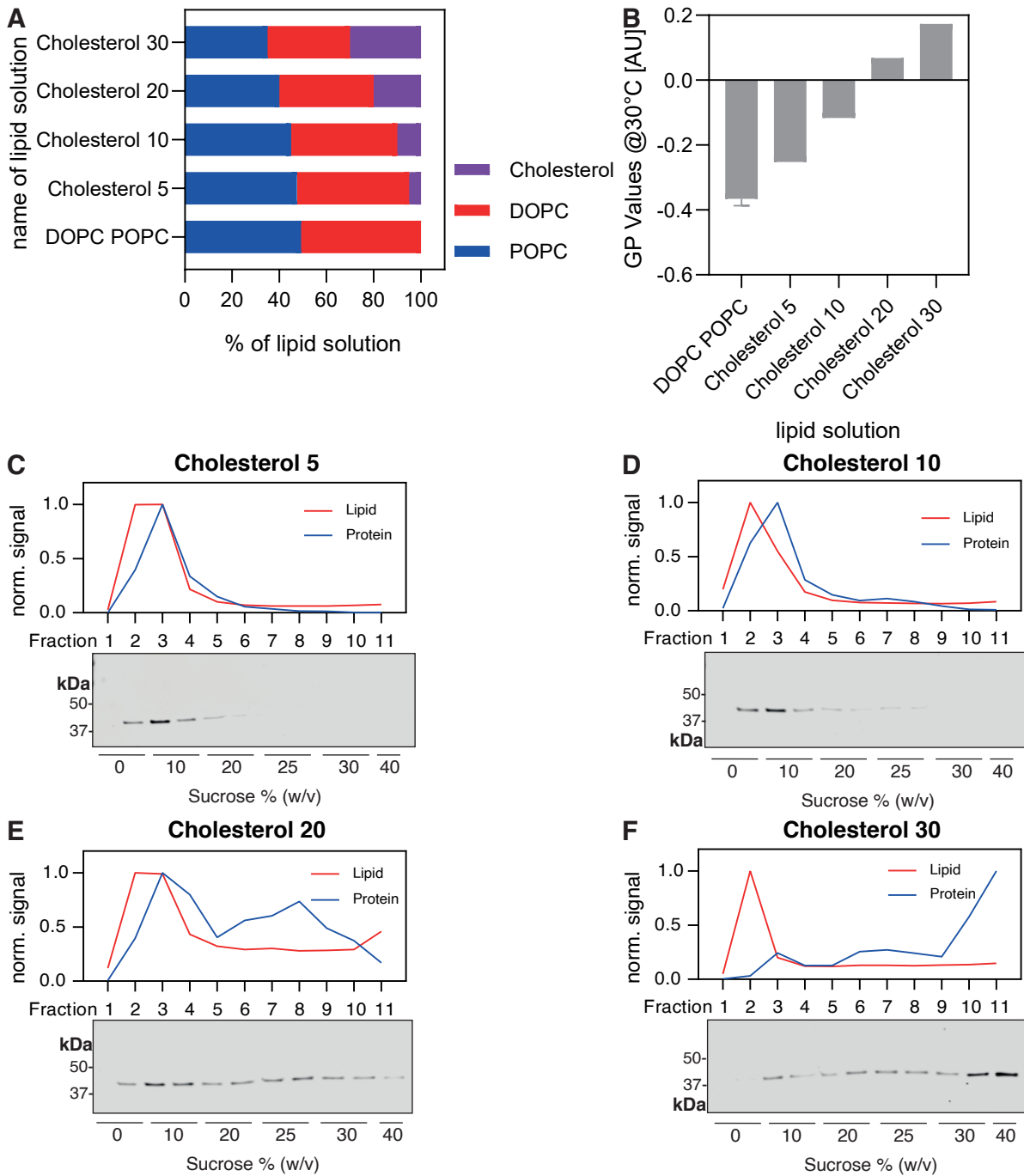


Figure 31: Characterization of the lipid mixtures used to examine the effect of various lipid packaging densities on the PERK-TMR and its reconstitution success.

(A) The lipid compositions used in this work. Percentages of ingredients are indicated in mole percent. (B) GP values of lipid compositions from A recorded at 30 °C. N=2 for datasets with error bars, otherwise n=1. The data is consistent with previously published data (Halbleib et al. 2017). (C-F) Quality control of reconstitution by sucrose gradient. Purified and labeled S532C PERK-TMR proteins were reconstituted in liposomes at a desired protein to lipid ratio of 1:1000 in according lipid environments. (C) Reconstituted in Cholesterol 5 environment. (D) Reconstituted in Cholesterol 10 environment. (E) Reconstituted in Cholesterol 20 environment. (F) Reconstituted in Cholesterol 30 environment. (C-F) The signals were normalized, relative to the highest intensity in each data set.

The effect of different lipid packaging densities and cholesterol ratios can be examined with POPC, DOPC POPC, Cholesterol 5, Cholesterol 10, Cholesterol 15, and Cholesterol 20 (see Figure 31). The GP value, which represents the lipid packaging density, increases to the same extent as the cholesterol content. The PERK-TMR can be successfully reconstituted in the Cholesterol 5 and Cholesterol 10 lipid environments. Higher amounts of cholesterol lead to a deviation of the lipid and protein intensity peaks, suggesting an unstable protein integration and an unsuccessful reconstitution.

The effect of the cholesterol content of CHO2 can still be evaluated, as a successful reconstitution in a Cholesterol 10 environment is possible, which contains the same cholesterol content as CHO2. Meanwhile, the high lipid packaging density of CHO2 can not be evaluated.

The enlarged protein-lipid-interface of the PERK-TMR in conjunction with the highly rigid cholesterol lipid environment seems to make a reconstitution energetically impossible. If the cholesterol content is increased after an already successful reconstitution, higher cholesterol contents could be examined.

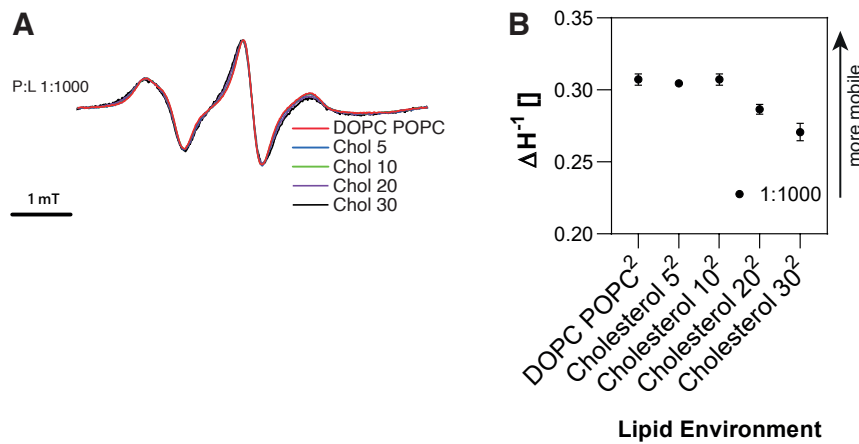


Figure 32: An increase of cholesterol in the lipid mixture only has a pronounced effect on the RT EPR spectrum of our native cysteine construct at high concentrations.

(A) Representative EPR spectra from our native cysteine PERK-TMR construct reconstituted in according lipid environments with a P:L of 1:1000, recorded at RT. Each spectrum was processed by our script and normalized to the highest value being 100%. (B) The ΔH^{-1} value, which indicates the mobility of the MTS-label during the recording, was derived from spectra from A among others. n of used spectra equals the superscript number after the according lipid environment.

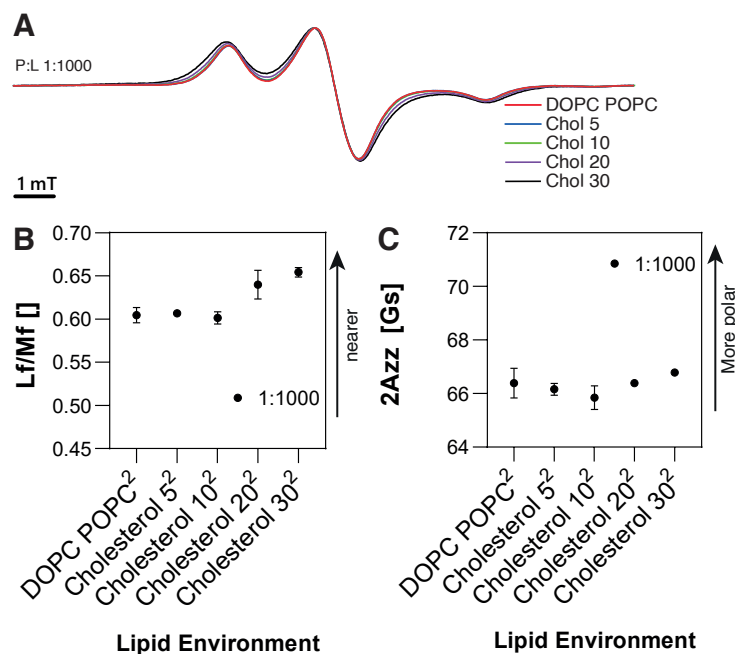


Figure 33: An increase of cholesterol in the lipid mixture only has a pronounced effect on the LT EPR spectrum of our native cysteine construct at high concentrations.

(A) Representative EPR spectra from our native cysteine PERK-TMR construct reconstituted in according lipid environments with a P:L of 1:1000, recorded at LT. Each spectrum was processed by our script and normalized to the highest value being 100%. **(B)** The Lf/Mf ratio, which indicates the proximity of MTS-label during the recording, was derived from spectra from **A** among others. n of used spectra equals the superscript number after the according lipid environment. **(C)** The 2Azz value, which indicates the micro-environmental polarity around the MTS-label during the recording, was derived from spectra from **A** among others. n of used spectra equals the superscript number after the according protein specification.

Cholesterol has an effect, both on the RT as well as the LT spectrum, at high concentrations (see Figures 32 and 33). Cholesterol contents of 20-30 mole % lead to a broadening of RT as well as LT spectra. The MTS labels, which are attached to the native S532C, are nearer to each other, more immobile, and in a slightly more polar micro-environment than their counterparts that are inserted into a DOPC POPC or POPC environment. This change can be explained by the subpar reconstitution success and forming of protein dimers (see protein signal at the bottom fraction of Figure 31 **F**). At cholesterol contents comparable to the CHO2 environment, no significant change in RT as well as LT cwEPR spectra can be observed.

7.7.5 Soy PI shows no effect on the cwEPR spectra of PERK-TMR

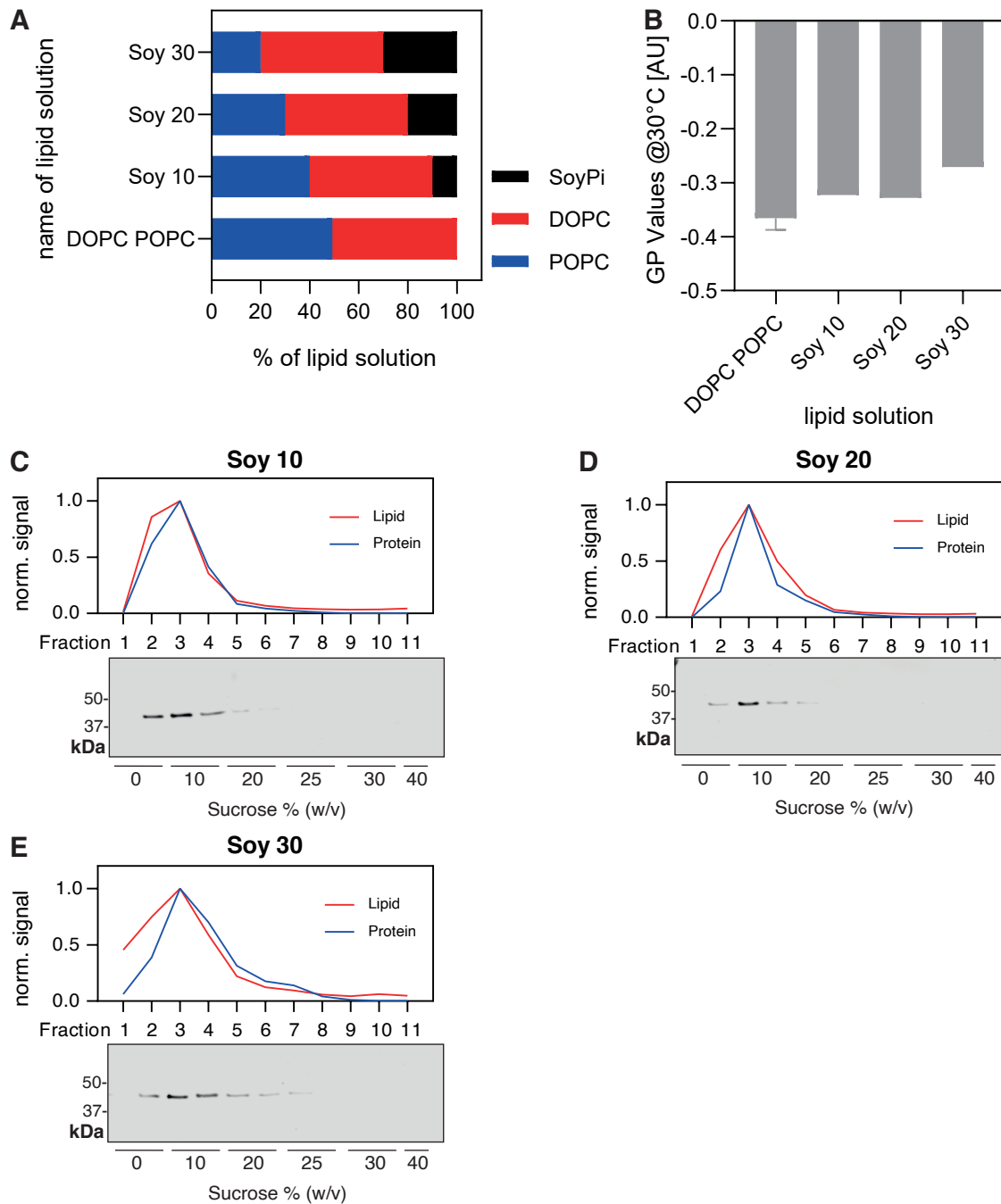


Figure 34: Characterization of the lipid mixtures used to examine the effect of various Soy PI contents on the PERK-TMR and its reconstitution success.

(A) The lipid compositions used in this work. Percentages of ingredients are indicated in mole percent. (B) GP values of lipid compositions from A recorded at 30 °C. N=2 for datasets with error bars, otherwise n=1. The data is consistent with previously published data (Halbleib et al. 2017). (C-E) Quality control of reconstitution by sucrose gradient. Purified and labeled S532C PERK-TMR proteins were reconstituted in liposomes at a desired protein to lipid ratio of 1:1000 in according lipid environments. (C) Reconstituted in Soy 10 environment. (D) Reconstituted in Soy 20 environment. (E) Reconstituted in Soy 30 environment. (C-E) The signals were normalized, relative to the highest intensity in each data set.

To examine the effect of Soy PI, containing a *phosphatidylinositol* instead of a *phosphocholine* headgroup, DOPC POPC, POPC, Soy 10, Soy 20, and Soy 30 were used (see Figure 34). The reconstitution is successful in all environments and the lipid packaging density is comparatively low in all environments.

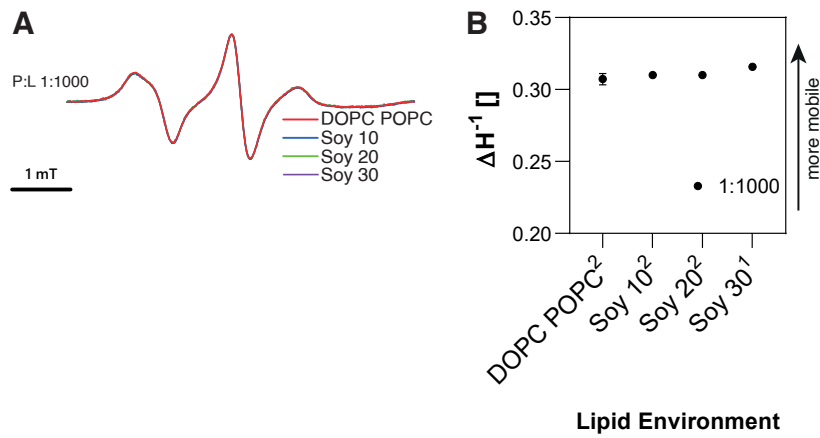


Figure 35: A increase of Soy PI in the lipid mixture has no effect on the RT EPR spectrum of our native cysteine construct.

(A) Representative EPR spectra from our native cystein PERK-TMR construct reconstituted in according lipid environments with a P:L of 1:1000, recorded at RT. Each spectrum was processed by our script and normalized to the highest value being 100%. **(B)** The ΔH^{-1} value, which indicates the mobility of the MTS-label during the recording, was derived from spectra from **A** among others. n of used spectra equals the superscript number after the according lipid environment.

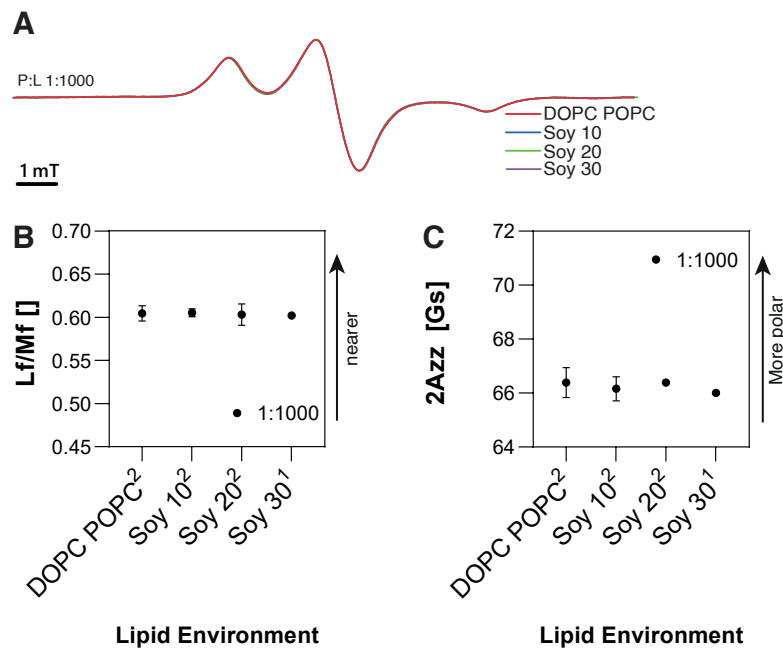


Figure 36: A increase of Soy PI in the lipid mixture has no effect on the LT EPR spectrum of our native cysteine construct.

(A) Representative EPR spectra from our native cysteine PERK-TMR construct reconstituted in according lipid environments with a P:L of 1:1000, recorded at LT. Each spectrum was processed by our script and normalized to the highest value being 100%. **(B)** The Lf/Mf ratio, which indicates the proximity of MTS-label during the recording, was derived from spectra from **A** among others. n of used spectra equals the superscript number after the according lipid environment. **(C)** The 2Azz value, which indicates the micro-environmental polarity around the MTS-label during the recording, was derived from spectra from **A** among others. n of used spectra equals the superscript number after the according protein specification.

Neither in the RT nor in the LT spectrum can an effect of Soy PI be seen (see Figures 35 and 36).

8 Discussion

8.1 Establishment of a robust system for examining PERK-TMR through cwEPR

Utilizing a minimal PERK-TMR construct coupled with an MBP-tag for purification, we have significantly improved the reconstitution process of various PERK-TMR mutants across different lipid environments. We consistently obtained high-quality EPR spectra, which were analyzed automatically (see Figure 21). This method effectively mitigates a potential researcher bias and enhances reproducibility.

8.2 Experimental insights into PERK-TMR: The transition zone between amphipathic and transmembrane helix

Evaluation of the RT cwEPR spectra does not identify a clear helical pattern of spin probe mobility along the residues of the predicted amphipathic helix. Unlike the juxta-membrane amphipathic helix described in baker's yeast IRE1 (Halbleib et al. 2017), the amphipathic helix of PERK does not insert deeply into the lipid bilayer. However, to study the structure and dynamics of PERK's juxta-membrane region and its interactions with the lipid bilayer, more experiments are required. A rather shallow insertion of PERK's amphipathic helix into the lipid bilayer would also be consistent with the systematic EPR data with respect to spin probe polarity (see Figure 23). The relatively high degree of polarity reported by spin probes installed from residue K512 to I525 indicates that most residues in this region face the aqueous environment or the polar lipid headgroup region. Nevertheless, the lower polarity reported for a spin probe installed at position L517, and even more so at residues V525 to T528, indicates some interaction of this juxta-membrane region with the lipid bilayer.

When the spin probe is installed at the position of W521 or W522, a particularly high polarity was observed, which may indicate a positioning of the spin probe in the region of the negatively charged phosphate moieties. Tryptophan residues, known for anchoring membranes through their indole groups, stabilize their surroundings and are often enriched in the lipid headgroup region of transmembrane proteins (Situ et al. 2018). This interpretation is supported by the low mobility of spin probes installed in this region (H520 and W521) as a possible consequence from particularly tight lipid packing in the water-membrane interface. Charged residues nearby (H520, K523, E524) may contribute to bilayer deformation and the increased local polarity. A possible connection between our biophysical data and human disease is provided by the very rare Wolcott-Rallison syndrome (literature suggests under 100 cases worldwide), which has been attributed to a point mutation at W552X in humans (Ozbek et al. 2010; Senée et al. 2004), where individuals experience fetal diabetes mellitus, hepatic failure, and, if survived, severe epiphyseal dysplasia (Juneja, Sultan, Bhatnagar 2012).

Notably, the glutamate at position 524 (E524) is, according to MD simulations (conversation with Dr. Roberto Covino) in a similar position between the amphipathic helix and the transmembrane helix as the functionally important residue E540 in the yeast IRE1 (Väth et al. 2021). Indeed, E524 also causes lipid disordering and water penetration into the lipid bilayer according to MD simulations (conversation with Dr. Roberto Covino).

Crosslinking experiments on yeast IRE1 revealed a crossover at position F544C (Väth et al.

2021) just below the plane of polar headgroups. The absence of a recordable EPR spectrum at E524C in our PERK experiments, despite three new attempts after protein purification, could be due to spin-spin interactions when two spin-labels are extremely close to each other (Molin, Salikhov, Zamaraev 1980; Salikhov 2021). We speculate that the overall architecture of the trans-membrane domain may be shared among yeast IRE1 and human PERK, but that the position of the ‘crossing point’ where two neighboring helices interact most intimately may have shifted towards the lipid headgroup region in PERK. Beyond that, our EPR data suggests that interacting PERK helices show a higher proximity in the C-terminal regions inserted in the lipid bilayer compared to the N-terminal regions, which seem to point way from each other (see Figure 23). A further experimental validation, e.g. by systematic crosslinking experiments in a native ER membrane environment, would be helpful to determine the overall architecture and biologically relevant configuration of PERK in signalling-active oligomers.

8.3 Mechanical activation of the PERK-TMR

The reconstitution of PERK-TMR in liposomes of defined lipid composition is challenging due to PERK’s inherent resistance to bilayer insertion, which can lead to protein aggregation during the reconstitution procedure. Despite these challenges, we collected firm evidence that the oligomerization of PERK is increased when lipid packing increases and the membrane compressibility is reduced. Notably, this reflects the behavior of the yeast IRE1, which uses a hydrophobic mismatch-based mechanism to sense and respond to conditions of low ER membrane compressibility (Halbleib et al. 2017; Văth et al. 2021; Renne, Ernst 2023).

One of the tested lipid environments used to investigate the behavior of PERK was engineered to mimic several conditions that have been previously associated with lipid bilayer stress and membrane-based UPR activation. We successfully and efficiently reconstituted PERK in liposomes composed of these tightly packing lipids (see Figure 25) and observed the highest degree of PERK dimerization/oligomerization in all experiments (see Figures 26 and 27). We then undertook steps to identify the ‘active’ compound or relevant property by testing the impact of individual components from the complex CHO2 lipid mix. Efforts to attain a comparable degree of lipid packing by the inclusion of cholesterol resulted in a high degree of protein loss during the reconstitution process (see Figure 31). Despite that, we observed a significant spectral broadening when PERK was reconstituted in lipid environments containing increasing concentrations of cholesterol (see Figures 33 and 32). This suggests that PERK may use a similar hydrophobic mismatch-based mechanism as the yeast IRE1 (Halbleib et al. 2017; Renne, Ernst 2023), which renders PERK sensitive to reduced membrane compressibility.

Furthermore, a last dataset regarding the influence of DPPC was not examined, because of DPPC’s tendency to form a gelling phase in higher concentrations, leading to a local enrichment of DPPC and, conversely, to a further enrichment of PERK-TMR in the remaining membrane. Whether a gelling phase induced by the 20% DPPC in CHO2 might be responsible for the pronounced change in the spectra seems unlikely but cannot be completely ruled out. To increase certainty, a dilution series of DPPC/protein to lipid ratio could be prepared and potentially validated with another method (e.g. Förster resonance energy transfer (FRET), which could differentiate room-temperature and low-temperature environments).

PERK behaves differently from other membrane-sensing proteins. For instance, while ATF6

is activated by dihydrosphingosine as well as dihydroceramide (Tam et al. 2018), it is not influenced by lipid saturation (Kitai et al. 2013). Conversely, Mga2 also appears to act as a sensor of membrane saturation, detecting lateral compressibility of the membrane via an intramembrane-located tryptophan and orienting itself rotationally to a neighboring Mga2 depending on lateral membrane compressibility (Ballweg et al. 2020).

Close monitoring of membrane compressibility and thickness seems particularly useful in the context of the endoplasmic reticulum (ER) and protein production/translocation. Cell membranes not only compartmentalize the organelles of a cell but are also heavily compartmentalized themselves (Prasad, Sliwa-Gonzalez, Barral 2020), giving rise to distinct functional centers and serving as an additional sorting mechanism for proteins and contact sites with other organelles (X. Wu, Rapoport 2021).

Notably, the PERK-TMR was reconstituted initially at a relatively low protein to lipid ratio of 1:1000 in a 100% POPC ("OFF") membrane environment, compared to previous reconstitutions of the yeast IRE1 (Halbleib et al. 2017). Nevertheless, the PERK-TMR does seem to oligomerize in this environment to a considerable extent (see Figure 17). Hence, the PERK-TMR exhibits a higher tendency to oligomerizes, which is likely to be functionally relevant. Further EPR experiments could involve utilizing even lower protein to lipid ratios or employing a spin dilution model to more precisely discern the influence of the lipid membrane on the spin label and the influence from oligomerization.

Having achieved a reliable reconstitution of the PERK-TMR in liposomes, it may become feasible to insert the protein in 'permissive' liposomes first, before altering the lipid composition either by delivering specific lipids such as cholesterol to the proteoliposomes or by metabolically perturbing the lipid composition using lipid hydrolases or other lipid metabolic enzymes. This work represents an important step towards studying and understanding the role of lipid in PERK activation and opens new opportunities to stage crucial biochemical events underlying complex metabolic disorders associated with chronic ER stress.

9 Appendix

9.1 Python code for semi-automatic EPR spectra analysis

```

1  # automatic EPR spectra analysis
2  # todo: user eingabe = "LT", "rt", "yes", "no"

3  import pandas as pd
4  import numpy as np
5  import matplotlib.pyplot as plt
6  import glob
7  from scipy.optimize import fsolve, curve_fit, leastsq
8  from scipy.interpolate import interp1d

9  np.set_printoptions(threshold=np.inf)
10 #import x/y values
11 csvv=[]
12 print("modus? TT oder RT")
13 modus=input()
14 print("Lese Daten...")

15 counter=-1
16 file = {}
17 for filename in glob.glob('*.oaf'):
18     file[filename[:-4]] = pd.read_csv(filename, sep='\s+', skiprows=1, header=None,
19     ↪ names=['X', 'G-val', 'Y'])
20     counter=counter+1
21     #print(file)

22     data=file[filename[:-4]]
23 # smoothing um mAn=[x]
24     mAn=[1]
25     for durchschnitt_n in mAn:
26         print("Smoothing Average="+str(durchschnitt_n)+" Nachbarn...")

27         data["MA_Y"]=data.rolling(window=durchschnitt_n)["Y"].mean()

28 #moving average
29 x=data["X"][durchschnitt_n:].values
30 #print(data[10:12]["MA_Y"]-data[15]["MA_Y"].values
31 #establishing of baseline
32 if (modus=="TT"):
33     xx1=np.argmax(x>3315)
34     xx2=np.argmax(x>3335)
35     xx3=np.argmax(x>3450)
36 else:
37     xx1=np.argmax(x>3453)
38     xx2=np.argmax(x>3463)
39     xx3=np.argmax(x>3528)
40 #moving average
41 #print(data[10:12]["MA_Y"]-data[15]["MA_Y"].values
42 #establishing of baseline
43 """
44 xa=data[xx1:xx1+10]["X"].values[0]
45 ya=data[xx1:xx1+10]["MA_Y"].values.mean()

46 print("Anfangswerte für die Baseline sind: "+str(xa)+"/"+str(ya))

47 #xy end
48 xe=data[xx2:xx2+10]["X"].values[0]

```

```

48     ye=data[xx2:xx2+10]["MA_Y"].values.mean()
49     #x/y beginning
50     """

51     xa=data[xx1:xx1+10]["X"].values[0]
52     ya=data[xx1:xx1+10]["MA_Y"].values.mean()
53     print("Anfangswerte für die Baseline sind: "+str(xa)+"/"+str(ya))
54     #xy end
55     xe=data[xx3:xx3+10]["X"].values[0]
56     ye=data[xx3:xx3+10]["MA_Y"].values.mean()
57     print("Endwerte für die Baseline sind: "+str(xe)+"/"+str(ye))
58     print("Baseline equation nach y=mx+z")
59     #make baseline equation y=mx+z
60     #print("Line through("+str(xa)+"/"+str(ya)+")("+str(xe)+"/"+str(ye)+")")
61     m=(ye-ya)/(xe-xa)
62     z=ye-xe*m
63     print("y="+str(m)+"x"+str(z))
64     baseline= "y="+str(m)+"x"+str(z)
65     data["BL"]=data["MA_Y"]-(m*data["X"]+z)
66     #removing of baseline
67     plt.plot(data["X"], (m*data["X"]+z), '--', label= baseline)
68     plt.plot(data["X"], data["MA_Y"], '-')
69     plt.plot(xa, ya, 'ro', zorder=10)
70     plt.plot(xe, ye, 'ro', zorder=10)
71     plt.plot(xe, ye, 'ro', zorder=10)
72     plt.legend([baseline], loc='best')
73     plt.plot(data["X"], data["BL"], '-', label= "baseline")
74     print("Baseline wird abgezogen...")
75     y=data["BL"][durchschnitt_n:].values
76     f = interp1d(x, y, axis=0, fill_value="extrapolate")
77     print(data["BL"][10:].idxmax())
78     init=data.loc[data["BL"].idxmax()]["X"]+1
79     def get_x0(f, init):
80         done=False
81         print("Suche Anfang für x=0-Algorithmus...")
82         while done==False:
83             x=fsolve(f, init)
84             #print(init)
85             if x > (data.loc[data["BL"].idxmax()]["X"]) and x < data.loc[data["BL"].idxmin()]["X"]:
86                 return x
87                 done=True
88             else:
89                 done=False
90                 init=init+0.2
91     x0=get_x0(f, init)
92     print("x0="+str(x0))
93     print("Standardisiere Spektren...")

94     data["move"]=data["X"]-x0

95     xnew = data["move"][durchschnitt_n:]
96     #split data in several fields
97     """plt.plot(xnew, f(x), '-')
98     plt.axhline(y=0, color='black', linestyle='-')
99     plt.show()"""
100     varybl= np.sqrt((sum((y[xx1:xx2]-y[xx1:xx2].mean())**2))/(xx2-xx1))
101     if (modus=="TT"):
102         xlh=(data["move"][data.index[(data["move"].values>-36) & (data["move"].values<-35.5)]] [0] :
103         ↪ data.index[(data["move"].values>-18) & (data["move"].values<-17.5)]] [0]).values)
103         ylh=(data["BL"][data.index[(data["move"].values>-36) & (data["move"].values<-35.5)]] [0] :
104         ↪ data.index[(data["move"].values>-18) & (data["move"].values<-17.5)]] [0]).values)

```

```

104     xll=(data["move"][data.index[(data["move"].values>-21) & (data["move"].values<-20.5)])[0] :
    ↪ data.index[(data["move"].values>-10) & (data["move"].values<-9.5)])[0].values)
105     yll=(data["BL"][data.index[(data["move"].values>-21) & (data["move"].values<-20.5)])[0] :
    ↪ data.index[(data["move"].values>-10) & (data["move"].values<-9.5)])[0].values)
106     xmh=(data["move"][data.index[(data["move"].values>-11) & (data["move"].values<-10.5)])[0] :
    ↪ data.index[(data["move"].values>-2) & (data["move"].values<-1.5)])[0].values)
107     ymh=(data["BL"][data.index[(data["move"].values>-11) & (data["move"].values<-10.5)])[0] :
    ↪ data.index[(data["move"].values>-2) & (data["move"].values<-1.5)])[0].values)
108     xml=(data["move"][data.index[(data["move"].values>2) & (data["move"].values<2.5)])[0] :
    ↪ data.index[(data["move"].values>15) & (data["move"].values<15.5)])[0].values)
109     wml=(data["BL"][data.index[(data["move"].values>2) & (data["move"].values<2.5)])[0] :
    ↪ data.index[(data["move"].values>15) & (data["move"].values<15.5)])[0].values)
110     xhh=(data["move"][data.index[(data["move"].values>20) & (data["move"].values<20.5)])[0] :
    ↪ data.index[(data["move"].values>35) & (data["move"].values<35.5)])[0].values)
111     yhh=(data["BL"][data.index[(data["move"].values>20) & (data["move"].values<20.5)])[0] :
    ↪ data.index[(data["move"].values>35) & (data["move"].values<35.5)])[0].values)
112     xhl=(data["move"][data.index[(data["move"].values>33) & (data["move"].values<33.5)])[0] :
    ↪ data.index[(data["move"].values>44) & (data["move"].values<44.5)])[0].values)
113     yhl=(data["BL"][data.index[(data["move"].values>33) & (data["move"].values<33.5)])[0] :
    ↪ data.index[(data["move"].values>44) & (data["move"].values<44.5)])[0].values)
114     else:
115         xlh=(data["move"][data.index[(data["move"].values>-25) & (data["move"].values<-24.5)])[0] :
    ↪ data.index[(data["move"].values>-17) & (data["move"].values<-16.5)])[0].values)
116         ylh=(data["BL"][data.index[(data["move"].values>-25) & (data["move"].values<-24.5)])[0] :
    ↪ data.index[(data["move"].values>-17) & (data["move"].values<-16.5)])[0].values)
117         xll=(data["move"][data.index[(data["move"].values>-15) & (data["move"].values<-14.5)])[0] :
    ↪ data.index[(data["move"].values>-8) & (data["move"].values<-7.5)])[0].values)
118         yll=(data["BL"][data.index[(data["move"].values>-15) & (data["move"].values<-14.5)])[0] :
    ↪ data.index[(data["move"].values>-8) & (data["move"].values<-7.5)])[0].values)
119         xmh=(data["move"][data.index[(data["move"].values>-6) & (data["move"].values<-5.5)])[0] :
    ↪ data.index[(data["move"].values>0) & (data["move"].values<0.5)])[0].values)
120         ymh=(data["BL"][data.index[(data["move"].values>-6) & (data["move"].values<-5.5)])[0] :
    ↪ data.index[(data["move"].values>0) & (data["move"].values<0.5)])[0].values)
121         xml=(data["move"][data.index[(data["move"].values>0) & (data["move"].values<0.5)])[0] :
    ↪ data.index[(data["move"].values>5.5) & (data["move"].values<6)])[0].values)
122         yml=(data["BL"][data.index[(data["move"].values>0) & (data["move"].values<0.5)])[0] :
    ↪ data.index[(data["move"].values>5.5) & (data["move"].values<6)])[0].values)
123         xhh=(data["move"][data.index[(data["move"].values>6) & (data["move"].values<6.5)])[0] :
    ↪ data.index[(data["move"].values>14.5) & (data["move"].values<15)])[0].values)
124         yhh=(data["BL"][data.index[(data["move"].values>6) & (data["move"].values<6.5)])[0] :
    ↪ data.index[(data["move"].values>14.5) & (data["move"].values<15)])[0].values)
125         xhl=(data["move"][data.index[(data["move"].values>14.5) & (data["move"].values<15)])[0] :
    ↪ data.index[(data["move"].values>30) & (data["move"].values<30.5)])[0].values)
126         yhl=(data["BL"][data.index[(data["move"].values>14.5) & (data["move"].values<15)])[0] :
    ↪ data.index[(data["move"].values>30) & (data["move"].values<30.5)])[0].values)
127     #Finden Highs, lows, intersections
128     def _2Lorentzian(x, amp1, cen1, wid1, amp2,cen2,wid2):
129         return (amp1*wid1**2/((x-cen1)**2+wid1**2)) +\
130             (amp2*wid2**2/((x-cen2)**2+wid2**2))
131     def _1Lorentzian(x, amp1, cen1, wid1):
132         return (amp1*wid1**2/((x-cen1)**2+wid1**2))
133     done="R"
134     from lmfit import Model
135     while done=="R":
136         gmodel2 = Model(_2Lorentzian)
137         gmodel1 = Model(_1Lorentzian)
138         params2 = gmodel2.make_params(amp1=1, cen1=1, wid1=1,amp2=1,cen2=1,wid2=1)
139         params1 = gmodel1.make_params(amp1=1, cen1=1, wid1=1)
140         lh= gmodel2.fit(ylh, params2, x=xlh)

```

```

141     ll= gmodel2.fit(yll, params2, x=xll)
142     mh= gmodel2.fit(ymh, params2, x=xmh)
143     ml= gmodel2.fit(yml, params2, x=xml)
144     hh= gmodel2.fit(yhh, params2, x=xhh)
145     hl= gmodel2.fit(yhl, params2, x=xhl)

146     rrlh= 1 - lh.residual.var() / np.var(ylh)
147     rrll= 1 - ll.residual.var() / np.var(yll)
148     rrmh= 1 - mh.residual.var() / np.var(ymh)
149     rrml= 1 - ml.residual.var() / np.var(yml)
150     rrhh= 1 - hh.residual.var() / np.var(yhh)
151     rrhl= 1 - hl.residual.var() / np.var(yhl)

152     lhx=xlh[np.argmax(lh.best_fit)]
153     llx=xll[np.argmin(ll.best_fit)]
154     mxh=xmh[np.argmax(mh.best_fit)]
155     mlx=xml[np.argmin(ml.best_fit)]
156     hhx=xhh[np.argmax(hh.best_fit)]
157     hlx=xhl[np.argmin(hl.best_fit)]
158     lhy=lh.best_fit[np.argmax(lh.best_fit)]
159     lly=ll.best_fit[np.argmin(ll.best_fit)]
160     mhy=mh.best_fit[np.argmax(mh.best_fit)]
161     mly=ml.best_fit[np.argmin(ml.best_fit)]
162     hhy=hh.best_fit[np.argmax(hh.best_fit)]
163     hly=hl.best_fit[np.argmin(hl.best_fit)]

164     extremax=[lhx,llx,mhx,mlx,hlx]
165     extremay=[lhy,lly,mhy,mly,hly]

166     plt.plot(x[xx1], y[xx1], "go")
167     plt.plot(x[xx2], y[xx2], "go")

168     plt.show()
169     #plt.plot(xnew, f(x), '- ')

170     plt.axhline(y=0, color='black', linestyle='--')
171     plt.plot(extremax, extremay, 'go', label='best fit', zorder=10)
172     plt.plot(xlh, lh.best_fit, 'r-', label='best fit')
173     plt.plot(xll, ll.best_fit, 'r-', label='best fit')
174     plt.plot(xmh, mh.best_fit, 'r-', label='best fit')
175     plt.plot(xml, ml.best_fit, 'r-', label='best fit')
176     #plt.plot(xhh, hh.best_fit, 'r-', label='best fit')
177     plt.plot(xhl, hl.best_fit, 'r-', label='best fit')
178     plt.legend([filename], loc='best')
179     plt.plot(xnew,y, '- ')
180     plt.show()
181     done="yes"

182     noisetosignal= varybl/mhy*1000

183     #getting 2Azz
184     azz2=(hlx-lhx)
185     #getting dH (mobility) rt
186     dH=1/(mlx-mhx)
187     #getting proximity
188     proxy=(lhy-lly)/(0.5*(mhy-mly))
189     ↵ filename2=filename+"_NoisetoSignalRatio_"+str(noisetosignal.round(2))+".csv"
190     y=y/mhy*100+75*counter
191     df1=pd.DataFrame({"x":xnew,filename+" "+ str(noisetosignal.round(2)):y})
192     #df2=pd.DataFrame({"filename":filename2, "azz":azz2, "prox":proxy, "deltaH":dH, "
193     #rrlh":rrlh, "rrll":rrll, "rrmh":rrmh, "rrml":rrml, "rrhh":rrhh, "rrhl":rrhl})
194     df1.to_csv(filename2, index=False)

```

```
194     #df2.to_csv("output.csv", index=False, mode='a')
195     import csv
196     list=(filename2, azz2, proxy, dH, rrlh, rrl1,rrmh, rrml,rrhl)
197     with open('output.csv','a', newline='') as f:
198         writer = csv.writer(f)
199         writer.writerow(list)
```


10 List of Figures

1	BiP as sensor for unfolded proteins	11
2	Overview of the UPR signaling	12
3	A schematic illustration of hydrophobic mismatch.	14
4	IRE1 dimerizes to reduce the energetic cost of membrane compression.	15
5	Schematic illustration of the Zeeman effect.	17
6	Bioinformatical analysis of the human PERK-TMR.	42
7	The sequence of PERK-TMR is highly conserved in varying animals.	43
8	Purification of the PERK-TMR minimal sensor construct.	44
9	Isolation of single-cysteine variants of PERK-TMR.	45
10	EPR spectroscopy reveals free MTS labels in preparations of PERK-TMR.	46
11	Size-exclusion chromatography indicates a monodisperse preparation of MTS-labeled PERK-TMR constructs and removes free MTS labels.	47
12	Dimers of PERK-TMR protein remain in the final preparation after SEC.	48
13	Walkthrough of the calculation of the labeling efficiency.	49
14	MTS labeling efficiency of single-cysteine variants of PERK-TMR.	50
15	The cysteine-less PERK-TMR is prone for aggregation during reconstitution in liposomes.	51
16	Lipid environment and lipid package density have a big impact on the success of reconstitution of cysteine-less PERK-TMR.	54
17	Lowering the ratio of protein to lipid improves the reconstitution of PERK-TMR in liposomes.	55
18	The loss of protein during reconstitution is negligible.	56
19	Cysteineless PERK-TMR protein integrates successfully into a 100% POPC membrane.	57
20	Illustration of spectra analysis on representative cwEPR spectra recorded at different temperatures.	58
21	Establishing the pipeline for automatic processing of EPR-spectra.	60
22	Mobility data of the PERK-TMR helix through RT cwEPR spectra.	63
23	Proximity and micro-environmental polarity data of the PERK-TMR helix through low temperature cwEPR measurements.	65
24	Structural formula of lipids used to engineer different lipid environments.	66
25	Characterization of the lipid mixtures used to simulate "ON" and "OFF" conditions of the UPR.	67
26	The CHO2 lipid mixture leads to a pronounced broadening of the RT EPR spectrum of our native cysteine construct.	69
27	The CHO2 lipid mixture leads to a pronounced broadening of the LT EPR spectrum of our native cysteine construct.	70
28	Characterization of the lipid mixtures used to examine the effect of various PE:PC ratios on the PERK-TMR and its reconstitution success.	72
29	A increase of POPE in the lipid mixture has no effect on the RT EPR spectrum of our native cysteine construct.	73

30	A increase of POPE in the lipid mixture leads to a minuscule broadening of the LT EPR spectrum of our native cysteine construct.	74
31	Characterization of the lipid mixtures used to examine the effect of various lipid packaging densities on the PERK-TMR and its reconstitution success.	76
32	A increase of cholesterol in the lipid mixture has only a pronounced effect on the RT EPR spectrum of our native cysteine construct at high concentrations.	77
33	A increase of cholesterol in the lipid mixture has only a pronounced effect on the LT EPR spectrum of our native cysteine construct at high concentrations.	78
34	Characterization of the lipid mixtures used to examine the effect of various Soy PI contents on the PERK-TMR and its reconstitution success.	79
35	A increase of Soy PI in the lipid mixture has no effect on the RT EPR spectrum of our native cysteine construct.	80
36	A increase of Soy PI in the lipid mixture has no effect on the LT EPR spectrum of our native cysteine construct.	81

11 List of Tables

1	Equipment used in this study.	20
2	List of chemicals and their sources used in this study	21
3	Lipids used in this study. Stocks are stored in chloroform overlaid with nitrogen at -80°C.	21
4	Commercial kits/premade mixtures used in this study.	22
5	List of consumables and their sources used in this study	22
6	Enzymes used in this study, stored at -20 °C.	23
7	Probes and fluorescencet dyes used in this study.	23
8	Antibodies used in this study.	23
9	Table of forward (fwd) and reverse (rev) primers for Quikchange™ SDM of point mutations of PERK-TMR constructs used in this work.	24
10	Table of forward (fwd) and reverse (rev) primers for Q5™ SDM of point mutations of PERK-TMR constructs used in this work.	24
11	Table of forward (fwd) and reverse (rev) primers for In-Fusion™ SDM of point mutations of PERK-TMR constructs used in this work.	25
12	Table of forward (fwd) and reverse (rev) primers for sequencing PERK-TMR constructs used in this work.	25
13	Table of plasmids used and constructed in this study.	26
14	<i>E. coli</i> strains used in this study.	26
15	Media for cultivation of <i>E. coli</i>	27
16	Buffers used in this work.	28
17	Standard reaction mixture for Quikchange™ SDM.	31
18	Standard reaction conditions for Quikchange™ SDM.	31
19	Standard reaction mixture for In-Fusion™ SDM.	31
20	Standard reaction conditions for In-Fusion™ SDM.	32
21	Standard reaction mixture for Q5™ SDM.	32
22	Standard reaction conditions for Q5™ SDM.	32
23	Lipids mixtures for liposome preparation with a 10 mM lipid concentration.	36
24	Default recording options for EPR spectra.	38

12 Acronyms

β-OG	octyl-beta-glucosid	LBS	Lipid Bilayer Stress
AH	amphipathic helix	LPD	lipid packing density
amp	Ampicillin	LT	low temperature (-196 °C)
ATF4	Activating Transcription Factor 4	MBP	maltose-binding protein
ATF6	activating transcription factor 6	mRNA	messenger ribonucleic acid
BiP	binding immunoglobulin protein	MSB	Membrane Sample Buffer
bp	base pair	MTS	1-Oxyl-2,2,5,5-tetramethyl-3-pyrroline-3-methyl)methanethiosulfonate
cwEPR	continuous-wave electron paramagnetic resonance	OD	optical density
DMSO	dimethyl sulfoxide	P:L	protein-to-lipid ratios
DNA	deoxyribonucleic acid	PBS	phosphate-buffered saline
DOPC	1,2-dioleoyl- <i>sn</i> -glycero-3-phosphocholine	PC	phosphatidylcholine
DPPC	1,2-dipalmitoyl- <i>sn</i> -glycero-3-phosphocholine	PCR	polymerase chain reaction
DTT	Dithiothreitol	PE	phosphatidylethanolamine
eIF2α	α subunit of eukaryotic initiation factor 2	PERK	protein kinase R like endoplasmic reticulum kinase
EPR	electron paramagnetic resonance spectroscopy	POPC	1-palmitoyl-2-oleoyl- <i>sn</i> -glycero-3-phosphocholine
ER	endoplasmatic reticulum	POPE	1-palmitoyl-2-oleoyl- <i>sn</i> -glycero-3-phosphoethanolamine
ERAD	ER-associated degradation	rER	rough endoplasmatic reticulum
FRET	Förster resonance energy transfer	rpm	revolutions per minute
GP	generalized polarization	RT	room temperature (20-26 °C)
HEPES	4-(2-hydroxyethyl)-1-piperazine-ethanesulfonic acid	SDM	site-directed mutagenesis
IPTG	Isopropyl β -D-1-thiogalactopyranoside	SDS-PAGE	sodium dodecyl sulfate polyacrylamide gel electrophoresis
IRE1α	inositol-requiring enzyme type 1	sER	smooth endoplasmatic reticulum
KLD	kinase, ligase and <i>DpnI</i> ,	SOB	Super Optimal Broth
LB	lysogeny broth	Soy PI	L- α -phosphatidylinositol [from Soy plant]
		SRP	signal recognition particle
		TAE	TRIS-Acetate-EDTA

TB transformation buffer

TBS-T Tris-buffered saline with Tween20

TEV *Tobacco Etch Virus* (nuclear-inclusion-a
endopeptidase)

TMH transmembrane helix

TMR transmembrane region

UPR Unfolded Protein Response

UV/Vis ultraviolet/visible light

v/v volume per volume

w/v weight per volume

WT wild type

13 References

1. Ariyama, H., N. Kono, S. Matsuda, T. Inoue, H. Arai (2010). "Decrease in Membrane Phospholipid Unsaturation Induces Unfolded Protein Response". *The Journal of Biological Chemistry* 285, 22027–22035.
2. Ballweg, S., E. Sezgin, M. Doktorova, R. Covino, J. Reinhard, D. Wunnicke, I. Hänel, I. Levental, G. Hummer, R. Ernst (2020). "Regulation of Lipid Saturation without Sensing Membrane Fluidity". *Nature Communications* 11, 756.
3. Bernsel, A., H. Viklund, A. Hennerdal, A. Elofsson (2009). "TOPCONS: Consensus Prediction of Membrane Protein Topology". *Nucleic Acids Research* 37, W465–W468.
4. Bordignon, E., H.-J. Steinhoff (2007). "Membrane Protein Structure and Dynamics Studied by Site-Directed Spin-Labeling ESR". *ESR Spectroscopy in Membrane Biophysics*. Boston, MA: Springer US, 129–164.
5. Braakman, I., D. N. Hebert (2013). "Protein Folding in the Endoplasmic Reticulum". *Cold Spring Harbor Perspectives in Biology* 5, a013201.
6. Bruckert, J. (2016). *Reinigung Und Vergleichende Charakterisierung Des Transmembranhelices von IRE1 and PERK*. Bachelor Thesis. Frankfurt University, 1–65.
7. Clement, A. B., M. Gamberdinger, I. Y. Tamboli, D. Lütjohann, J. Walter, I. Greeve, G. Gimpl, C. Behl (2009). "Adaptation of Neuronal Cells to Chronic Oxidative Stress Is Associated with Altered Cholesterol and Sphingolipid Homeostasis and Lysosomal Function". *Journal of Neurochemistry* 111, 669–682.
8. Contreras, F.-X., A. M. Ernst, P. Haberkant, P. Björkholm, E. Lindahl, B. Gönen, C. Tischer, A. Elofsson, G. von Heijne, C. Thiele, R. Pepperkok, F. Wieland, B. Brügger (2012). "Molecular Recognition of a Single Sphingolipid Species by a Protein's Transmembrane Domain". *Nature* 481, 525–529.
9. Covino, R., S. Ballweg, C. Stordeur, J. B. Michaelis, K. Puth, F. Wernig, A. Bahrami, A. M. Ernst, G. Hummer, R. Ernst (2016). "A Eukaryotic Sensor for Membrane Lipid Saturation". *Molecular Cell* 63, 49–59.
10. Dupont, S., L. Beney, T. Ferreira, P. Gervais (2011). "Nature of Sterols Affects Plasma Membrane Behavior and Yeast Survival during Dehydration". *Biochimica et Biophysica Acta (BBA) - Biomembranes* 1808, 1520–1528.
11. Edwards, D. T., Z. Ma, T. J. Meade, D. Goldfarb, S. Han, M. S. Sherwin (2013). "Extending the Distance Range Accessed with Continuous Wave EPR with Gd³⁺ Spin Probes at High Magnetic Fields". *Physical chemistry chemical physics: PCCP* 15, 11313–11326.
12. Ellgaard, L., A. Helenius (2003). "Quality Control in the Endoplasmic Reticulum". *Nature Reviews Molecular Cell Biology* 4, 181–191.
13. Fattal, D., A. Ben-Shaul (1993). "A Molecular Model for Lipid-Protein Interaction in Membranes: The Role of Hydrophobic Mismatch". *Biophysical Journal* 65, 1795–1809.

14. Fu, S., L. Yang, P. Li, O. Hofmann, L. Dicker, W. Hide, X. Lin, S. M. Watkins, A. R. Ivanov, G. S. Hotamisligil (2011). "Aberrant Lipid Metabolism Disrupts Calcium Homeostasis Causing Liver Endoplasmic Reticulum Stress in Obesity". *Nature* 473, 528–531.
15. Gautier, R., D. Douguet, B. Antony, G. Drin (2008). "HELIQUEST: A Web Server to Screen Sequences with Specific α -Helical Properties". *Bioinformatics (Oxford, England)* 24, 2101–2102.
16. Halbleib, K., K. Pesek, R. Covino, H. F. Hofbauer, D. Wunnicke, I. Hänel, G. Hummer, R. Ernst (2017). "Activation of the Unfolded Protein Response by Lipid Bilayer Stress". *Molecular Cell* 67, 673–684.
17. Han, J., R. J. Kaufman (2016). "The Role of ER Stress in Lipid Metabolism and Lipotoxicity". *Journal of Lipid Research* 57, 1329–1338.
18. Hebert, D. N., M. Molinari (2007). "In and out of the ER: Protein Folding, Quality Control, Degradation, and Related Human Diseases". *Physiological Reviews* 87, 1377–1408.
19. Ho, N., W. S. Yap, J. Xu, H. Wu, J. H. Koh, W. W. B. Goh, B. George, S. C. Chong, S. Taubert, G. Thibault (2020). "Stress Sensor Ire1 Deploys a Divergent Transcriptional Program in Response to Lipid Bilayer Stress". *Journal of Cell Biology* 219, e201909165.
20. Hotamisligil, G. S. (2010). "Endoplasmic Reticulum Stress and the Inflammatory Basis of Metabolic Disease". *Cell* 140, 900–917.
21. Inoue, H., H. Nojima, H. Okayama (1990). "High Efficiency Transformation of Escherichia Coli with Plasmids". *Gene* 96, 23–28.
22. Janmey, P., P. Kinnunen (2006). "Biophysical Properties of Lipids and Dynamic Membranes". *Trends in cell biology* 16, 538–546.
23. Jeschke, G. (2012). "DEER Distance Measurements on Proteins". *Annual Review of Physical Chemistry* 63, 419–446.
24. Johnston, A. J., Y. (Zhang, S. Busch, L. C. Pardo, S. Imberti, S. E. McLain (2015). "Amphipathic Solvation of Indole: Implications for the Role of Tryptophan in Membrane Proteins". *The Journal of Physical Chemistry B* 119, 5979–5987.
25. Jumpertz, T., B. Tschapek, N. Infed, S. H. J. Smits, R. Ernst, L. Schmitt (2011). "High-Throughput Evaluation of the Critical Micelle Concentration of Detergents". *Analytical Biochemistry* 408, 64–70.
26. Juneja, A., A. Sultan, S. Bhatnagar (2012). "Wolcott-Rallison Syndrome". *Journal of the Indian Society of Pedodontics and Preventive Dentistry* 30, 250–253.
27. Kaiser, H.-J., D. Lingwood, I. Levental, J. L. Sampaio, L. Kalvodova, L. Rajendran, K. Simons (2009). "Order of Lipid Phases in Model and Plasma Membranes". *Proceedings of the National Academy of Sciences* 106, 16645–16650.

28. Kaiser, H.-J., A. Orłowski, T. Róg, T. K. M. Nyholm, W. Chai, T. Feizi, D. Lingwood, I. Vattulainen, K. Simons (2011). "Lateral Sorting in Model Membranes by Cholesterol-Mediated Hydrophobic Matching". *Proceedings of the National Academy of Sciences* 108, 16628–16633.
29. Kitai, Y., H. Ariyama, N. Kono, D. Oikawa, T. Iwawaki, H. Arai (2013). "Membrane Lipid Saturation Activates IRE1 α without Inducing Clustering". *Genes to Cells* 18, 798–809.
30. Koch, G. L. (1990). "The Endoplasmic Reticulum and Calcium Storage". *BioEssays: News and Reviews in Molecular, Cellular and Developmental Biology* 12, 527–531.
31. Kopp, M. C., N. Larburu, V. Durairaj, C. J. Adams, M. M. U. Ali (2019). "UPR Proteins IRE1 and PERK Switch BiP from Chaperone to ER Stress Sensor". *Nature Structural & Molecular Biology* 26, 1053–1062.
32. Korennykh, A., P. Walter (2012). "Structural Basis of the Unfolded Protein Response". *Annual Review of Cell and Developmental Biology* 28, 251–277.
33. Kozutsumi, Y., M. Segal, K. Normington, M.-J. Gething, J. Sambrook (1988). "The Presence of Malfolded Proteins in the Endoplasmic Reticulum Signals the Induction of Glucose-Regulated Proteins". *Nature* 332, 462–464.
34. Krogh, A., B. Larsson, G. von Heijne, E. L. Sonnhammer (2001). "Predicting Transmembrane Protein Topology with a Hidden Markov Model: Application to Complete Genomes". *Journal of Molecular Biology* 305, 567–580.
35. Maiuolo, J., S. Bulotta, C. Verderio, R. Benfante, N. Borgese (2011). "Selective Activation of the Transcription Factor ATF6 Mediates Endoplasmic Reticulum Proliferation Triggered by a Membrane Protein". *Proceedings of the National Academy of Sciences* 108, 7832–7837.
36. Malekar, V. C., J. D. Morton, R. N. Hider, R. H. Cruickshank, S. Hodge, V. J. Metcalf (2018). "Effect of Elevated Temperature on Membrane Lipid Saturation in Antarctic Notothenioid Fish". *PeerJ* 6, e4765.
37. Mandl, J., T. Mészáros, G. Bánhegyi, M. Csala (2013). "Minireview: Endoplasmic Reticulum Stress: Control in Protein, Lipid, and Signal Homeostasis". *Molecular Endocrinology* 27, 384–393.
38. Merrick, W. C. (1992). "Mechanism and Regulation of Eukaryotic Protein Synthesis". *Microbiological Reviews* 56, 291–315.
39. Molin, N., K. M. Salikhov, K. I. Zamaraev (1980). *Spin Exchange: Principles and Applications in Chemistry and Biology*. Tech. rep. Springer-Verlag, 242.
40. Mouritsen, O., M. Bloom (1984). "Mattress Model of Lipid-Protein Interactions in Membranes". *Biophysical Journal* 46, 141–153.
41. NCBI Resource Coordinators (2018). "Database Resources of the National Center for Biotechnology Information". *Nucleic Acids Research* 46, D8–D13.

42. Ozbek, M. N., V. Senée, S. Aydemir, L. D. Kotan, N. O. Mungan, B. Yuksel, C. Julier, A. K. Topaloglu (2010). "Wolcott-Rallison Syndrome Due to the Same Mutation (W522X) in EIF2AK3 in Two Unrelated Families and Review of the Literature". *Pediatric Diabetes* 11, 279–285.
43. Pineau, L., J. Colas, S. Dupont, L. Beney, P. Fleurat-Lessard, J.-M. Berjeaud, T. Bergès, T. Ferreira (2009). "Lipid-Induced ER Stress: Synergistic Effects of Sterols and Saturated Fatty Acids". *Traffic* 10, 673–690.
44. Pool, M. R. (2022). "Targeting of Proteins for Translocation at the Endoplasmic Reticulum". *International Journal of Molecular Sciences* 23, 3773.
45. Prasad, R., A. Sliwa-Gonzalez, Y. Barral (2020). "Mapping Bilayer Thickness in the ER Membrane". *Science Advances* 6, eaba5130.
46. Preissler, S., C. Rato, Y. Yan, L. A. Perera, A. Czako, D. Ron (2020). "Calcium Depletion Challenges Endoplasmic Reticulum Proteostasis by Destabilising BiP-substrate Complexes". *eLife* 9, e62601.
47. Radanović, T., R. Ernst (2021). "The Unfolded Protein Response as a Guardian of the Secretory Pathway". *Cells* 10, 2965.
48. Radanović, T., J. Reinhard, S. Ballweg, K. Pesek, R. Ernst (2018). "An Emerging Group of Membrane Property Sensors Controls the Physical State of Organellar Membranes to Maintain Their Identity". *BioEssays* 40, 1700250.
49. Reinhard, J., L. Starke, C. Klose, P. Haberkant, H. Hammarén, F. Stein, O. Klein, C. Berhorst, H. Stumpf, J. P. Sáenz, J. Hub, M. Schuldiner, R. Ernst (2024). "MemPrep, a New Technology for Isolating Organellar Membranes Provides Fingerprints of Lipid Bilayer Stress". *The EMBO Journal* 43, 1653–1685.
50. Renne, M. F., R. Ernst (2023). "Membrane Homeostasis beyond Fluidity: Control of Membrane Compressibility". *Trends in Biochemical Sciences* 48, 963–977.
51. Robertson, J. L. (2018). "The Lipid Bilayer Membrane and Its Protein Constituents". *Journal of General Physiology* 150, 1472–1483.
52. Salikhov, K. M. (2021). "New Information About Manifestations of Spin Exchange in the EPR Spectra of Solutions of Paramagnetic Particles Under Saturation Conditions". *Applied Magnetic Resonance* 52, 1063–1091.
53. Schosseler, P. M. (1998). *Electron Paramagnetic Resonance Study of the Copper(II) Complexation with Carbonate Ligands in Aqueous Solution and at Calcium Carbonate Surfaces*. Doctoral Thesis. ETH Zurich, 5–27.
54. Senée, V. et al. (2004). "Wolcott-Rallison Syndrome: Clinical, Genetic, and Functional Study of EIF2AK3 Mutations and Suggestion of Genetic Heterogeneity". *Diabetes* 53, 1876–1883.
55. Sharpe, H. J., T. J. Stevens, S. Munro (2010). "A Comprehensive Comparison of Transmembrane Domains Reveals Organelle-Specific Properties". *Cell* 142, 158–169.

56. Sievers, F., A. Wilm, D. Dineen, T. J. Gibson, K. Karplus, W. Li, R. Lopez, H. McWilliam, M. Remmert, J. Söding, J. D. Thompson, D. G. Higgins (2011). "Fast, Scalable Generation of High-Quality Protein Multiple Sequence Alignments Using Clustal Omega". *Molecular Systems Biology* 7, 539.
57. Singer, S. J., G. L. Nicolson (1972). "The Fluid Mosaic Model of the Structure of Cell Membranes". *Science (New York, N.Y.)* 175, 720–731.
58. Situ, A. J., S.-M. Kang, B. B. Frey, W. An, C. Kim, T. S. Ulmer (2018). "Membrane Anchoring of α -Helical Proteins: Role of Tryptophan". *The Journal of Physical Chemistry B* 122, 1185–1194.
59. Sonnhammer, E. L., G. von Heijne, A. Krogh (1998). "A Hidden Markov Model for Predicting Transmembrane Helices in Protein Sequences". *Proceedings. International Conference on Intelligent Systems for Molecular Biology* 6, 175–182.
60. Spicher, L., G. Glauser, F. Kessler (2016). "Lipid Antioxidant and Galactolipid Remodeling under Temperature Stress in Tomato Plants". *Frontiers in Plant Science* 7, 1–12.
61. Sun, Z., J. L. Brodsky (2019). "Protein Quality Control in the Secretory Pathway". *Journal of Cell Biology* 218, 3171–3187.
62. Taira, H., I. Akimoto, T. Miyahara (1986). "Effects of Seeding Time on Lipid Content and Fatty Acid Composition of Buckwheat Grains". *Journal of Agricultural and Food Chemistry* 34, 14–17.
63. Tam, A. B., L. S. Roberts, V. Chandra, I. G. Rivera, D. K. Nomura, D. J. Forbes, M. Niwa (2018). "The UPR Activator ATF6 Responds to Proteotoxic and Lipotoxic Stress by Distinct Mechanisms". *Developmental Cell* 46, 327–343.
64. Thibault, G., G. Shui, W. Kim, G. C. McAlister, N. Ismail, S. P. Gygi, M. R. Wenk, D. T. W. Ng (2012). "The Membrane Stress Response Buffers Lethal Effects of Lipid Disequilibrium by Reprogramming the Protein Homeostasis Network". *Molecular Cell* 48, 16–27.
65. Tran, D. M., H. Takagi, Y. Kimata (2019). "Categorization of Endoplasmic Reticulum Stress as Accumulation of Unfolded Proteins or Membrane Lipid Aberrancy Using Yeast Ire1 Mutants". *Bioscience, Biotechnology, and Biochemistry* 83, 326–329.
66. van Meer, G., D. R. Voelker, G. W. Feigenson (2008). "Membrane Lipids: Where They Are and How They Behave". *Nature reviews. Molecular cell biology* 9, 112–124.
67. Vähä, K., C. Mattes, J. Reinhard, R. Covino, H. Stumpf, G. Hummer, R. Ernst (2021). "Cysteine Cross-Linking in Native Membranes Establishes the Transmembrane Architecture of Ire1". *Journal of Cell Biology* 220, e202011078.
68. Voeltz, G. K., M. M. Rolls, T. A. Rapoport (2002). "Structural Organization of the Endoplasmic Reticulum". *EMBO reports* 3, 944–950.

69. Volmer, R., K. van der Ploeg, D. Ron (2013). “Membrane Lipid Saturation Activates Endoplasmic Reticulum Unfolded Protein Response Transducers through Their Transmembrane Domains”. *Proceedings of the National Academy of Sciences* 110, 4628–4633.
70. Walter, P., D. Ron (2011). “The Unfolded Protein Response: From Stress Pathway to Homeostatic Regulation”. *Science* 334, 1081–1086.
71. Wang, P., J. Li, J. Tao, B. Sha (2018). “The Luminal Domain of the ER Stress Sensor Protein PERK Binds Misfolded Proteins and Thereby Triggers PERK Oligomerization”. *Journal of Biological Chemistry* 293, 4110–4121.
72. Westrate, L., J. Lee, W. Prinz, G. Voeltz (2015). “Form Follows Function: The Importance of Endoplasmic Reticulum Shape”. *Annual Review of Biochemistry* 84, 791–811.
73. Wu, H., P. Carvalho, G. K. Voeltz (2018). “Here, There, and Everywhere: The Importance of ER Membrane Contact Sites”. *Science* 361, eaan5835.
74. Wu, X., T. A. Rapoport (2021). “Translocation of Proteins through a Distorted Lipid Bilayer”. *Trends in Cell Biology* 31, 473–484.
75. Zámbo, V., L. Simon-Szabó, P. Szelényi, É. Kereszturi, G. Bánhegyi, M. Csala (2013). “Lipotoxicity in the Liver”. *World Journal of Hepatology* 5, 550–557.
76. Zhu, G., N. Yin, Q. Luo, J. Liu, X. Chen, L. Liu, J. Wu (2020). “Enhancement of Sphingolipid Synthesis Improves Osmotic Tolerance of *Saccharomyces Cerevisiae*”. *Applied and Environmental Microbiology* 86, e02911.

14 Danksagung

In dieser Arbeit gibt es vielen Leuten Dank auszusprechen. Zu aller erst meinem Betreuer und Doktorvater Prof. Robert Ernst, der diese Arbeit erst möglich gemacht hat und organisatorisch sowie persönlich immer unterstützend zur Seite stand. Du hast so viel möglich gemacht, für das ich unglaublich dankbar bin. Danke für deine humorvolle Art und deine auch manchmal frustrierende, aber immer positiv ausgerichteten Spontanität mit der neue Wege -argumentativ wie experimentell- eröffnet werden. Danke für die vielen Freiräume und Freiheiten und das große Vertrauen in einen, die zum Ausprobieren einladen und einem schnell Selbstverantwortung lehren.

Und danke für deinen persönlichen Einsatz. Man merkt, dass dein Herz an der Forschung und am Labor hängt -und nun auch an der Familie!-. Für mich war es irgendwann überraschender, dass du erst am nächsten Morgen auf eine E-mail geantwortet hast und nicht direkt schon um 3 Uhr nachts - 5 Minuten nach dem Absenden.

Ich danke dir für die Zeit, die mit einem Kaffee nach einem Vorklinik-Seminar begann und nach nun fast 5~ Jahren am Beginn der Facharztweiterbildung ihr Ende findet. Und ich erinnere mich noch an einen Satz, der damals auf dem Weg vom alten Biochemie-Gebäude zum Laborgebäude fiel: "Es ist doch egal wie lange etwas dauert, so lange man Spaß hat!". Und ich stimme dem voll zu: Ich habe viel gelernt, mein Weltbild einige Male umgestoßen und hatte Spaß!

Danke an meinen Zweitbetreuer Dr. Reinhard Kappl, der mir freundlicherweise Zugang zu seinem EPR-Equipment, seiner Werkstatt, seiner Erfahrung und seiner Zeit geschenkt hatte. Danke für die Vielzahl an Erklärungen, die Du auch oft genug wiederholt hast, weil ich sie meist nicht direkt verstanden habe. Für die einfache und schnelle Kommunikation beim Termine ausmachen und die vielen kleinen Handgriffe und Tricks, die in keiner Anleitung stehen. Und Danke für deine ruhige, entspannte und humorvolle Art!

Vielen Dank an Dr. Roberto Covino mit dessen MD Simulationen die Fantasie angeregt wurde und man eine bessere Vorstellung davon gewinnen konnte, wie Proteinhelix und Bilayer miteinander interagieren.

Einen ganz besonderen Dank möchte ich geschlossen an das ganze AG-Ernst Team schicken. Ohne diese großartige Atmosphäre und das Miteinander, den vielen geselligen Abenden und vielen tollen Persönlichkeiten hätte ich wahrscheinlich irgendwo auf dem Weg doch etwas Statistisches gemacht oder die Frustration siegen lassen. Danke für die offenen Ohren und die vielen Meinungen, danke für die viele geteilte Freude und den manchmal geteilten Ärger! Und danke, dass Ihr einen auf Abwegen geratenen Mediziner in eure naturwissenschaftlichen Hallen aufgenommen habt -ohne ihn fertig zu machen.

Danke an Dr. Stephanie Ballweg, die mich bei meinen ersten Schritten im Labor begleitet, mir Protokolle überlassen hatte und mir einige Shortcuts und Tipps und Tricks gezeigt hat. "Bereite alles so vor, dass du so wenig wie möglich denken musst - dann verwirrst du dich nicht selbst!"

Danke an Toni Radanovic, der später zu meinem Hauptansprechpartner wurde und mir -als Vorbild- gezeigt hat, was es heißt strukturiert vorzugehen, klar zu planen und zu dokumentieren, Variables zu vermeiden und Proben so zu verstauen, dass man auch noch nach Monaten weiß, woher sie kommen (wenn man damit nicht immer alle Racks besetzen würde). Würde ich noch einmal anfangen, würde ich vieles anders machen und das Laborbuch ganz anders beginnen. Danke für diese kreativen Ideen und persönliche Bastelprojekte, die immer beeindruckend waren und einen sprachlos zurücklassen!

Danke an Julia Hach, die mir vor allem beim Schließen der letzten Datenlücken praktisch geholfen hat, als das Studium einen wieder eingeholt hatte. Danke für deine offenen Ohren. Danke, dass du einen Teil des Büros zu einem bunten und herzlichen Ort gemacht hast und dass du das Labor immer auf den neusten Stand der Gesellschaftsspiele bringst! Danke, dass du das Labor mit vorausschauenden Bestellungen am Laufen -, und mit viel Freude zusammenhältst. Und Danke, dass ich Mitglied des Team Unicorn sein durfte.

Danke an Carsten Mattes für die unvergleichliche Selbstironie! Es war immer eine große Freude dir beim Anlegen des Hefegartens zuzusehen. Danke, dass du mir bei der Suche nach Ivat Ilf geholfen hattest. Und danke, dass ich bei deiner kulinarischen Reise und Entwicklung dabei sein durfte: Angefangen hat es mit den edelsten Sorten Sauce hollandaise, die durch Tetrapak-Technologie von der Außenwelt geschützt waren, über die besten Naschereien der Kindheit und irgendwann ist es dann in selbstgemachte Pralinen, Parfaits und Weine umgeschlagen! Danke für diese spannende Reise und einen weiteren Grund, einfach mal so in's Labor zu kommen.

Danke an John Reinhard, der eine Art Ruhepol im Labor und gefühlt mit jedem Gerät vertraut ist. Vielen Dank für's Troubleshooten, wenn mal wieder etwas nicht gelaufen ist und danke für die analytisch-hinterfragende Art bei den Journal-Clubs. Dadurch konnte man eine ganz andere Denkweise kennenlernen, die im Studium eher zu kurz kommt.

Danke Daniel Granz für die vielen Gespräche und das Durchführen von vielen kleinen Laborwettbewerben. Und vielleicht ein noch viel größeres Meta-Danke für deinen Lebensweg, du zeigst das vieles noch möglich ist, auch wenn man schon einen Weg eingeschlagen hatte und man sich immer ändern kann.

Danke Martina Zäch, für einerseits die viele organisatorische Arbeit. Aber auch für die gute Ortskenntnis im Saarland; die vielen vorgeschlagenen Wanderrouten, die man erst am Ende der Saarland-Zeit kennengelernt hat und die Stadt- und Waldführungen.

Danke auch an all die anderen, die das Labor und die Laborerfahrung mit Leben gefüllt hatten: Heike Stumpf, Charlotte Berhorst, Jona Causemann, Amnaa Jain, das ganze AG-Schul-Team. Und Danke an alle, die nur kurz da waren oder ich vergessen habe, oder die, die seit des praktischen Teils der Arbeit erst dazugekommen sind und ich gar nicht lange erleben durfte.

Und Danke an alle Leute, auf deren Vorarbeit ich mich stützen durfte - ob das nun Wissen, Plasmide, Programme, Libraries oder etwas anderes war-.

Die Arbeit hat mich die ganze Saarland-Zeit über begleitet, also will ich auch ein Danke an alle geben, die während dieser Zeit zu einer Art Familie für mich wurden: Olga -die inzwischen auch praktisch Teil der Familie wurde-, die Max-Kade Gruppe, die Homburger und Saarbrücker mit denen man den Großteil dieser Zeit verbringen durfte.

Einen extra Dank geht auch an meine neuen Kollegen, welche mich im Weg der klinischen Medizin begleiten, hierunter besonders Nele, die -durch Ihren Umweg in die englische Linguistik- noch einmal Schliff in den Ausdruck brachte! Und -natürlich- auch ein Danke nach Hause, zur Familie die mir auch 350 km entfernt immer halt gegeben hat; die man immer viel zu selten sieht.

Aus datenschutzrechtlichen Gründen wird der Lebenslauf in der elektronischen Fassung der Dissertation nicht veröffentlicht

